



**Modelling and development of a fault tolerant
permanent magnet machine for helicopter tail
rotor applications**

Qing Li

B.Sc., M.Sc.

A thesis submitted for the degree

of Doctor of Philosophy

October 2022

School of Engineering

Newcastle University

United Kingdom

Abstract

With environmental and energy issues becoming increasingly prominent, environmentally friendly transport is receiving progressively more attention and research. This thesis concentrates on a study of the motor used in the electric tail rotor of helicopters.

The concept of ‘More Electric Aircraft’ (MEA) has gained attention because of the many advantages it brings, such as enhanced aircraft performance, increased reliability, decreased operating and maintenance costs and reduced greenhouse gas emissions. All these advantages it brings have attracted a lot of attention to it. Helicopter technology has also been influenced by this conceptual approach.

This study proposes a Permanent Magnet (PM) motor design for a helicopter electric tail rotor with fault-tolerant performance. The performance of this type of motor was analysed using Finite Element (FE) simulation, paying particular attention to rotor losses and their mitigation, along with topologies which offer fault tolerance.

Due to the harsh working environment of motors, it is essential to prevent damage caused by high temperatures, such as insulation failure, demagnetisation of PMs. Losses were minimised and the heat dissipation performance of the motor was obtained by Computational Fluid Dynamics (CFD) simulation based on the finite element simulation results. A new hybrid cooling design was proposed that showed excellent cooling results in simulations.

Finally, considering the complexity of the model, part of the stator winding was manufactured with the hybrid cooling design and tested in a wind tunnel. The experimental and simulation results were compared, and the design was validated. The predicted and measured results showed some consistency in the cooling performance.

Acknowledgement

This project received help from many individuals. My first and foremost thanks goes to my supervisor, Prof. Barrie Mecrow, who has patiently reviewed, commented on, supported and encouraged my research work over the past four years. Under his guidance, I have not only improved my technical problem-solving skills, but also learned to think in a logical way. I would also like to express my deep gratitude to Dr Xu Deng for her advice and assistance both inside and outside the work environment. Last but not least, I would also express my deep gratitude to Dr Xiang Shen for his help and guidance on my project. The times I spent with him form happy memories.

I would also like to express my gratitude to the technicians and support staff who assisted me in building, assembling and testing the prototypes. Special thanks to Chris Annan, Chris Manning and John Smith at Newcastle University's Mechanical Workshop, and the UG lab's Gordon Marshall, as well as Martin Purvis from Northumbria University's Mechanical Workshop.

My heartfelt appreciation goes towards my parents, Xin Li and Ling Wang, who respect every decision I make and always support and encourage me during my study. Many thanks to my wonderful friends in Newcastle University, Ruosen Qi, Bowen Gu, Xiang Wang, Handong Li, Igao and Ramin. Their help and friendship will always be in my heart.

List of Figures

Figure 2-1: The trend toward the MEA [15].....	6
Figure 2-2: Power sources on a conventional civilian aircraft [21].....	7
Figure 2-3: Concept for the power sources on an MEA [21]	8
Figure 2-4: A380 electrical power system components [21]	10
Figure 2-5: Boeing 787 electrical power distribution system (physical locations) [31].	11
Figure 2-6: UH-60A single main rotor and tail rotor helicopter.....	12
Figure 2-7: A tandem main rotor helicopter – Boeing CH-47 Chinook.....	13
Figure 2-8: Torque effect on the helicopter	14
Figure 2-9: Fenestron tail rotor – EC120B	14
Figure 2-10: NOTAR – MD Explorer air ambulance [114]	15
Figure 2-11: Tail rotor configurations [43].....	16
Figure 2-12: Variants of electrification of the helicopter propulsion system [9]	18
Figure 2-13: Propulsion system topologies of the hybrid electric helicopter [79]	19
Figure 2-14: Proposed machine with slotless single-stator double-rotor [78].....	20
Figure 2-15: Combined propulsion system topologies of the hybrid electric helicopter [79]	21
Figure 2-16: Three-phase voltage source rectifier-inverter topology diagram.....	23
Figure 2-17: Single-phase H-bridge inverter diagram	23
Figure 2-18: Ventilation structure: (a) An EFC motor; (b) An OFC motor [72].....	26
Figure 2-19: Configuration of fin channels [94].....	27
Figure 3-1: Hysteresis loop for a ferromagnet or ferrimagnet [107]	33
Figure 3-2: Development of coercivity in the 20th century, showing the upper and lower extremes [106]	34
Figure 3-3: Magnetic energy product of PM materials [105].....	35
Figure 3-4: B–H curve of Vacoflux 48.....	36

Figure 3-5: Cross-section of the PM motor	38
Figure 3-6: Magnetisation curve for ferromagnets and corresponding permeability	39
Figure 3-7: Optimisation of the ratio of rotor yoke thickness to PM pitch	40
Figure 3-8: Optimisation of the ratio of stator yoke thickness to PM pitch	41
Figure 3-9: Tooth pitch to permanent magnet pitch ratio	41
Figure 3-10: Motor performance trends.....	44
Figure 3-11: Percentages of the different types of losses	45
Figure 4-1: The CAD model of the motor with 20 conductors	48
Figure 4-2: The CAD model of the motor with 80 conductors	49
Figure 4-3: AC loss from 1Hz to 1000Hz (20 conductors per slot)	50
Figure 4-4: AC loss from 1Hz to 1000Hz (80 conductors per slot)	50
Figure 4-5: The trend of AC loss/DC loss from 1 Hz to 1000Hz.....	50
Figure 4-6: (a) Surface-mounted PM motor (b) Interior PM motor	52
Figure 4-7: Segmentation per PM.....	53
Figure 4-8: The trend of PM losses by circumferential segmentation.....	54
Figure 4-9: Segmentation in the axial direction.....	54
Figure 4-10: The trend of PM losses by axial segmentation	55
Figure 4-11: Three different types of input current	56
Figure 4-12: The trend of PM losses with three type current sources and circumferential segmentation	57
Figure 4-14: 1/8 th model of the motor with rotor sleeve and copper shield	58
Figure 4-15: PM loss density distribution for the motor with 0.1mm copper shield.....	59
Figure 4-16: Rotor loss with current with additional 40kHz PWM harmonics.....	59
Figure 4-17: Structure of model with rotor cage on the q-axis.....	60
Figure 4-18: The connection of the rotor cage	61

Figure 4-19: (a) The structure of the PM with rotor cage on q-axis (b) PM losses distribution with ideal current input (c) PM losses distribution with current with a 40kHz switch frequency	61
Figure 4-20: The connection of the rotor cage	62
Figure 4-21: (a) PM losses distribution with ideal current input (b) PM losses distribution with current with a 40kHz switching frequency	62
Figure 4-22: Structure of model with rotor cage in d axis and q axis.....	64
Figure 4-23: (a) The structure of the PM with rotor cage on both d-axis and q-axis (b) PM losses distribution with idea current input (c) PM losses distribution with current with a 40kHz switch frequency	64
Figure 4-24: (a) The structure of the PM with a small rotor cage on both d-axis and q-axis (b) PM losses distribution with current with a 40kHz switch frequency	66
Figure 4-25: (a) The structure of the small rotor cage above PM (b) PM losses distribution with idea current input (c) PM losses distribution with current with a 40kHz switch frequency	67
Figure 4-26: (a) PM with circumferential segmentation and small rotor cage (b) PM losses distribution with idea current input (c) PM losses distribution with current with a 40kHz switch frequency	68
Figure 4-27: The structure of the interior PM model.....	69
Figure 4-28: The interior PM model with circumferential segmentation.....	70
Figure 4-29: The PM loss of interior PM model with circumferential segmentation.....	71
Figure 4-30: The PM loss of interior PM model with axial segmentation	72
Figure 4-31: The interior PM model with circumferential segmentation and rotor cage	72
Figure 4-32: The Rotor loss of interior PM model with circumferential segmentation and rotor cage	73
Figure 5-1: One-eighth of the motor.....	77
Figure 5-2: Field extractor in Simcenter MAGNET.....	77

Figure 5-3: Air gap magnetisation field of the motor with 48 slots and 56 poles	78
Figure 5-4: Air-gap harmonic spectrum of the motor with 48 slots and 56 poles	78
Figure 5-5: 1/16 th of the motor with 48 slots and 32 poles	79
Figure 5-6: Air gap magnetisation field of the motor with 48 slots and 32 poles	80
Figure 5-7: Air-gap harmonic spectrum of the motor with 48 slots and 32 poles	80
Figure 5-8: Fault-tolerant design with alternative segmented winding	82
Figure 5-9: Fault-tolerant design with interspersed winding	82
Figure 5-10: The back-EMF of the model (48Slots, 32Poles)	83
Figure 5-11: The updated back-EMF of the model (48Slots, 32Poles)	84
Figure 5-12: The updated back-EMF of the fault-tolerant model (48Slots, 32Poles)	85
Figure 5-13: Fault current while shorted at the terminals	87
Figure 5-14: The model with 5mm height slot tip	87
Figure 6-1: A 2D cross-section of the machine	91
Figure 6-2: The segment used for CFD thermal simulation	92
Figure 6-3: The computational domain in upstream view	95
Figure 6-4: Mesh details in upstream view	95
Figure 6-5: Input air flow temperature	96
Figure 6-6: (a) Temperature distribution in the 3D stator at an air speed of 10 m/s. (b) Temperature distribution in a 2D cross-section through the winding at an air speed of 10 m/s. The flow direction is left to right.	96
Figure 6-7: The velocity vector of the air flow in the 3D stator with an input airspeed of 10 m/s	97
Figure 6-8: The CAD model with a 0.5 mm air channel between windings.	98
Figure 6-9: Temperature distribution in a 2D cross-section of the winding at an input airspeed of 10 m/s. The flow direction is left to right	99

Figure 6-10: Temperature distribution in a 2D cross-section through the winding at an airspeed of (a) 10 m/s, (b) 20 m/s, (c) 30 m/s, and (d) 40 m/s. The flow direction is left to right.....	100
Figure 6-11: Maximum temperature rise when the input airspeed increases from 10 to 100 m/s.....	101
Figure 6-12: Definition of the width of the air channel, d , between windings.	102
Figure 6-13: Maximum temperature rise variation as the width of the air channel increases from 0.5 to 3 mm with different input airspeeds.	102
Figure 6-14: (a) The rectangular channel. (b) The tapered air channel.	103
Figure 6-15: (a) Temperature distribution of the model with a rectangular air channel in a 2D cross-section contour at an air speed of 10 m/s (b) Temperature distribution of the model with a triangular air channel in a 2D cross-section contour at an air speed of 10 m/s.....	104
Figure 6-16: Maximum temperature rise for different shaped air channels as a function of air flow rate.....	104
Figure 6-17: The maximum temperature rise variation as air turbulence intensity increase from 0.5% to 40% with different air flow velocity.....	105
Figure 6-18: The percentage reduction in temperature rise when the air turbulence intensity is increased from 0.5% to 40%	106
Figure 6-19: (a) The CAD model of the hybrid cooling design in (a) upstream view (b) downstream view	107
Figure 6-20: The mesh details of the hybrid cooling design in downstream view	108
Figure 6-21: The influence of water flow speed upon hotspot temperature rise	109
Figure 6-22: The cross-section of the model with a 3mm OD pipe at a water speed of 0.1m/s.....	109
Figure 6-23: The temperature of the liquid inside the pipe of the model with a 3 mm OD pipe at a water speed of 0.1 m/s.....	110
Figure 7-1: Test stator tooth units and winding blocks	112
Figure 7-2: Winding machine	112

Figure 7-3: 3D printed cover	112
Figure 7-4: Assembled base and pillars	113
Figure 7-5: 3D printed tooth units and winding blocks	113
Figure 7-6: Type K plug-in thermocouple	114
Figure 7-7: Test model with pipe of diameter: (a) 2 mm and (b) 3 mm.....	114
Figure 7-8: Assembled model for wind tunnel testing	115
Figure 7-9: Redesigned CAD model	116
Figure 7-10: Test rig for pressure test.....	117
Figure 7-11: Model placed inside the wind tunnel: (a) front view and (b) side view ..	118
Figure 7-12: Test rig setup and configuration for the wind tunnel experiments: (a) right side and (b) left side of wind tunnel	119
Figure 7-13: Comparison of experimental and numerical results at two measuring points for Model 1 at an airspeed of 10 m/s	120
Figure 7-14: Experimental results for Model 1 at an airspeed of 15 m/s	121
Figure 7-15: Comparison of experimental and numerical results at two measuring points for Model 2 at an airspeed of 10 m/s	122
Figure 7-16: Comparison of hot spot temperature rise in Models 3 and 4 at an airspeed of 10 m/s.....	122

List of Tables

Table 2-1: Rules of thumb for cooling type and heat transfer coefficients [92], [94]	25
Table 3-2: Performance comparison of different electrical machine topologies	32
Table 3-3: Motor Requirements.....	37
Table 3-4: Preliminary motor parameters	38
Table 3-5: Performance of the preliminary design	38
Table 3-6: Optimal motor parameters.....	42
Table 3-7: Optimised motor performance	42
Table 3-8: Motor dimensions as functions of the amplification coefficient.....	43
Table 4-1: Winding loss (20 conductors per slot).....	48
Table 4-2: Winding loss (80 conductors per slot).....	49
Table 4-3: The results of PM losses by FEA simulation	53
Table 4-4: PM length and loss by axial segmentation	54
Table 4-5: Simulation result of the model without segmentation.....	56
Table 4-6: Simulation result of the model with circumferential segmentation (4 segments)	56
Table 4-7: PM and cage loss with different input current	62
Table 4-8: PM and cage loss with different input current	63
Table 4-9: PM and cage loss with different input currents for different models.....	65
Table 4-10: PM and cage loss of motor with a small rotor cage with different input currents.....	66
Table 4-11: Ideal input current	66
Table 4-12: Current with 40kHz time-harmonic	67
Table 4-13: The rotor loss of the interior PM model.....	69
Table 4-14: The PM loss of interior PM model with ideal current.....	70
Table 4-15: The PM loss of interior PM model with 40kHz time-harmonic	70

Table 4-16: The rotor loss of interior PM model with ideal current.....	71
Table 4-17: The rotor loss of interior PM model with 40kHz time-harmonic	71
Table 4-18: The rotor loss of interior PM model with rotor cage and sinewave current	73
Table 4-19: The rotor loss of interior PM model with rotor cage and time-harmonic ...	73
Table 4-20: The rotor loss of interior PM model with rotor cage, time-harmonic and axial segmentation	73
Table 5-1: Slot angle distribution for a 12 slot and 14 poles unit motor	76
Table 5-2: Slot angle distribution for 12 slots and 8 poles unit motor	79
Table 5-3: Key parameters and performance comparison	81
Table 5-4: A comparison of the torque and PM loss	83
Table 5-5: Voltages needed to give the required back-EMF	84
Table 5-6: Updated key parameters for original model.....	84
Table 5-7: Updated key parameters for fault-tolerant model	85
Table 5-8: Back-EMF of two FT design model.....	86
Table 5-9: Output torque and torque ripple of the model	86
Table 5-10: Output torque of the model	86
Table 5-11: Short current with different height of slot tip.....	88
Table 6-1: Key parameters of the proposed motor	92
Table 6-2: Properties of materials.....	93
Table 6-3: Equivalent thermal conductivity of winding	94
Table 6-4: Comparison of model parameters with and without air channels	98
Table 6-5: The change of key winding parameters while increasing the width of the air channel.....	101
Table 6-6: Comparison of model parameters with different size pipe	107
Table 6-7: Temperature rises in hot spot for the two models	108
Table 7-1: Relationship between water-flow velocity and flow rate.....	115

Table 7-2: Key parameters of different models	116
Table 7-3: Experimental results of hot spot temperature rise	123
Table 7-4: Experimental results of hot spot temperature rise after sealing the windings with varnish.....	123

List of abbreviations

APU	Auxiliary Power Unit
B	Battery
BCRUs	Battery Charge Regulator Units
BLAC	Brushless AC
C	Converter
CFD	Computational Fluid Dynamics
CFF	Coil Fill Factor
CU	Control Unit
EFC	Enclosed Fan-Cooled
EM	Electric Motor
ETR	Electric Tail Rotor
FC	Fuel Cell
FE	Finite Element
FEA	Finite Element Analysis
G	Generator
GB	Gearbox
GTE	Gas Turbine Engine
ID	Inner Diameter
IM	Induction Machine
IPM	Interior Permanent Magnet
LPTN	Lumped Parameter Thermal Networks
MEA	More Electric Aircraft
MMF	Magnetomotive force

NdFeB	Neodymium-iron-boron
OD	Outer Diameter
OFC	Open Fan-Cooled
PE	Piston Engine
PM	Permanent Magnet
PMSM	Permanent Magnet Synchronous Machine
POA	Power Optimized Aircraft
RAT	Ram Air Turbine
SmCo	Samarium-cobalt
SPM	Surface Permanent Magnet
SRM	Switched Reluctance Machine
THD	Total Harmonic Distortion
TIMES	Totally Integrated More Electric Systems
TRUs	Transformer Rectifier Units
VF	Variable Frequency

List of symbols

B_s	saturation magnetic induction strength
B_r	residual flux density
B	flux density
H_c	coercivity
$(BH)_{max}$	maximum energy product
H	magnetic field strength
T	torque
D	rotor diameter
L	axial rotor length
P_{AC}	AC loss
P_{DC}	DC loss
P_{sk}	loss caused by skin effect
P_{pr}	loss caused by proximity effect
P_e	eddy current loss
f	electrical supply frequency
B_m	maximum instantaneous flux density
w	width of PM segmentation
ρ	PM resistivity
θ_e	electrical angle
k_e	equivalent thermal conductivity
k	material thermal conductivity
v	volume ratio of material
v_c	volume ratio of the conductors
v_i	volume ratio of the insulation materials

k_c	thermal conductivity of conductor
k_i	thermal conductivity of insulator materials
k_a	equivalent thermal conductivity of the insulation
v_{ii}	volume ratio of the impregnation insulation
v_{ci}	volume ratio of the conductor insulation

Contents

Abstract.....	i
Acknowledgement.....	ii
List of Figures.....	iii
List of Tables.....	ix
List of abbreviations.....	xii
List of symbols.....	xiv
Chapter 1 Introduction.....	1
1.1 Background	1
1.2 Aim and objectives	2
1.3 Contribution to knowledge	2
1.4 Thesis overview	3
1.5 Publication	4
Chapter 2 The more electric aircraft.....	5
2.1 Introduction	5
2.2 Aircraft power system layout	6
2.2.1 Traditional aircraft system	6
2.2.2 The MEA system	7
2.3 MEA advantages	8
2.4 Current research on MEA	9
2.4.1 A380 electrical system	9
2.4.2 Boeing 787 electrical system	11
2.5 More Electric Helicopter development	12
2.5.1 The helicopter	12
2.5.2 Helicopter configurations	13

2.5.3	More electric helicopter.....	16
2.5.4	More Electric Helicopter layout	18
2.5.5	Design challenges of electric tail rotors.....	19
2.6	Current research on helicopter electric tail rotor system	19
2.7	Fault tolerance	22
2.7.1	Fault-tolerant motor	22
2.7.2	Fault-tolerant drive system	22
2.8	Thermal management.....	24
2.8.1	Forced air cooling	25
2.8.2	Forced liquid cooling	27
2.8.3	Hybrid cooling.....	28
2.9	Conclusion.....	28
Chapter 3 Electrical machine design		30
3.1	Introduction	30
3.2	Electrical machine topology	30
3.3	Benchmark design.....	32
3.3.1	Materials	33
3.3.2	Finite element analysis and Simcenter MagNet software	36
3.3.3	Motor requirements and preliminary design.....	37
3.4	Geometry optimisation	38
3.4.1	Ratio of rotor yoke thickness to PM pitch	39
3.4.2	Ratio of the stator yoke thickness to PM pitch	40
3.4.3	Ratio of tooth pitch to PM pitch	41
3.5	Optimisation of power density with constant output.....	42
3.6	Conclusion.....	46
Chapter 4 Loss analysis		47

4.1	Introduction	47
4.2	Winding loss	47
4.3	PM loss	51
4.3.1	Surface-mounted PM motor VS Interior PM motor	52
4.3.2	The surface-mounted PM motor	53
4.3.2.1	Segmentation of surface-mounted PM motor	53
4.3.2.2	Time harmonic effect	55
4.3.3	Optimization methods	57
4.3.3.1	Introduction of a Conducting Rotor Shield	58
4.3.3.2	Rotor cage in q axis	60
4.3.3.3	Rotor cage on the d-axis and q-axis	63
4.3.3.4	Three-phase rotor cages over PMs	66
4.3.4	The interior PM motor	69
4.3.4.1	Circumferential segmentation	70
4.3.4.2	Axial segmentation	71
4.3.4.3	The model with rotor cage	72
4.3.5	Comparison	74
4.4	Conclusion	75
Chapter 5 Harmonic analysis and fault tolerant operation		76
5.1	Introduction	76
5.2	Harmonic analysis	76
5.2.1	Analysis of the proposed model	76
5.2.2	Motor with 48 slots and 32 poles	79
5.3	Fault-tolerant design	81
5.3.1	A comparison between two fault-tolerant designs	81
5.3.2	Key parameters design	82

5.3.3	Healthy operation simulation of the Fault Tolerant Design	85
5.3.4	Three phases terminal fault	86
5.3.5	Fault current	87
5.4	Conclusion	88
Chapter 6	Thermal analysis	90
6.1	Introduction	90
6.2	Thermal analysis approaches	90
6.3	Benchmark design and software setting	91
6.4	Air cooling optimization	98
6.4.1	Air flow velocity	98
6.4.2	Width of the air channel	101
6.4.3	Shape of the air channel	103
6.5	The influence of air turbulence intensity	105
6.6	Hybrid cooling	106
6.6.1	Model design	107
6.6.2	CFD simulation results	108
6.7	Conclusion	110
Chapter 7:	Prototype manufacturing and thermal experiment	111
7.1	Introduction	111
7.2	Experimental preparation	111
7.2.1	Test model for air cooling	111
7.2.2	Base, pillars, and 3D printed tooth units and winding blocks	112
7.2.3	Test model for hybrid cooling	114
7.2.4	Calculation of coil resistance	116
7.2.5	Changes to CAD model for thermal simulation	116
7.3	Tests and results	117

7.3.1	Pressure test.....	117
7.3.2	Test rig setup in wind tunnel	117
7.3.3	Results analysis	120
7.3.4	Varnish sealed windings.....	123
7.4	Conclusion.....	123
Chapter 8 Conclusion and Future Work		124
8.1	Conclusion.....	124
8.2	Future work	124
Reference		126

Chapter 1 Introduction

1.1 Background

The transportation sector is considered responsible for more than 20% of global CO₂ emissions. Moreover, the global aviation industry contributes around 2% of global CO₂ emissions from human activities, according to the Intergovernmental Panel on Climate Change [1]. Traditional aircraft modes are becoming increasingly problematic in the face of global warming, air pollution, and energy constraints. Among the most critical challenges to reducing the environmental impact of aviation are aircraft mass and fuel consumption. For total aviation traffic, one less kilogramme per aircraft saves roughly 1700 tonnes of fuel and 5400 tonnes of CO₂ emissions per year [2]. To keep up with the global economic development trend, governments, universities, and corporations aim to develop new energy modes of transportation. Electric motors and associated drive systems are critical components of new energy modes, such as electric-, hybrid-, and fuel cell-driven transportation.

The More Electric Aircraft (MEA), which prioritises the use of electrical systems throughout the aircraft while minimising the need for traditional power like hydraulic, pneumatic, and mechanical systems, has many claimed benefits that are far from new [3]. MEA has become a well-known alternative for enhancing aircraft performance, increasing reliability, decreasing operating and maintenance costs, reducing greenhouse gas emissions and offering safe services and a comfortable environment [4]–[6]. Meanwhile, the development of power electronic systems, fault-tolerant motors and fault-tolerant electrical systems is attracting more interest in the development of MEA [4].

In addition, the MEA concept has an impact on helicopter technology. However, because of the power constraints of motors and batteries, an all-electric propulsion system, which is popular for many small-scale rotorcrafts and multirotor platforms, is not feasible for full-scale rotorcrafts [8]. Therefore, the proposed hybrid propulsion systems in [9]–[11] will be a viable option for helicopters. With parallel and series designs, the electric drive can be applied for the tail rotor or both the main and tail rotors. Electric drives provide equivalent performance and weight to mechanical links, including various shafts and gearboxes, but significantly reduce maintenance costs, boost operating flexibility and provide future advancements to the current system.

As the central component of the electric drive system, the motor is critical to the overall driving performance of the system. However, because of the size of air transportation and the operational environment, the high-performance requirements of these motors exert more substantial demands on motor design and analysis than industrial motors.

1.2 Aim and objectives

This research aims to develop a fault-tolerant PM motor for helicopter Electric Tail Rotor (ETR) systems. Furthermore, a novel cooling mechanism is required to increase the system's competitiveness.

The specific objectives of this research are as follows:

- 1) Design and analyse a PM Synchronous Machine (PMSM) with high power, torque and current densities, and which is fault tolerant.
- 2) Study and optimise the PM losses by adding a rotor copper cage.
- 3) Evaluate the machine performance in normal operation and fault mode.
- 4) Investigate the effects of airflow velocity, air turbulence intensity and air channel size between coils on air cooling performance.
- 5) Design a distinct hybrid cooling topology by CFD simulation.
- 6) Validate the thermal simulation results experimentally.

1.3 Contribution to knowledge

Based on the knowledge gathered, the study has made the following contributions:

- 1) Proposing a proper PM motor for the electric tail rotor of a helicopter.
- 2) Through the study of the rotor copper shield, the rotor cage is presented and compared.
- 3) The fault-tolerant design was carried out on the proposed motor and was verified in simulation.
- 4) Demonstrating the air-cooling performance under different conditions such as air turbulence intensity, and the width and shape of the air channel.
- 5) A new hybrid cooling system is proposed and simulated for the first time.
- 6) constructing and testing the proposed new hybrid cooling system in the wind tunnel, validating its superiority.

1.4 Thesis overview

The structure and content of this thesis are as follows:

Chapters 1 and 2 provide a literature review of electric drive systems for helicopters. Firstly, the concepts of MEA are introduced along with several advantages when replacing the mechanical, hydraulic and pneumatic systems with electric drive systems. The principle of the fault-tolerance electric machine system is then presented. Then, considering high power density and reliability, the benefits and drawbacks of different cooling methods are proposed and compared.

Chapter 3 presents a benchmark design of the PMSM with high current and power densities.

Chapter 4, according to the design from Chapter 3, analyses and reduces the PM and winding losses, which contain AC and DC losses. The optimisation approach for the PM loss with a rotor cage is designed, studied, and compared for two alternative PM machine structures – surface permanent magnet (SPM) and interior permanent magnet (IPM).

Chapter 5 analyses and compares the non-synchronous winding harmonics of motors with different pole-slot combinations, then two fault-tolerant models are proposed and analysed in comparison, and finally a suitable design is selected.

Based on the optimised PM machine, Chapter 6 uses CFD simulation to calculate the temperature rise in the stator. The cooling performance is determined while considering the effect of the airflow velocity, air turbulence intensity, as well as various sizes and forms of air channels between coils. Finally, hybrid cooling options that involve copper pipes inside the windings are devised and compared to reduce the hot spot temperature in the coil centre.

Chapter 7 discusses the construction of the experimental platform and the manufacturing of the tested models. Meanwhile, the cooling performance of air cooling only and hybrid cooling is investigated in the wind tunnel to validate the CFD simulation results presented in Chapter 6.

Chapter 8 offers a summary of this research and conclusions, as well as a consideration of future research feasibility.

1.5 Publication

In addition to this thesis, this work has resulted in various publications that have been presented at international conferences:

Q. Li, X. Shen, B. Mecrow and X. Deng, "Hybrid Cooling Design of Permanent Magnet Synchronous Machines," The 10th International Conference on Power Electronics, Machines and Drives (PEMD 2020), 2020, pp. 395-400, doi: 10.1049/icp.2021.1044.

Q. Li, B. Mecrow, X. Shen, X. Deng and M. Ikhlaiq, "Design and analysis of a cooling system for permanent magnet synchronous machines," 11th International Conference on Power Electronics, Machines and Drives (PEMD 2022), 2022, pp. 141-145, doi: 10.1049/icp.2022.103

Chapter 2 The more electric aircraft

2.1 Introduction

Following realisation of the electric vehicle concept, the MEA concept is offered with the goal of replacing its mechanical, hydraulic, or pneumatic precursors with an electric system. Electrification of aircraft actuation was first proposed in 1916 [13]. Electrical power was then employed for significant flight controls and other functions to aid pilots as aircraft speed and size increased throughout the Second World War [14]. There are four types of secondary power systems, which are standard on aeroplanes around the world [15], [17]:

- Mechanical power system: this transfers engine power to hydraulic pumps, local pumps for engine equipment and other mechanically powered subsystems, as well as the primary electrical generator, via the mechanical gearbox.
- Hydraulic power system: this transfers power from the central hydraulic pumps to the actuation functions, such as for primary and secondary flight control, landing gear, engine actuation and a variety of other systems.
- Pneumatic power system: this uses high-pressure engine compressors to power the environmental control system, which includes air conditioning, pressurisation, and wing ice protection.
- Electrical power system: this obtains power from the main generator to power the avionics and utility services, including cabin and aircraft lights, galleys, and other commercial loads (such as entertainment systems).

Electrical power, now established as a secondary power source to support electronic and utility services, initially struggled to acquire traction due to limitations such as lower power density [14], [16]. Through improvements in permanent magnetic materials, semiconductor materials, and power electrical drive control techniques in the 1970s, the electrical power system came to provide several benefits over mechanical, hydraulic, and pneumatic systems, such as safer operation [7].

Around the early 1980s, the aerospace industry began to adapt electrical power for equipment where it was technically feasible and advantageous [14]. Several programmes, such as the Totally Integrated More Electric Systems (TIMES), the US Air Force MEA Program, and the Power Optimized Aircraft (POA), were launched in the 1990s to

investigate the application of electrical systems and optimisation of electrical power management to reduce fuel consumption and maintenance costs while increasing reliability and safety [15]. Figure 2-1 depicts the progression towards MEA.

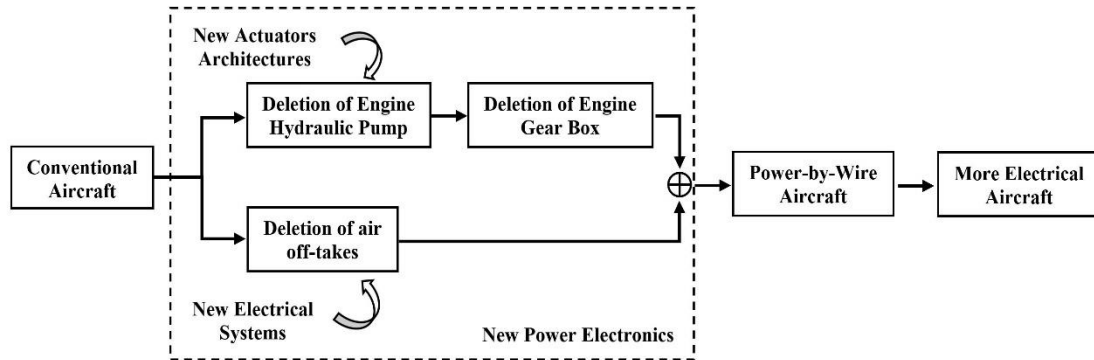


Figure 2-1: The trend toward the MEA [15]

Currently, both the Boeing 787 and the Airbus 380 (A380) feature substantially bigger electrical systems than prior aircraft, resulting in a plethora of technological advancements [15], [18]. Electrical systems are now replacing other secondary power systems in aircraft actuation systems, wing ice protection, environmental control systems, and fuel pumping, making aircraft more fuel-efficient and quieter [17]–[19], [77].

2.2 Aircraft power system layout

2.2.1 Traditional aircraft system

In conventional civilian aircraft, the gas turbine engines, as shown in Figure 2-2, provide thrust for the flight as well as power all other loads on the plane (mechanical, pneumatic, hydraulic, and electrical) [20], [21]. The earlier secondary power systems have several drawbacks as they grow more complicated, such as low efficiency, and it can be difficult to identify breaches in the pneumatic and hydraulic systems due to a heavy and inflexible infrastructure, and the possibility of harmful fluid leakage [15]. Because interactions between numerous pieces of equipment lower the overall efficiency of the systems, streamlining to a single type of power source derived from aircraft engines will be more effective.

A leak in a pneumatic or hydraulic system would result in a network outage for all equipment, and access to the location can be difficult [15]. Eliminating pneumatic, mechanical, and hydraulic components might hence significantly enhance engine

performance and reduce overall weight, lowering fuel consumption. Consequently, electrical power was chosen as the primary source since it offers various benefits in terms of versatility and application range (from low-power avionics to high-power actuators) [20]. Furthermore, the enhanced prognostics and diagnostics provided by electrical systems increase aircraft availability and decrease the need for unexpected maintenance [17], [22].

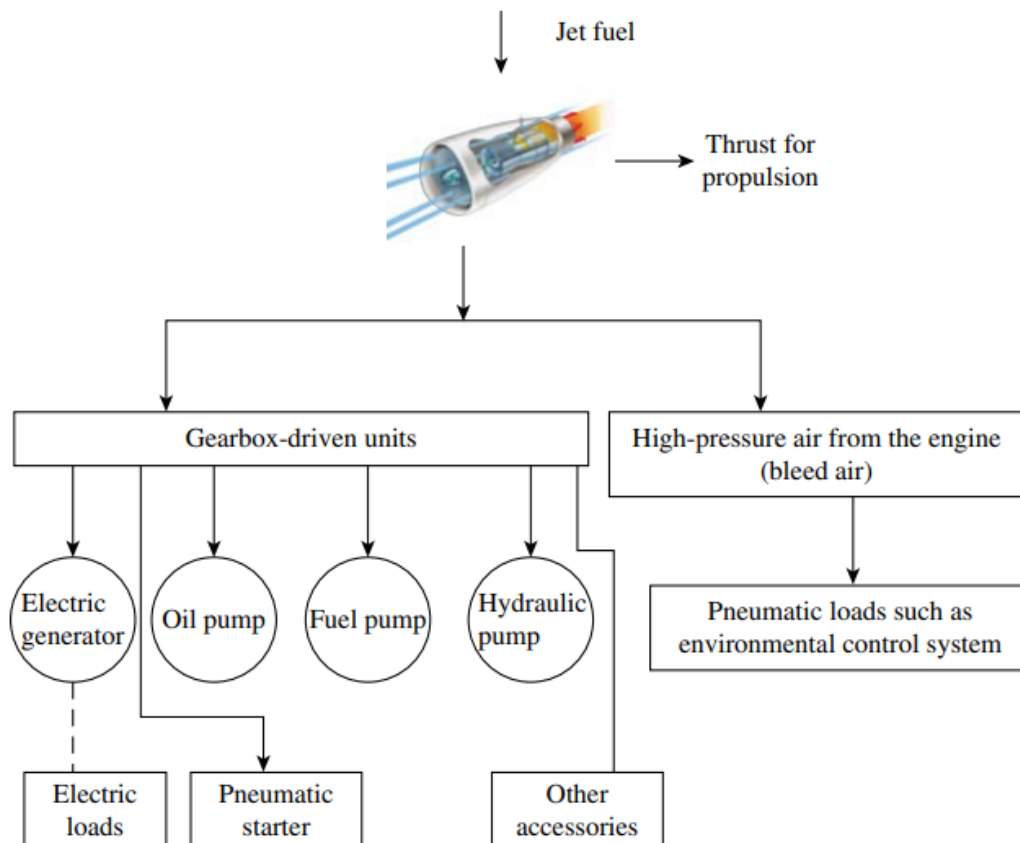


Figure 2-2: Power sources on a conventional civilian aircraft [21]

2.2.2 The MEA system

The gas turbine engines in an MEA system provide thrust and electric power, as shown in Figure 2-3. Electric motors power most of the system's loads, including hydraulic, fuel, and oil pumps, as well as environmental control and de-icing systems. Generators can be placed on the exterior of the engine and connected to the main shaft through gearboxes or mounted coaxially with the shaft to start the engine and generate electric power [20].

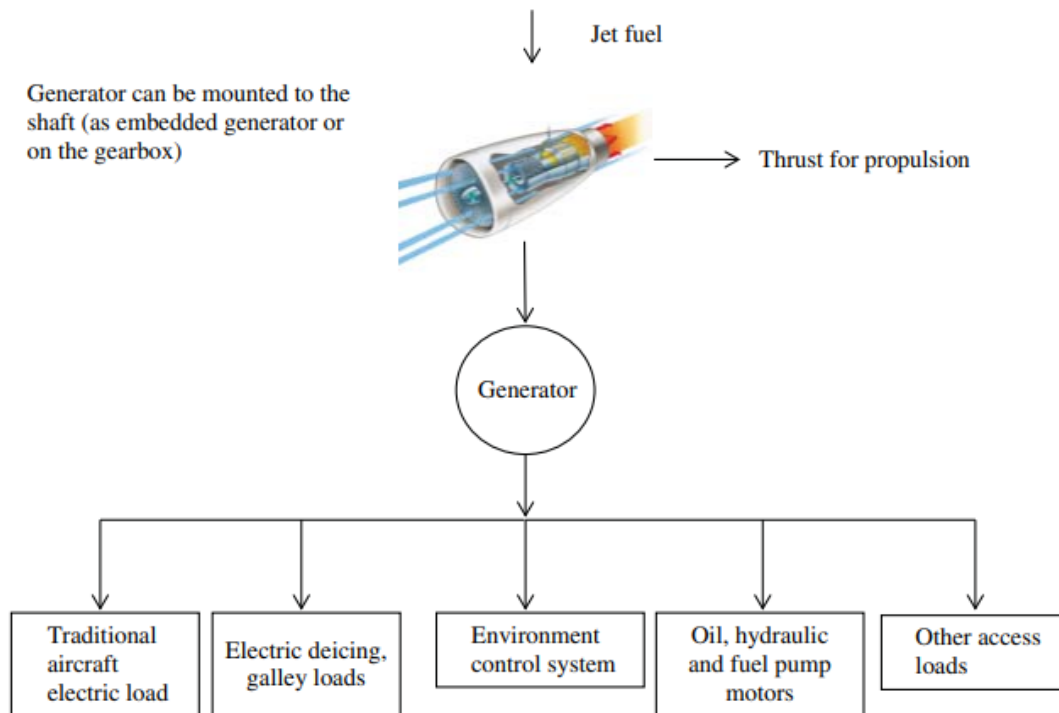


Figure 2-3: Concept for the power sources on an MEA [21]

2.3 MEA advantages

Adopting MEA can provide the several primary advantages. First, eliminating hydraulic systems improves aircraft reliability while also reducing complexity, redundancy, weight, installation, and maintenance costs [23], [24]. Second, replacing the engine-bleed system with electric motor-driven pumps simplifies installation and lowers costs [5]. Third, using the engine starter/generator to start the aero-engine eliminates the engine tower shaft and gears, power take-off shaft, and auxiliary gearboxes, and reduces engine starting power, especially at low temperatures [25]. Fourth, electrical systems are generally more efficient than hydraulic and pneumatic systems because traditional, centralised systems remain energised throughout the flight, whereas electrical systems provide the precise function required without concerns about excess or reduced power being supplied to the loads [7]. Meanwhile, the MEA increases the efficiency of power distribution, and reduces the required power rating of the wiring by shortening the distances between generation and consumption [26]. Additional advantages include:

- Reliability (easier and faster failure isolation [12], easier to monitor and observe performance trends [21], 15% reliability improvement [30]).

- Flexibility (power generation and distribution close to the load [5]).
- Easier and safer control [27].
- Reduced noise.
- Less maintenance [12] (Up to 4.2% reduction in maintenance man-hours per flying-hour [28]).
- Reduced environmental impact (fuel savings and reduced hydraulics).
- Reduced weight (Up to 6.5% reduction in take-off gross weight [28]).
- Allowing for the installation of sophisticated entertainment systems, seat comfort, and other features.
- Fewer constraints regarding certification of aircraft for commercial use.
- Reduced ground support.
- Eliminates high-temperature ducts and inflammable fluids required in a traditional aircraft [21].
- Enables faster diagnostics and better prediction of potential failures, resulting in less downtime [29].

2.4 Current research on MEA

Airframers, vendors, and the military are all interested in more electric architecture and the associated components/subsystems. On the one hand, replacing most pneumatic and hydraulic systems with electrical systems has realised benefits such as higher fuel efficiency, lower emissions, and increased reliability. On the other hand, the MEA concept places growing demands on the generation, conversion, and distribution of electrical power within the aircraft, resulting in the constant evolution of MEA technologies with plenty of potential for improvement as systems are refined and enhanced. As a result, the MEA concept is widely recognized as the technological direction for the aerospace industry. The A380 and Boeing 787 are two major aircraft programmes that demonstrate how electric power production and increased usage of power electronics can be accomplished in an aircraft.

2.4.1 A380 electrical system

The A380 was the first large civil aircraft to feature a more electric architecture system with variable frequency (VF) power generation [21], [32]. The maiden flight of the first A380 took place on 27 April 2005. The aircraft, equipped with Rolls-Royce Trent 900

engines, took off from Toulouse–Blagnac International Airport with a crew of six, and landed successfully after 3 hours and 54 minutes. The A380 aircraft is currently operating on scheduled flights with different airlines [33].

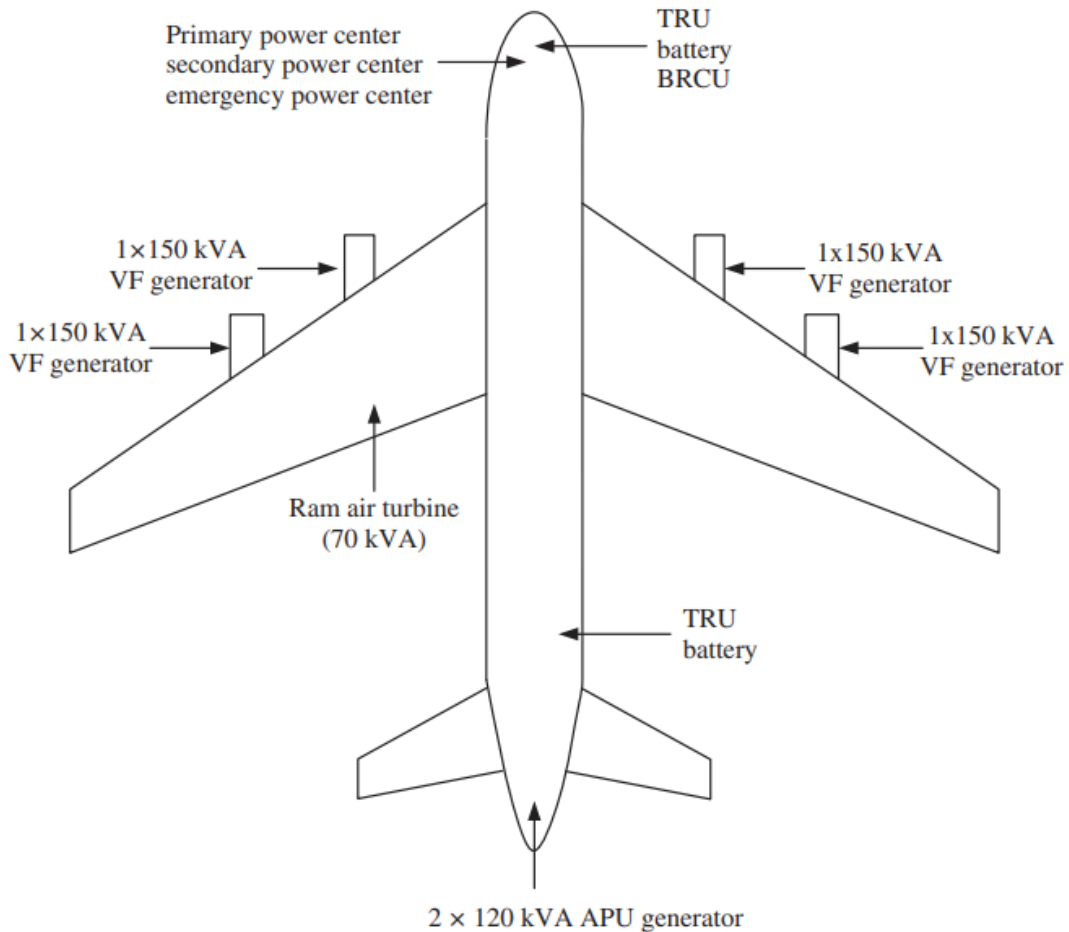


Figure 2-4: A380 electrical power system components [21]

The A380 electrical system components are shown in Figure 2-4. These comprise four 150 kVA VF generators (370–770 Hz), two constant-frequency auxiliary power unit (APU) generators (nominally 400 Hz), one 70 kVA ram air turbine (RAT) for emergency purposes, and four external power connections (400 Hz) for ground power.

Each of the main generators is driven by its associated engine, and supplies power to the appropriate AC bus. However, because the generators' output frequencies depend on the varying speeds of the engines driving them, the several AC buses cannot be connected in parallel. Each generator is, therefore, controlled by its respective generator control units, as are the two APU generators. There are three Battery Charge Regulator Units (BCRUs), which are based on regulated Transformer Rectifier Units (TRUs) connected to the AC

bus. The AC bus also provides power to the galley loads. Meanwhile, the main AC buses can accept ground power input for on-the-ground servicing and support.

2.4.2 Boeing 787 electrical system

The Boeing 787 has most of the features of an MEA system [21], [31], [32]. The Boeing 787 made its maiden flight on 15 December 2009 and completed flight testing in mid-2011. The aircraft entered commercial service on 26 October 2011.

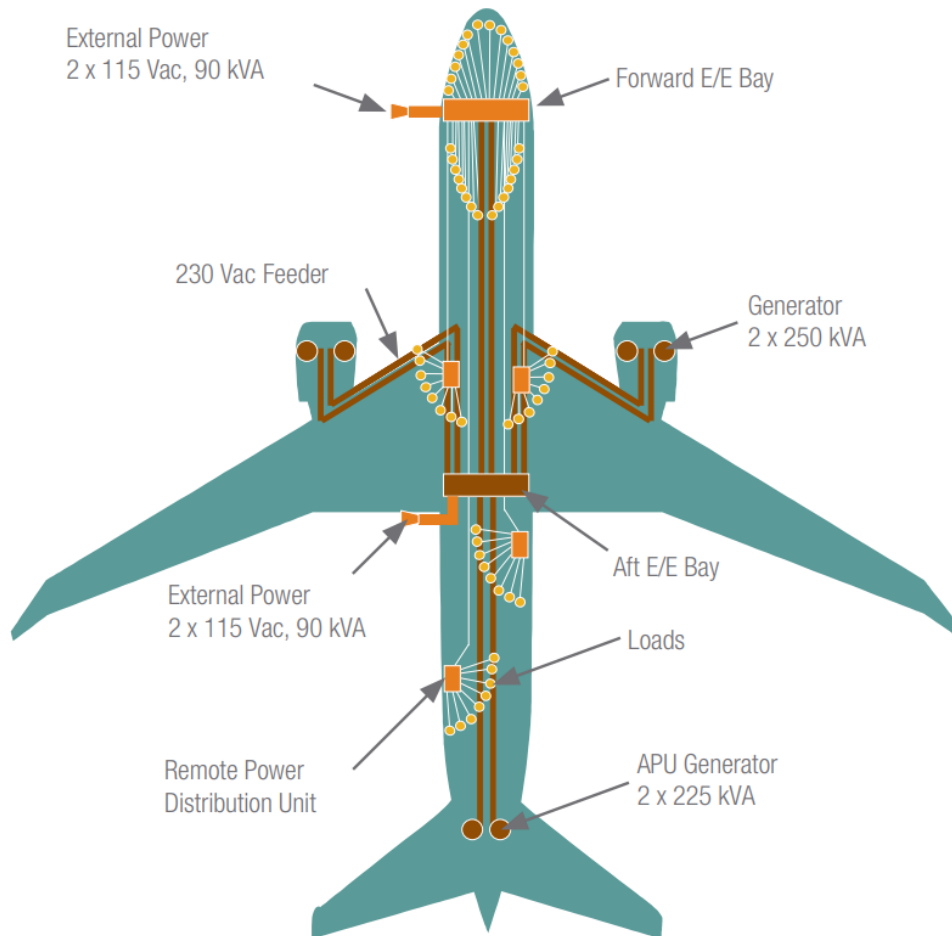


Figure 2-5: Boeing 787 electrical power distribution system (physical locations)

[31]

The electrical power distribution system is shown in Figure 2-5. The system includes six generators — two per engine and two per APU — operating at 235 V AC for reduced generator feeder weight. The system also includes ground power receptacles for airplane maintenance on the ground without using the APU. The bleed air is not used in the airframe, so the environment control system, cabin pressurization system, wing anti-ice system and other conventionally pneumatic power systems are all powered electrically.

The only bleed air used from the engine is low-pressure fan air used for anti-icing the engine cowl. The main electrical loads are as follows:

- Environment control system and cabin pressurisation system which contain four electric compressors.
- Electrically heated cargo bay.
- Four 100 kVA electrical motor pumps for the cooling loop of high-power motor controllers and galley refrigerators.
- Wing de-icing.
- Flight controls.
- Electric brakes.
- Landing gear.

2.5 More Electric Helicopter development

2.5.1 The helicopter

The helicopter's rotating wings provide all three of lift, propulsion, and control. Figures 2-6 and 2-7 illustrate the principal helicopter configurations. The rotor blades rotate around a vertical axis, tracing out a disk on a horizontal, or nearly horizontal, plane. Aerodynamic forces can be generated by helicopters with rotary wings even when the speed of the craft itself is zero. The helicopter, therefore, is capable of vertical flight, including vertical take-off and landing [34].



Figure 2-6: UH-60A single main rotor and tail rotor helicopter



Figure 2-7: A tandem main rotor helicopter – Boeing CH-47 Chinook

Helicopters are widely used in military, fire rescue, resource detection, tourism, communication and other fields because of their high mobility, hovering, vertical take-off and landing, and near-ground flight characteristics [35].

2.5.2 Helicopter configurations

Power is transmitted to the rotor via the shaft and is accompanied by torque. Measures are required to balance the torque effect on the helicopter because there are no forces or moments acting on it while in steady flight. Generally, there are two ways to achieve this: a single main rotor plus tail rotor configuration, and a twin contra-rotating rotor configuration.

2.5.2.1. Configuration with a single main rotor and a tail rotor

Helicopters with a single main rotor require a separate auxiliary rotor to balance torque and yaw control as shown in Figure 2-8. The compensating torque is created by the tail rotor thrust acting about the main rotor shaft. The main rotor provides lift, propulsive force, and roll, pitch, and vertical control. There are three most common auxiliary rotors configurations used to balance the torque [36], [38]:

- The tail rotor
- Fenestron
- The NOTAR

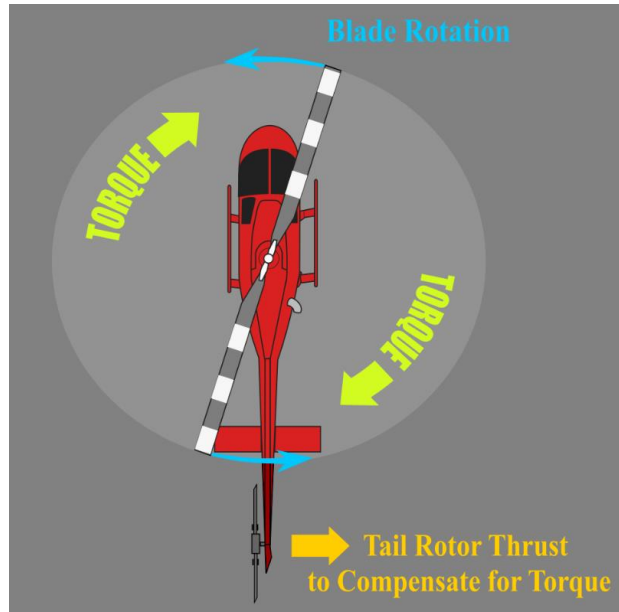


Figure 2-8: Torque effect on the helicopter

The tail rotor is a small rotor mounted on the tail boom as shown in Figure 2-6, usually slightly beyond the edge of the main rotor disk. The tail rotor is vertical and with a horizontal shaft. It develops thrust in a direction perpendicular to that of the main rotor to balance the torque created by the main rotor. In addition, it allows the pilot to rotate the helicopter around its vertical axis to change the orientation of the craft.



Figure 2-9: Fenestron tail rotor – EC120B [37]

An alternative tail rotor configuration is the Fenestron [37] in which a ducted fan at the end of the tail boom replaces the tail rotor as illustrated in Figure 2-9. Compared with the typical tail rotor, it has a smaller diameter and is run at a higher speed. This configuration offers several advantages such as reduced noise and vibration, lightness and smallness rotor, enhanced efficiency, and increased safety by reducing the chance of a tail strike. However, it has disadvantages such as increased weight, cost, and power during the hover.



Figure 2-10: NOTAR – MD Explorer air ambulance [114]

Another configuration is the NOTAR which does not involve the tail rotor, as shown in Figure 2-10. It was developed by McDonnell Douglas Helicopter Systems. This system outputs a high volume of low-pressure air generated by a fan inside the tail boom through slots, and exploits the Coanda effect to create a boundary layer to modify airflow around the tail boom. This compensates for the main rotor torque. Meanwhile, the directional yaw control is obtained by a vented drum at the end of the tail boom. This configuration also provides benefits such as reduced noise and improved safety, while requiring a larger tail boom than the conventional one.

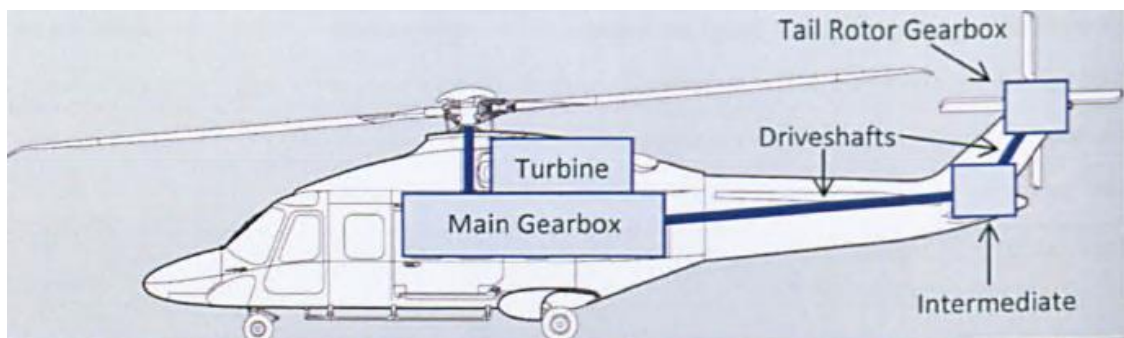
2.5.2.2. Configuration with twin contrarotating rotors

A twin main rotor configuration uses two contrarotating rotors of the same size and loading, which produce the torque of the same magnitude but in opposing directions. As a result, there is no net torque on the helicopter in forwards flight and hover. The

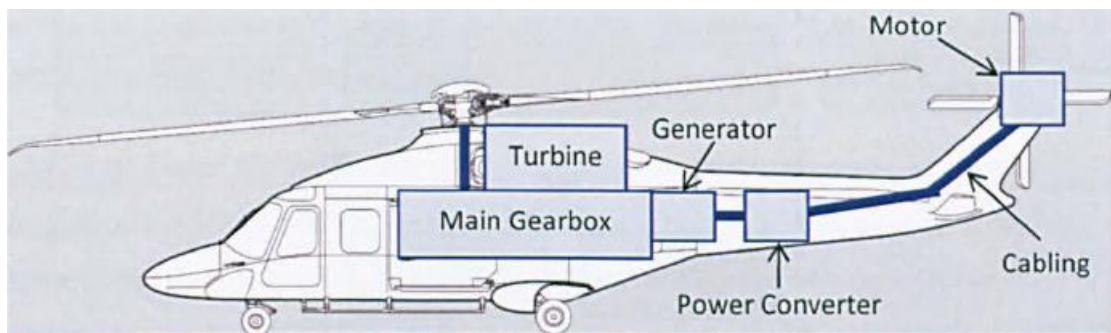
directional yaw control is gained by creating a torque difference between the two main rotors.

2.5.3 More electric helicopter

Minimising embedded mass and fuel consumption while meeting instantaneous load power requirements is mandatory for designing operational helicopters [39]. Notably, the electrification of helicopter propulsion is considered a promising approach for meeting these requirements [11], [40]. Pure-electric and hybrid electric propulsion systems have been proposed [41]-[42]. However, hybrid electric propulsion systems have longer flight times than pure-electric systems due to the energy density of traditional fuels in combination with a smaller battery (which can be relatively heavy). Thus, secondary power supplies can avoid oversizing the main power supply and optimise the management of transient energy [39]. Furthermore, for helicopters with a single main rotor, the battery allows for a few minutes of additional power in the event of mechanical engine failure [10].



(a) Traditional mechanical tail rotor configuration



(b) Electrical tail rotor configuration

Figure 2-11: Tail rotor configurations [43]

Figure 2-11 shows the traditional tail rotor configuration and ETR configuration. The ETR system replaces the driveshafts and tail rotor gearbox with a generator, power converter, cabling and motor.

There are numerous differences between mechanically driven and electrically driven tail rotor systems. The conventional helicopter tail rotor system, the foundation of helicopter research, is a system powered mechanically by a series of high-speed shafts and gearboxes, which are the only connection between the tail rotor and the main transmission. The thrust of the tail rotor fan is generated by the different pitch angles of the rotor blades. Considering the operation behaviour and failure modes, the power draw of the mechanically driven tail rotor system is determined by the working conditions of the tail rotor and the main transmission, which acts as a constant speed power source. Once the power demand for the system increases, the rotating tail rotor will stall, and thus the power transmitted from the main mechanical transmission should be readjusted. The stall of the tail rotor is a dangerous operational state that needs to be avoided. However, the electrically driven system is controlled by the power converter and its controller. The inner control loop of an electrical drive is the current loop, designed to ensure the system obtains the required torque, and its outer loop is designed to control the speed by adjusting the torque demand according to the speed difference. Hence, the shifting aerodynamic load is monitored, and the rotor speed can be adjusted instead of stalling [43]. Therefore, the electrical drive system is more controllable and reliable compared to the mechanical system.

The electrification of the helicopter tail rotor system is desirable due to several well-known advantages when compared to the conventional mechanical system [9],[41], such as:

- The increase in reliability and fault tolerance
- The increase in operational efficiency
- Reduction of emissions
- Reduction of energy consumption
- Reduced noise
- Simplifying the operation

2.5.4 More Electric Helicopter layout

Potential powertrain layouts for helicopters are discussed in [9], which include hybrid and electric propulsion systems, as shown in Figure 2-12. It describes the different constructions of the propulsion systems when electrifying the helicopter from the more-electric helicopter to the all-electric helicopter by replacing the mechanical systems with electric systems.

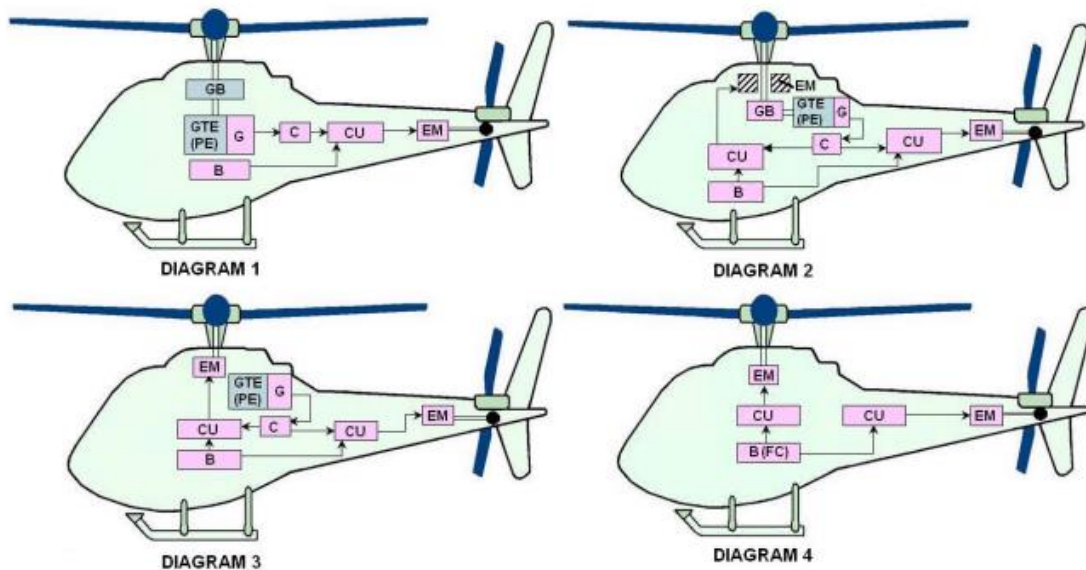


Figure 2-12: Variants of electrification of the helicopter propulsion system [9]

- Diagram 1: In the propulsion system, the drive system of the tail rotor has been converted from a conventional mechanical drive to an electric drive. The gas turbine engine (GTE) or the piston engine (PE) rotates the main rotor through a gearbox (GB). Also, the electric generator (G) is installed on an engine gearbox or built into the engine. The current is supplied through the converter (C) and control unit (CU) to the electric motor (EM) of the tail rotor. The battery (B) is used to supply the emergency power.
- Diagram 2: The hybrid propulsion system consists of a conventional engine (GTE or PE), an electric drive for the tail rotor, a partial electric drive for the main rotor, converters, and control units. The generator is installed on the conventional engine as well. The main rotor is driven by a traditional engine through a gearbox, assisted by the electric motor when the power request is very high [8]. Emergency power is supplied by the battery.

- Diagram 3: The main and tail rotors are fully powered by electricity, but the traditional engine is still used to run one or more generators which are installed on the engine. The battery provides an emergency energy source.
- Diagram 4: In this completely electric propulsion system, the power is provided by the battery or a fuel cell (FC) to supply the electric main and tail rotors.

2.5.5 Design challenges of electric tail rotors

The challenges of designing an optimum PM machine for helicopter applications are listed below:

- fit the environment in which the helicopter operates;
- avoiding mechanical resonance points in the helicopter;
- enhance the reliability of the machine;
- trade-offs between power density, efficiency and weight;
- thermal management.

Because of the harsh operating environment, the electric tail rotor system requires high reliability and safety. Hence, the fault-tolerant PM motor with concentrated windings, which can maintain the operation of the system in fault mode, will be considered. Given the constraints upon motor volume, power density is a significant motor parameter that affects the performance of the whole system. However, power density, efficiency and weight interact with each other, so the trade-offs between these three parameters are always a central concern of machine design. Finally, because the thermal problem cannot be ignored, a forced cooling method has to be investigated in parallel with the machine design process.

2.6 Current research on helicopter electric tail rotor system

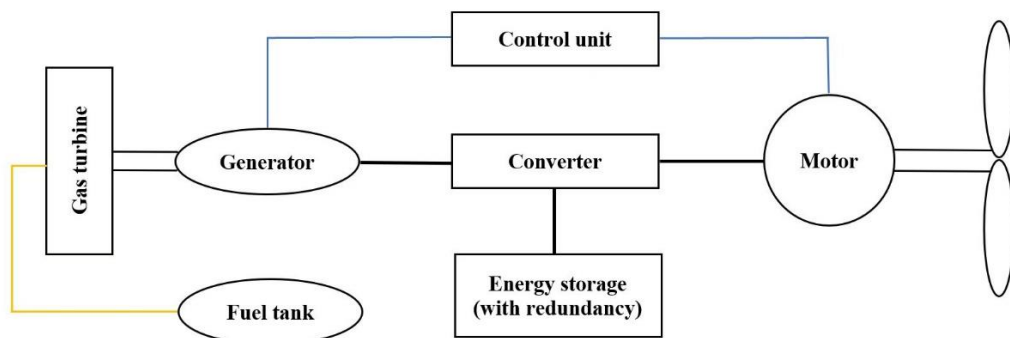


Figure 2-13: Propulsion system topologies of the hybrid electric helicopter [79]

In general, the helicopter ETR drive system, as illustrated in Figure 2-13, consists of various critical components: generator, electric energy storage, power converter, electric motor and control unit. Since the ETR drive system is safety-critical, all components must have high reliability and be fault tolerant [44].

The main power is supplied through the generator installed on an engine gearbox or built into the engine. Additional battery capacity is typically used for the emergency power supply [9]. The generator is the most important part of the power supply system. Thus, a hybrid series-parallel configuration using several independent generators has been proposed, which is the most reliable configuration [45]. Additionally, high-speed surface-mounted PM machines have been developed for direct-drive generators, which have higher reliability, efficiency, power density and compactness, and lower weight, acoustic noise and maintenance costs [46], [47].

A series of designs for PM generators on helicopters was proposed in [76], considering two stators with different winding conductors (copper and aluminium) and three rotors with varying sleeve materials. The authors aimed to optimise system power density, efficiency, and robustness.

In another study, researchers proposed a PMSM topology, as shown in Figure 2-14, without slots and cores on the stator, which was implemented as electric aircraft propulsion [78]. This topology has several advantages [80], such as ease of starting due to the lack of cogging torque [81], limited space occupied by the windings, and low iron loss during high-speed operation [82].

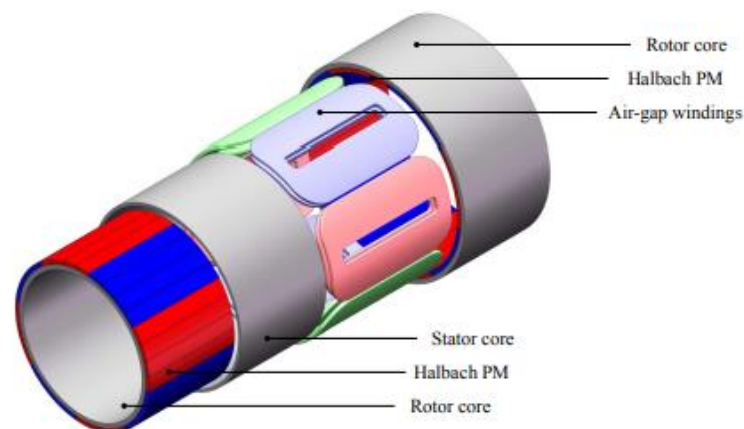


Figure 2-14: Proposed machine with slotless single-stator double-rotor [78]

Furthermore, a three-phase brushless AC (BLAC) PM motor has been proposed, which was designed for a medium-sized twin-engine helicopter [43], [48]. The motor contains four channels, such that the stator coils can be regarded as four independent parts and each part is a star-connected three-phase motor module. Therefore, the interaction between the phase coils can be minimised. However, electrical and thermal coupling occurs between these four channels. Therefore, this current report also considers the analysis of electrical and thermal coupling effects.

Moreover, a six-phase BLAC spoke-type interior PM motor with independent phases was introduced [49]-[51]. These investigations optimised the trade-offs between power density, efficiency and weight during the motor design and focused on electromagnetic and thermal analysis.

In addition, a six-phase BLAC PM motor with an outer rotor and interior stator was proposed [52]. The outer rotor can simplify the assembly of the tail rotor and can be easily maintained or replaced. The paper compared the performance of two different power levels for two different PM motors, which utilised a spoke-type external rotor and a V-shape external rotor.

According to fault tolerance, availability, and performance assessment, authors of [79] used the Lz-transform method to evaluate two options of a hybrid electric traction drive system for a helicopter: a serial electric-hybrid propulsion system with a gas turbine and electrical generator, as shown in Figure 2-13, and a combined electric-hybrid propulsion system with a gas turbine, generator, and speed reducer, as shown in Figure 2-15.

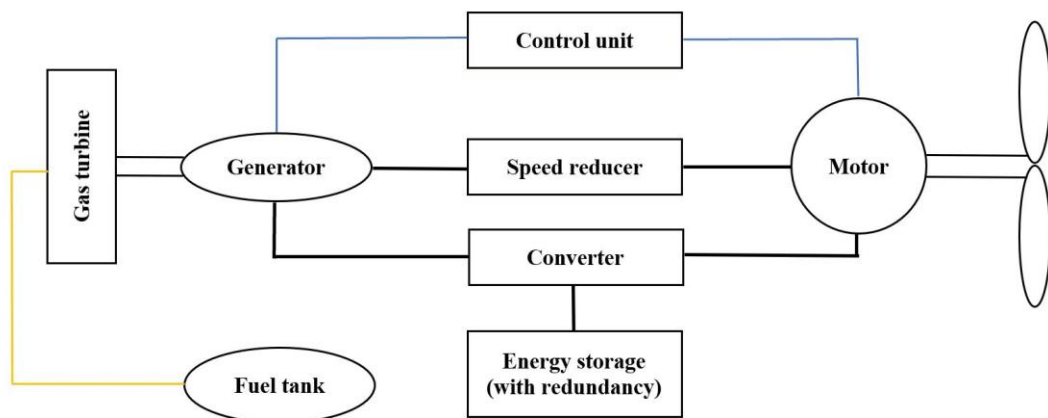


Figure 2-15: Combined propulsion system topologies of the hybrid electric helicopter [79]

2.7 Fault tolerance

It is important for the motor drive system to gain high reliability. A single failure should not result in a reduction in rated torque and power output in critical components, leading to a loss of thrust control or directional yaw control. At the same time, the fault-tolerant motor drive system should be able to detect failing components by means of self-diagnosis and react to ensure proper flight [16].

2.7.1 Fault-tolerant motor

The most important part of the helicopter ETR drive system is the fault-tolerant motor, which needs to match the specific volume and weight. Additionally, the motor needs to efficiently alternate between two working conditions, namely hover operation and forward flight, which are required due to poor flight conditions and regular changes in the flight path [49]. According to these conditions, the PM motors are suitable for ETR applications because they can enable higher power densities and reduce the envelope and weight of the system [16], [53].

The major advantages of PM motors are high power density, efficiency and reliability [47]. For a fault-tolerant PM motor, a single-layer concentrated winding arranged on a stator core can improve the physical, electrical and magnetic performances by minimising mutual inductance and maximising thermal insulation between phases [16], [48], [54]–[57]. Additionally, the windings are concentrated around the teeth, which can reduce the volume of copper from the end-winding [50]. Moreover, to achieve higher reliability, multi-channel drives are considered since each channel can be regarded as an independent module. Multi-channel motors are also more fault-tolerant than conventional three-phase motors [58], [59].

2.7.2 Fault-tolerant drive system

The power converter that transfers the power from the generator driven by the main gearbox to the motor is comprised of a rectifier unit, power electronic switches, filtering components (e.g., DC link capacitor), controllers, cooling, energy storage devices and motor drive inverters [60]. The factors discussed when comparing power converters are:

- Specific power
- Power density
- Efficiency

- Fault tolerance

For the application of ETRs, the power converter will receive an AC waveform from the generation system and supply an AC waveform to the motor. To improve the fault tolerance of the drive system, two types of drives have been developed: multiple three-phase drives [61], [62] and multiple single-phase drives [63], [64].

For multiple three-phase drives, the most common converter topology is the rectifier-inverter, as shown in Figure 2-16. The rectifier-inverter performs AC-DC-AC conversion with a DC intermediate stage. This type of power converter is mostly used for multi-channel electric systems.

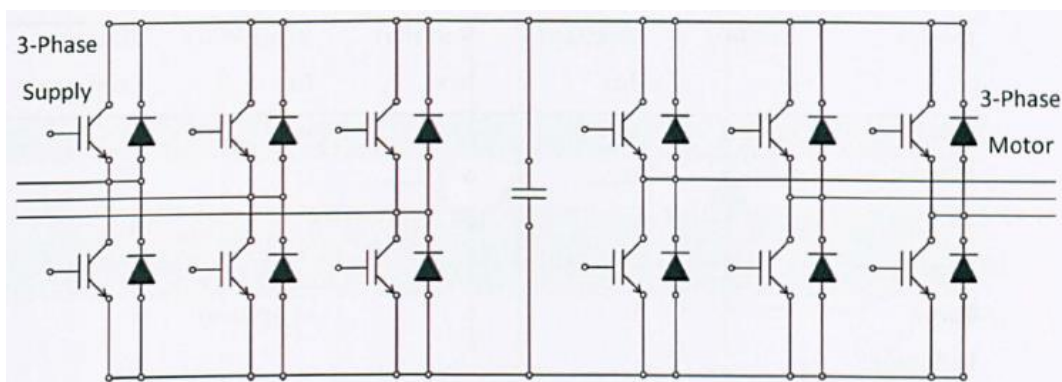


Figure 2-16: Three-phase voltage source rectifier-inverter topology diagram

For multiple single-phase drives, the topology is the H-bridge converter, shown in Figure 2-17. It connects each motor phase independently to a DC source using four switches. The H-bridge motor drive topology provides better electrical isolation of the phases, which improves fault tolerance. This type of power converter is mostly used for multi-phase electric systems.

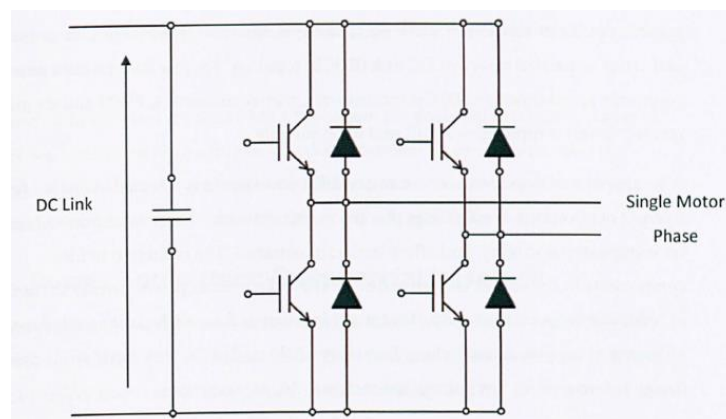


Figure 2-17: Single-phase H-bridge inverter diagram

The determination of the most suitable converter topology is affected by the machine topology it will be driving. More fault-tolerant converter topologies can further improve the motor-inverter fault performance.

2.8 Thermal management

MEA aims to replace the conventional mechanical and hydraulic system with an electric system, seeking reduced emissions and noise; higher reliability; lower production, operational, and maintenance costs; and higher power density and efficiency. An electric machine used in electric aircraft needs to be highly loaded to minimise the mass, irrespective of its use, i.e. actuation or propulsion. Therefore, a high current density is desirable, but overheating should be avoided as it reduces the life of the insulation material and degrades the rotor magnet performance, resulting in lower output torque, efficiency, and overall life [68]. Every 10°C temperature rise can shorten the insulation life by half [73], which means a lower operating temperature efficiently increases the machine's lifetime. Moreover, the limited space for electrical machines on MEA makes the cooling design even more challenging. Therefore, an effective and efficient thermal design is critical to reduce internal temperature rise and thermal cycling.

Several key factors affect the efficiency of the heat transfer from the inner electric machine to the external ambient environment: heat transfer type; system geometry, including the contact area and cooling channel of the machine; coolant choice; fluid velocity; and fluid temperature. Based on the different modes of heat transfer, the cooling for electric machines can be classified as conduction, natural convection, forced convection, radiation, or evaporative cooling.

Natural convection is a simple method to remove heat from machines. To improve the cooling performance, fins on the housing are considered to increase the heat transfer surface area. Then, by the increased machine output power, a forced air cooling system is considered to further improve cooling performance. In this system, a fan or blower is applied to enhance heat transfer from hot spots, such as windings and PMs, to the housing and then to the ambient environment.

For high current density machines, forced liquid cooling can improve cooling efficiency since forced air cooling cannot remove adequate heat, causing hot spots. As a result, better cooling performance allows for higher machine output power at the cost of higher

cooling system complexity and energy costs. Table 2-1 lists typical rules of thumb for cooling technology and associated heat transfer coefficients [92], [94]. For the natural convection, although it has lower heat transfer coefficients and cooling efficiency, it is the popular cooling method to be considered because of its low energy consumption and simplicity of construction. The forced cooling method, especially forced liquid cooling, has higher heat transfer coefficient which results in higher cooling efficiency. However, because of its higher energy cost and complexity system, it is widely used in high power density system.

Table 2-1: Rules of thumb for cooling type and heat transfer coefficients [92], [94]

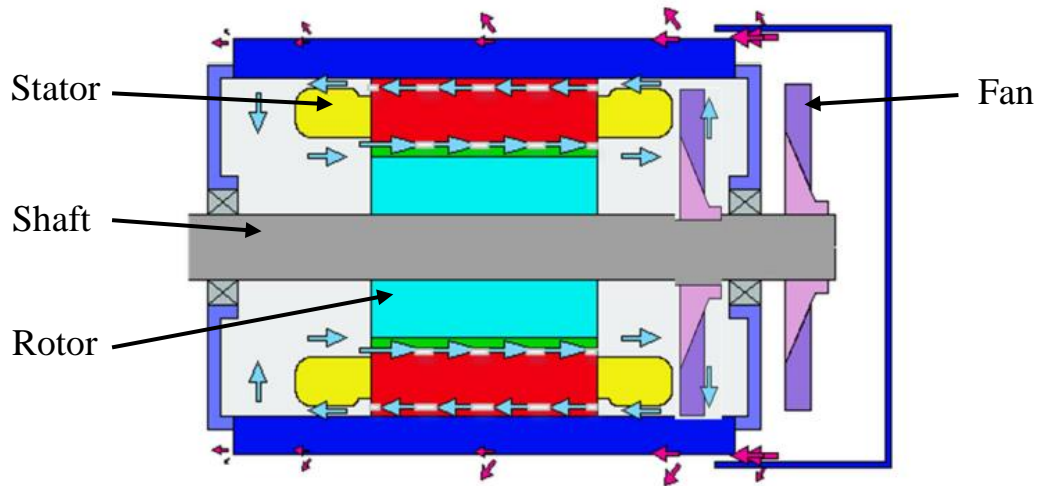
	Current density range (A/mm²)	Heat transfer coefficient (W/(m²·K))	Cooling efficiency	System complexity	Energy cost
Natural convection	1.5-5	5-10	Low	Simple	None
Forced convection	5-10	10-300	Medium	Medium	Low
Liquid cooling	10-30	50-20 000	High	Complex	High

2.8.1 Forced air cooling

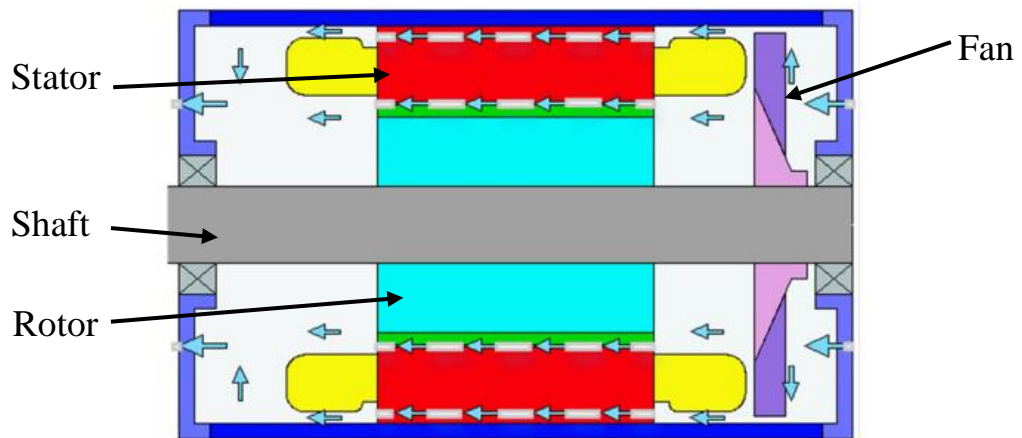
Forced air cooling is a popular method for increasing the heat transfer coefficient at the motor surfaces, owing to its simplicity and economic efficiency [65]. An adequate coolant flow is created by forced air using external equipment, such as a fan or a blower, and power sources. Heat is exchanged and removed from the hotter components. Air-cooled designs generally focus on optimising the internal or external airflow channels through the system to increase the contact area with the air, enhancing heat transfer performance. Two types of motor enclosures are enclosed fan-cooled (EFC) and open fan-cooled (OFC) [72].

An EFC motor [83]–[86], as shown in Figure 2-18 (a), is usually attached to an external fan that blows the coolant toward semi-open fin channels, the design of which has been optimised for the housing [87]. The primary purpose of an EFC motor is to transfer heat to the ambient environment through the coolant over these fins, as shown in Figure 2-19. The effects of different housing geometries and fin arrangements were discussed in [88] and [89]. An internal fan can be added to increase the cooling performance by moving the heat from the inner motor to the housing frame. As a result, more attention has

focused on the optimisation of the housing and shaft designs to increase the contact area with the air and thereby improve the cooling performance [66].



(a)



(b)

Figure 2-18: Ventilation structure: (a) An EFC motor; (b) An OFC motor [72]

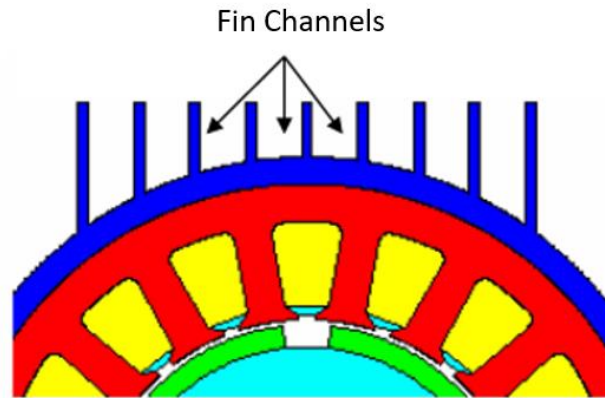


Figure 2-19: Configuration of fin channels [94]

A key benefit of the EFC constructure is that internal parts are better protected against contaminants that can block ventilation ducts and obstruct airflow [72]. Moreover, the air coolant can be replaced with gas with higher heat conduction and specific heat capacity [90]. The gas can significantly improve the cooling performance as its smaller and lighter molecules can lead to lower wind resistance and better heat transfer.

Figure 2-18 (b) illustrates the structure of an OFC motor. This cooling system, usually chosen for economic reasons, continuously draws the coolant air from the ambient environment into the enclosure through vent ducts [65], [95]. However, the motor requires filtration or indirect air channels to prevent environmental contaminants from entering the motor, and regular cleaning operations are necessary every two to three years because of the accumulated pollutants [91], [93].

Moreover, acoustic noise emissions have become a significant challenge associated with forced air cooling, especially when operating with high-speed fans [72]. Several measures to decrease the impact of noise have been proposed:

- Composite materials for blades [74]
- Reduced number of blades [74], [75]
- Irregular-pitch-blade fan [74]
- Mixed-flow (both axial and radial) fan [75]

2.8.2 Forced liquid cooling

Compared with air cooling, liquid cooling can achieve a higher heat transfer coefficient; hence, it is widely used in systems with high power density. The forced liquid can cool the machine through the housing jacket, stator channels, and rotor channels. However,

the forced liquid cooling system has some drawbacks, such as higher manufacturing cost, the requirement for an auxiliary system to provide coolant, and risks of leakage, stains, corrosion, and contamination.

Water-jacket cooling is a common, indirect cooling method that can remove the heat transferred from the inner motor to external surfaces through conduction [96]–[98]. This cooling system has several advantages, including higher-efficiency heat transfer from the stator, lower noise, and a completely enclosed environment [92]. However, it cannot remove sufficient heat from the hot spots, such as stator windings, rotor core, and PMs, because of the high thermal resistance between the source and coolant.

In most cases, liquid cooling is situated within the casing of the system but, on occasion, it may have more direct contact with the winding. Direct liquid cooled systems usually have a more complex geometry, required to accommodate the liquid cooling channels [69]. In addition, liquid cooling can only remove the heat near the liquid cooling channel. Thus, liquid channels located in the casing are not ideal for removing heat from the stator winding, which is too distant from the cooling liquid. A method has been developed to improve the internal cooling of a PM motor with a high current density by inserting a direct winding heat exchanger between two concentrated windings [70]. Although the cooling channel contacts the stator windings directly, it is hard to transfer heat from the hot spot because of the enamel insulation coating the conductors. Inserting cooling channel inside Litz wires was proposed in [71] to achieve better cooling performance in an axial flux PM machine. However, it has eight cooling tubes per slot, which is only suitable for machines with large slots.

2.8.3 Hybrid cooling

Usually, the motor can operate reliably under overload conditions while applying a single cooling method. However, the high current and power density machine cannot adequately use a single cooling technique. As a result, hybrid cooling, combined forced air, and liquid cooling are becoming more common for traction motors in electric vehicles because of their effectiveness [72].

2.9 Conclusion

In the previous sections, a literature review is presented regarding the definition of MEA, its layout development, and applications introduced over the past decades. This chapter

also includes an overview of various electric helicopter layouts and development. The concept, needs, and challenges of the helicopter ETR system are discussed. Finally, according to the requirements of the helicopter ETR system, a fault-tolerant system, which increases system reliability, and thermal management, which provides a better operating environment, are introduced.

Chapter 3 Electrical machine design

3.1 Introduction

This chapter describes the technical aspects of the electrical machine, including a comparison of machine topologies and materials and the performance qualification of the benchmark. The electrical machine is a central component of the helicopter ETR drive system. The performance and mass of the electrical machine are vital to understand as they significantly affect the drive system's performance. The important factors that should be considered while studying the electrical machine are output power and torque, power and torque density, efficiency, reliability, fault tolerance and thermal management.

Some electrical machine topologies are first introduced to understand the benefits and drawbacks of the various architectures. The goal is to obtain an optimal solution by balancing the advantages and disadvantages of each structure. Then, the lamination materials and PM are discussed, followed by the proposed benchmark design of the electrical machine. Finally, according to the key factors affecting performance, the benchmark design is optimised to improve machine performance.

3.2 Electrical machine topology

Many electrical machine topologies can be chosen for the application. However, for the safe and reliable application of motor design in helicopter ETR drive systems, the following key criteria need to be achieved [16], [43], [48]–[52]:

- *High power and torque density* are needed since the physical volume is limited by the aircraft structure. In addition, the fuel requirement and operating costs are affected.
- *High efficiency* is necessary to minimise fuel consumption, emissions and operating costs.
- *High fault tolerance* allows for the mechanical, electrical, magnetic and thermal isolation between lanes and an increased phase inductance to limit short circuit currents (for PM motors). Meanwhile, the motor needs to be able to operate under fault conditions, which will significantly affect system safety and reliability.

Brush and commutator-based electrical machines are not considered because of their high maintenance needs, low torque density and poor reliability. Therefore, the remaining suitable options are induction, reluctance and PM motors.

Induction machines (IMs) are the most common form of asynchronous machine. They operate by inputting current to stator windings and generating a magnetic field to induce a current in the rotor, usually a squirrel cage. The rotation of the rotor is slower than the rotating magnetic field when it is used as a motor and faster than the stator rotating magnetic field when it is a generator, as the current induction in the rotor requires this relative motion. This difference in speed is termed the slip speed.

IMs are widely used in industrial applications, owing to their simplicity, cost-effectiveness, robustness and reliability. However, they are not highly efficient, requiring thermal management on the rotor due to conduction losses.

Reluctance machines harness the tendency for the magnetic flux to follow the path of the lowest magnetic reluctance to generate torque. The switched reluctance machine (SRM) is the most common type of reluctance machine. In an SRM, the current is input to the stator windings to generate a magnetic flux that travels through the air gap to the rotor without any PMs or coils. The magnetic reluctance of the rotor creates a torque that attempts to align the rotor pole with the nearest stator pole to form a magnetic circuit with minimum magnetic reluctance. The coils are energised in sequence to achieve a constant torque output.

The advantages of the SRM include its rigid structure, high reliability and robustness, fast dynamic response and low manufacturing cost [99], [100]. At the same time, the torque ripple and acoustic noise tend to be high and may need to be minimised when applying the SRM.

PM machines are typically characterised by high power density, efficiency, torque density and reliability. They can have either distributed stator windings like IMs or concentrated windings like switched reluctance motors, with PMs on the rotor. The stator windings generate a rotating magnetic field which interacts with that created by PMs on the rotor to produce a torque on the rotor. Generally, two PM arrangements on the rotor are available: surface-mounted and interior. Surface-mounted PM motors, which are easy to manufacture, are usually used for low-speed applications because of the risk of

disengagement during high-speed operation. In contrast, interior PM motors are suited for high-speed operation, having higher overload capability than surface-mounted PM [102], [103]. Table 3-1 shows the properties of surface-mounted and interior PM motors.

Table 3-1: Comparison of surface-mounted PM motor and interior PM motor [101]

PM Motor type	Surface-mounted	Interior
Pole type	Saliency	Non-saliency
Operation	Direct and quadrature axis inductance are nearly equal	Variation in direct and quadrature axis inductance
Effective Air gap size	Large	Small

3.3 Benchmark design

A performance comparison of three electrical machine topologies based on the review is given in Table 3-2. According to the comparison, the PM motor is the most suitable machine, having a high power-to-weight ratio [104].

Table 3-2: Performance comparison of different electrical machine topologies

Machine topologies	Induction	Switched reluctance	PM
Power density	Low	Medium	High
Efficiency	Low	Medium	High
Cost	Low	Low	High
Fault tolerance	Low	High	High
Robustness	Good	Good	Poor
Air gap	Small, a fraction of mm	Small, a fraction of mm	1 mm or more
Torque ripple	Less than 5%	15%-25%	Up to 10%
Acoustic noise (dB(A))	Below 60	70 to 82	Below 65
Power electronics converter	Not necessary for constant speed motor	Necessary	Necessary
Notes	Low complexity	Tolerate high temperature	Temperature limited by PMs

Because of the fault-tolerance requirement, the multichannel three-phase approach is adopted. In this configuration, each set of three-phase windings has independent power converters, which satisfy the safety critical availability target. Also, the concentrated winding is considered a more suitable choice, achieving electrical, magnetic and thermal insulation between phases. Moreover, the volume of copper in the end windings can be

significantly reduced with concentrated winding, resulting in less motor mass and winding losses.

The combination of the number of slots and poles should be selected carefully to prevent a lower winding factor and minimise losses and torque ripple.

Finally, to achieve higher flux density in the main magnetic circuit and appropriate excitation magnetomotive force, the tooth tips and thicknesses of the rotor and stator core backs need to be considered discreetly.

3.3.1 Materials

Magnetic materials are broadly divided into two categories: soft and hard. The hysteresis loop shown in Figure 3-1 is used to distinguish them because of their different applications [105]–[107].

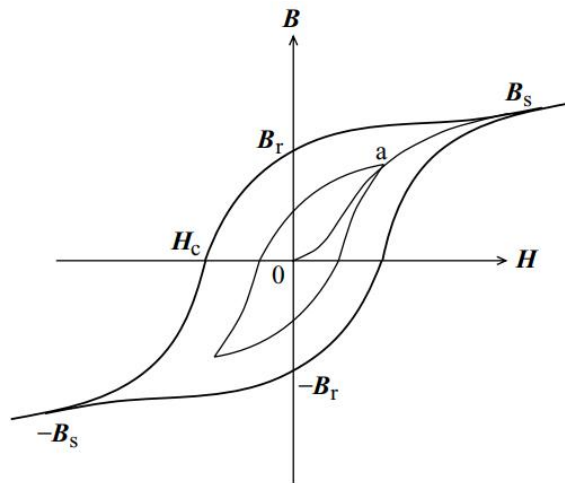


Figure 3-1: Hysteresis loop for a ferromagnet or ferrimagnet [107]

According to Figure 3-1, some concepts that affect the performance of magnetic materials are defined below:

- The saturation magnetic induction strength B_s is the maximum magnetisation that this material can achieve when an external magnetic field is applied.
- The residual flux density B_r , also known as remanence, is the value of the flux density B remaining when the external magnetic field decreases from the highest value of saturation magnetisation to zero.
- The coercivity H_c is the strength of the reversed magnetic field required to reduce the magnet flux to zero.

- The maximum energy product $(BH)_{max}$ is a measure of the maximum magnetic energy stored in a magnet. It is the maximum product of the flux density B and field strength H in the second quadrant of the hysteresis loop for this material.
- The permeability μ is the ratio of the flux density B to field strength H .
- The Curie temperature is the highest temperature at which magnetic materials change their magnetic properties.

Because of their differences in coercivity, soft and hard magnets are classified as shown in Figure 3-2. A hard magnet needs a large magnetic field to saturate the magnetisation and reduce the remanence to zero. Conversely, a soft magnet is easily saturated and demagnetised. Demagnetisation is achieved by means of an alternating magnetic field which brings the uniformly arranged elementary magnets into a uniformly disordered state. The demagnetising power that must be applied for this is determined by the strength of the magnetic field. This depends on the current, coil opening, coil length and number of coils.

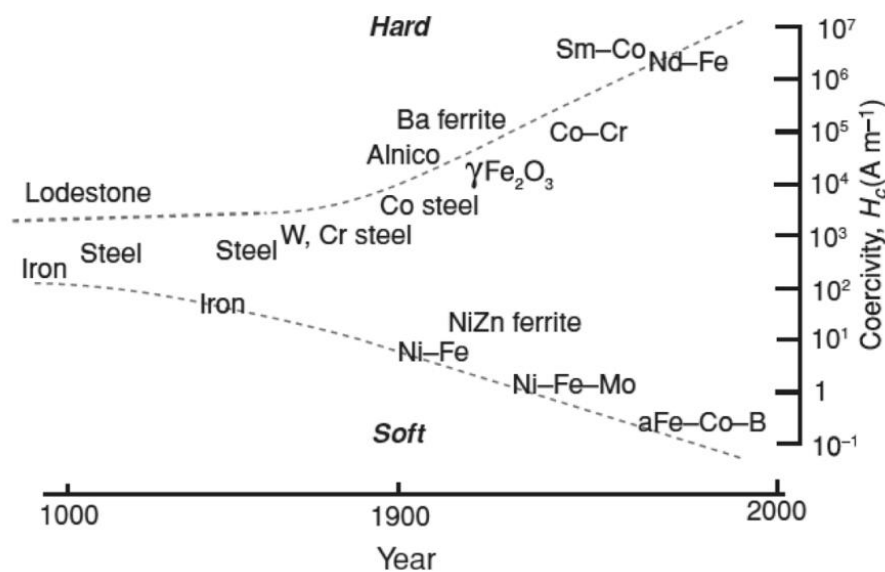


Figure 3-2: Development of coercivity in the 20th century, showing the upper and lower extremes [106]

Soft magnetic materials have magnetic permeability, electromagnetic energy conversion and transmission as their main functions. Therefore, such materials require high magnetic permeability and magnetic induction strength, while the area of the hysteresis lines or magnetic losses should be small. At the same time, smaller values of residual flux density

B_r and coercivity H_c are required, as well as higher saturation magnetic induction strengths B_s .

Hard magnetic materials, such as PMs, maintain constant magnetism once magnetised. They are characterised by high coercivity and high remanence. In practice, PMs work in the second quadrant of the demagnetised part of the hysteresis loop after saturation as shown in Figure 3-1. The improvement of the magnetic energy product of PM materials over most of the 20th century is illustrated in Figure 3-3.

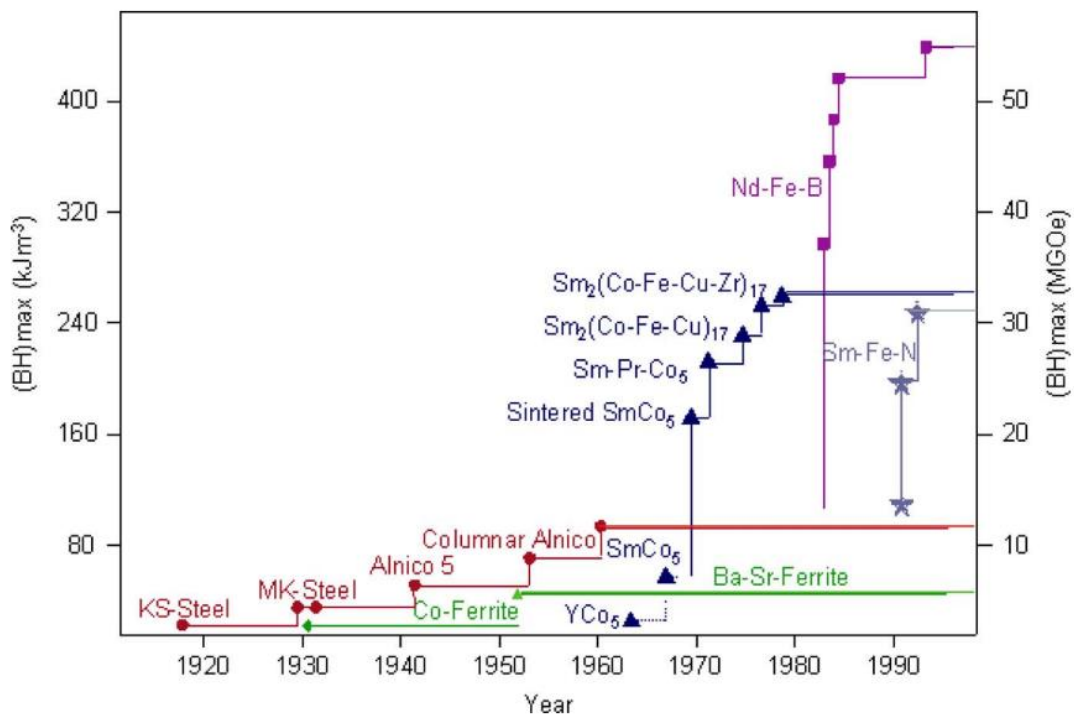


Figure 3-3: Magnetic energy product of PM materials [105]

The common PM materials categories are introduced below [105], [106], [108]–[111]:

- *AlNiCo* is composed primarily of aluminium (Al), nickel (Ni) and cobalt (Co) with a high remanence of around 1.2 T, low coercivity and a very high Curie temperature of about 890°C. As one of the most stable magnets, it is produced by casting and sintered processes.
- *Hard ferrite* is produced by heating a mixture of large proportions of iron oxide and other metallic materials, such as strontium, barium, manganese, nickel and zinc. It has a low residual flux density of 0.46 T, high coercivity and a low

temperature coefficient. Hard ferrite is widely used because of its simple manufacturing process and low cost.

- *Rare earth PM* is a strong PM made from alloys of rare earth elements. It is characterised by a very high coercivity and a high residual flux density. However, it costs more than other types of PM. The two types of rare earth PM are samarium-cobalt (SmCo) and neodymium-iron-boron (NdFeB). SmCo PM has a high residual flux density of 1.15 T and a high Curie temperature of 800°C, which lead to a maximum operating temperature of around 300°C. Compared with SmCo PM, the NdFeB PM can provide a higher residual flux density of 1.4 T. However, it has a lower Curie temperature of 400°C and needs to operate under 170°C, which is roughly half that of SmCo PM.

The NdFeB PM is selected because of the higher maximum energy product, which can reduce the machine weight and meet the requirement of the designed motor for the helicopter ETR drive system.

Vacoflux 48, chosen for the rotor and stator lamination, is made of cobalt iron alloys, which have a maximum saturation at 2.35 T. Figure 3-4 shows the relationship between magnetic flux density and magnetic field strength of this lamination.

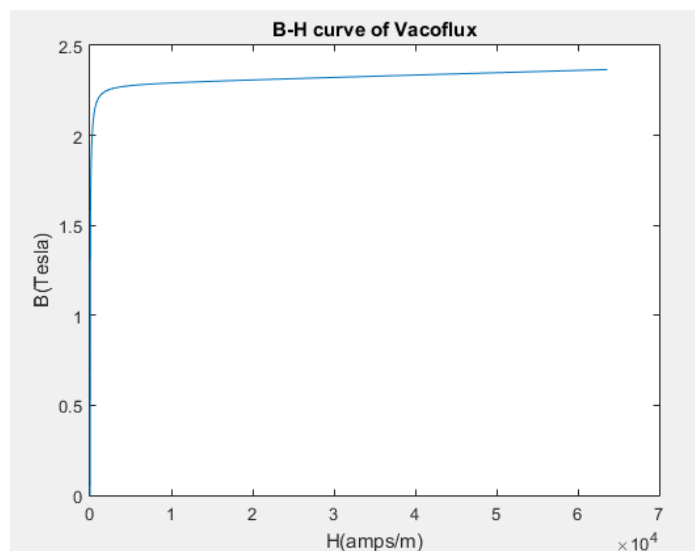


Figure 3-4: B–H curve of Vacoflux 48

3.3.2 Finite element analysis and Simcenter MagNet software

Finite element analysis (FEA) is a popular method for simulating a physical system by applying a numerical solution to differential equations that have emerged in engineering

modelling. It subdivides a complex system into smaller, simpler units, called elements, and the finite number of units form an algebraic system of equations. The method approximates these simple functions of finite elements over the domain, which are then combined into a global system of equations that models the entire problem for the final calculation [113]. FEA can accurately represent the complex geometries and the total solutions, as well as capture local effects. Although this is achieved by a particular space discretisation, the actual continuous domain is represented when recombining all sets of elements. The use of the software is paramount as FEA usually involves many calculations, and Simcenter MagNet is one such software that uses FEA to solve electromagnetic problems.

Simcenter MagNet is powerful electromagnetic simulation software that allows the performance prediction of motors, generators or any components with PMs or coils [112]. Complex electromagnetic devices can be accurately designed, optimised and analysed with this software. In addition, Simcenter MagNet can solve problems by simulating static magnetic fields or transient fields including motion with six degrees of freedom (X, Y, Z, roll, pitch and yaw). Meanwhile, options for 2D and 3D modelling are available to solve electromagnetic problems. However, while 2D simulation results can be gained quickly, 3D simulation results are more accurate at the cost of a long computation time, requiring a trade-off. Both 2D and 3D modelling are considered to analyse and optimise the designed PM motor.

3.3.3 Motor requirements and preliminary design

The motor performance requirements from project are listed in Table 3-3.

Table 3-3: Motor Requirements

Output Power	65 kW
Output Speed	2043 rpm
Torque	305 Nm
Current Density	$\geq 10 \text{ A/mm}^2$

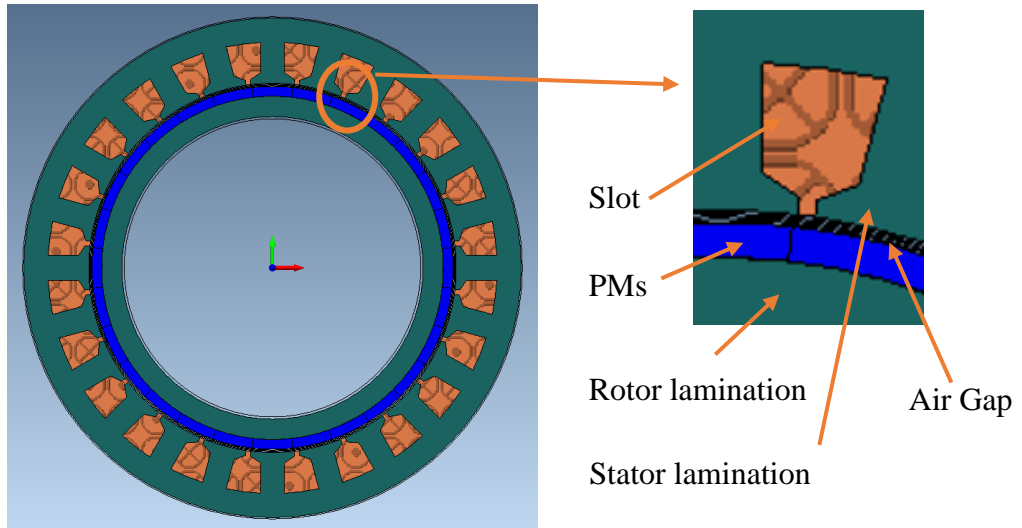


Figure 3-5: Cross-section of the PM motor

Table 3-4: Preliminary motor parameters

Number of poles	28
Number of stator slots	24
Stator outer diameter	308 mm
Stator inner diameter	228 mm
Rotor outer diameter	224 mm
Rotor inner diameter	186 mm
Stack length	80 mm
Airgap	2 mm
PM thickness	5.5 mm
Number of turns per phase	15
Wire diameter	1.78 mm

Table 3-5: Performance of the preliminary design

Phase Current	145.2 A _{max}
Average Torque	303.4 Nm
Speed	2043 rpm
Output power	64.91 kW
Total losses	4113 W
Efficiency	94.04%
Motor weight	35.88 kg
Power density	1.81 kW/kg
Current density	10.27 A/mm ²

All of these performance factors contribute to a preliminary motor design, the cross-section of which is shown in Figure 3-5. Table 3-4 lists the main parameters of the motor, and Table 3-5 presents the simulated performance of the preliminary design in healthy-mode conditions. The 24-slot, 28-pole combination was chosen because of its high winding factor and its low cogging torque.

3.4 Geometry optimisation

Comparing the performance of the designed motor with the requirements, power density is considered the key factor in optimising the motor. To achieve the expected power density, the motor weight needs to be reduced by adjusting the dimensions of the motor, such as the thicknesses of the rotor and stator yokes and the width of the stator tooth. Additionally, the saturation in the lamination should be limited since it can reduce torque capability and increase iron loss. During this stage, 2D FEA simulation will be adopted to saving the time.

Figure 3-6 shows the magnetisation curve and corresponding permeability for ferromagnets. At low field strength H , the permeability increases with magnetisation. However, the permeability decreases after the magnetisation passes the knee point, and the magnetic flux density just increases a little after the knee point.

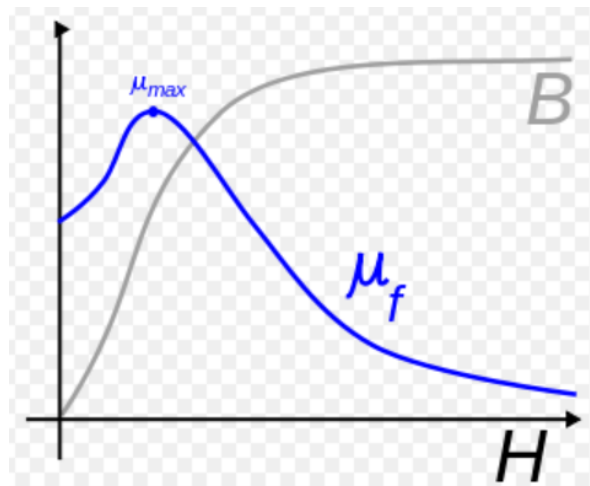


Figure 3-6: Magnetisation curve for ferromagnets and corresponding permeability

[115]

3.4.1 Ratio of rotor yoke thickness to PM pitch

In the preliminary design, because the thickness of the rotor yoke has an influence on the saturation in the rotor yoke, which is affected by the size of the PM, the ratio of the rotor yoke thickness to PM pitch should be optimised. Figure 3-7 shows the trends of the power density and maximum saturation in the rotor yoke when changing this ratio. During this optimization, keep fixed the air-gap length and pole pitch. Considering the corresponding permeability, the working area should be set near the knee point. Therefore, the optimal ratio is 0.395 when considering Figures 3-4 and 3-6 to achieve higher power density. As

the ratio of the rotor yoke thickness to PM pitch decreases, the permeability increases which cause saturation in the rotor yoke increases. Then, while the ratio of the rotor yoke thickness to PM pitch continuous reduce, the permeability increases to the knee point and the saturation in the rotor yoke almost achieve the maximum value. After the permeability pass the knee point, when the thickness of the rotor yoke keep reducing, the rotor lamination will oversaturation which would cause overheat and affect motor performance.

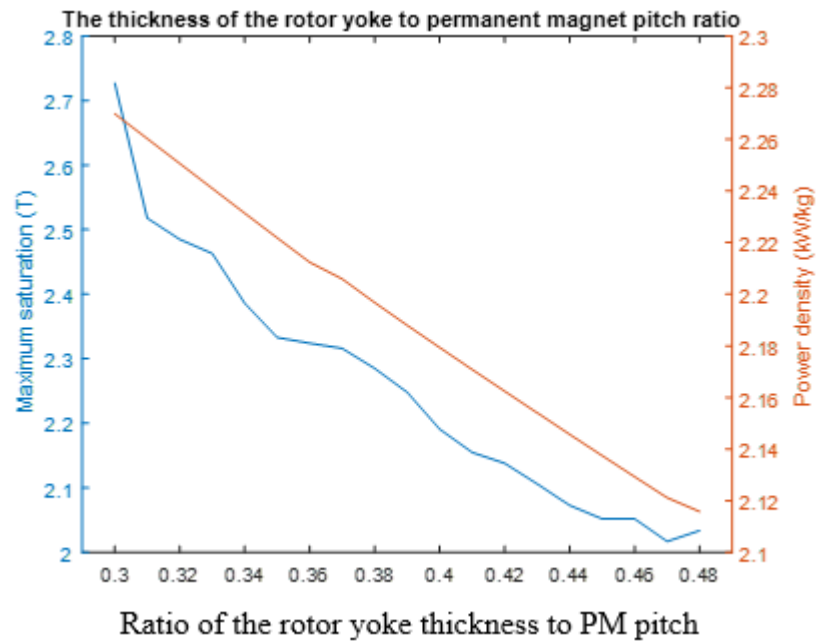


Figure 3-7: Optimisation of the ratio of rotor yoke thickness to PM pitch

3.4.2 Ratio of the stator yoke thickness to PM pitch

Because the same material is used for the stator lamination, optimisation of the stator yoke thickness is also considered. Figure 3-8 shows the trend of power density and maximum saturation in the stator yoke when changing the stator yoke thickness. As a result, the optimal ratio is 0.39.

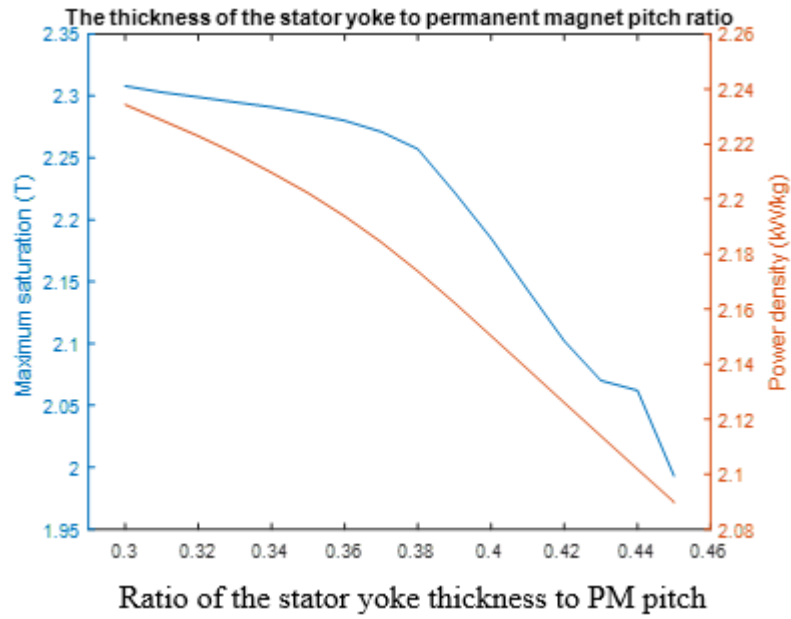


Figure 3-8: Optimisation of the ratio of stator yoke thickness to PM pitch

3.4.3 Ratio of tooth pitch to PM pitch

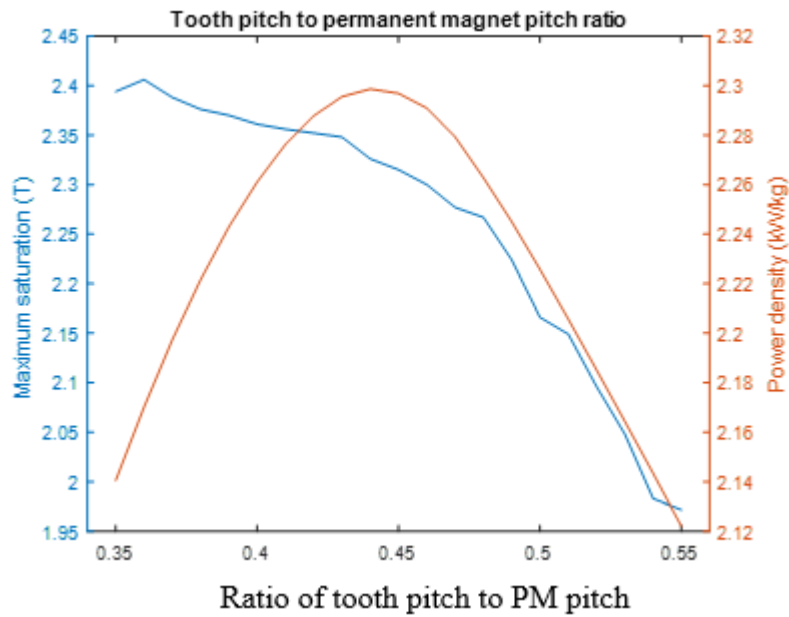


Figure 3-9: Tooth pitch to permanent magnet pitch ratio

The tooth pitch to PM pitch ratio is also critical for machine optimisation, and the power density maximises in the ratio range of 0.43 to 0.46, as shown in Figure 3-9. Since this optimisation changes the size of the slot, this requires maintaining the MMF and current density. Considering maximum saturation, 0.46 is selected for this ratio.

The optimised parameters and performance of the motor are listed in Tables 3-6 and 3-7. After geometry optimisation, there is a small increase in the performance of the motor, e.g. the output power is increased and the weight of the motor is reduced.

Table 3-6: Optimal motor parameters

	Original model	Optimised motor
Number of poles	28	28
Number of stator slots	24	24
Stator outer diameter	308 mm	300 mm
Stator inner diameter	228 mm	228 mm
Rotor outer diameter	224 mm	224 mm
Rotor inner diameter	186 mm	193 mm
Stack length	80 mm	87 mm
Airgap	2 mm	2 mm
PM thickness	5.5 mm	5.5 mm
Number of turns per phase	15	17
Wire diameter	1.78 mm	1.78 mm

Table 3-7: Optimised motor performance

	Original model	Optimised motor
Phase Current	145.2 Amax	147.51 Amax
Average Torque	303.4 Nm	306.83 Nm
Speed	2043 rpm	2043 rpm
Output power	64.91 kW	65.64 kW
Total losses	4113 W	4124 W
Efficiency	94.04%	94.09 %
Motor weight	35.88 kg	29.03 kg
Power density	1.81 kW/kg	2.26 kW/kg
Current density	10.27 A/mm ²	10.43 A/mm ²

3.5 Optimisation of power density with constant output

Power density, the most important parameter for the PM machine, is optimised in this section. The 24 slot, 28 pole design is essentially a multiple of a 12 slot, 14 pole machine. This gives a high winding factor and, by having more poles than slots, the tooth width can be reduced, leaving more room for the windings.

The motor weight is related to the motor size, i.e. the outer diameters (ODs), inner diameters (IDs) and length of the machine. According to the Formula (3-1) [116], the basic rule for optimisation is to keep the poles–slots ratio and increase the rotor ID. While increasing the ID of the stator, the length of the stator should be changed according to the Formula (3-1) to ensure that the value of the output torque is the same. As a result, the

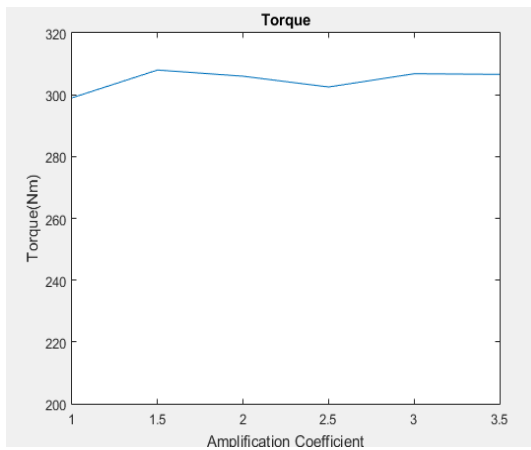
numbers of poles and slots change. In addition, to maintain the output power, the motor length is reduced. Table 3-8 lists the motor dimensions and the numbers of poles and slots. The amplification coefficient is the required multiple of the rotor ID. Figure 3-10 presents the trends of the performance of the optimized motor which according to the formula by MagNet 2D simulation. Furthermore, in this optimisation it is assumed that the input current is perfectly sinusoidal and the end windings are ignored, and that there are no other measures, such as magnet segmentation.

$$T = kD^2L \quad (3 - 1)$$

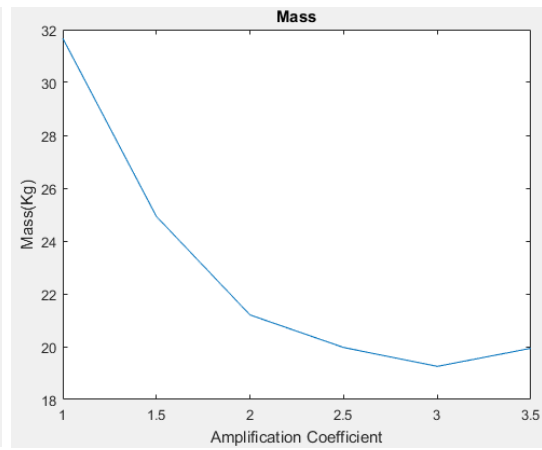
where T is torque, k is a constant, D is the rotor diameter, L and is the axial rotor length.

Table 3-8: Motor dimensions as functions of the amplification coefficient

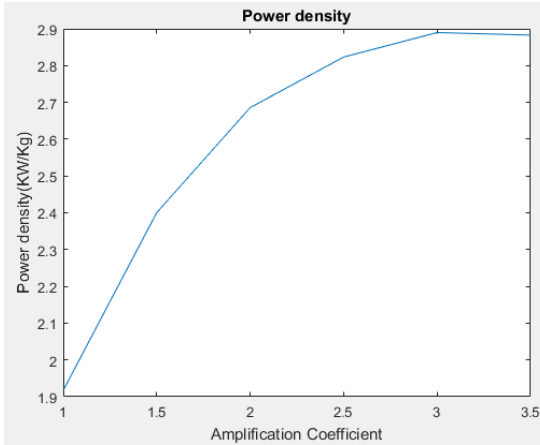
Amplification coefficient	Stator OD (mm)	Stator ID (mm)	Rotor OD (mm)	Rotor ID (mm)	Length (mm)	No. of poles	No of slots
1	300	228	224	193	87	28	24
1.5	395	324	320	290	47	42	36
2	491	421	417	386	29	56	48
2.5	588	518	514	483	20	70	60
3	684	614	610	579	15	84	72
3.5	780	710	706	676	11.8	98	84



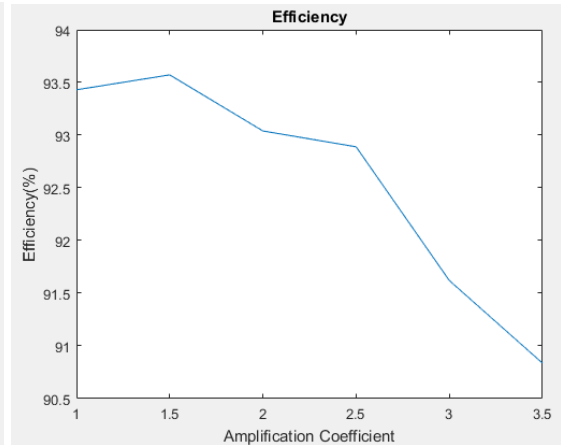
(a)



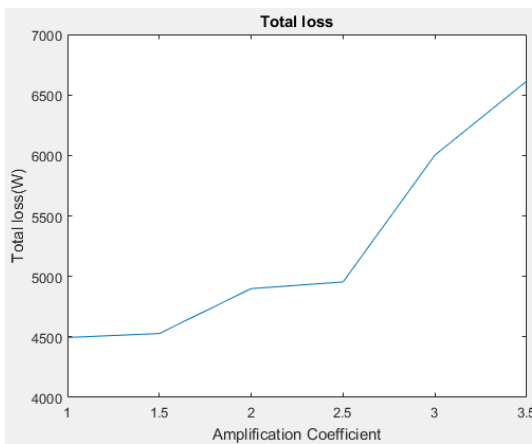
(b)



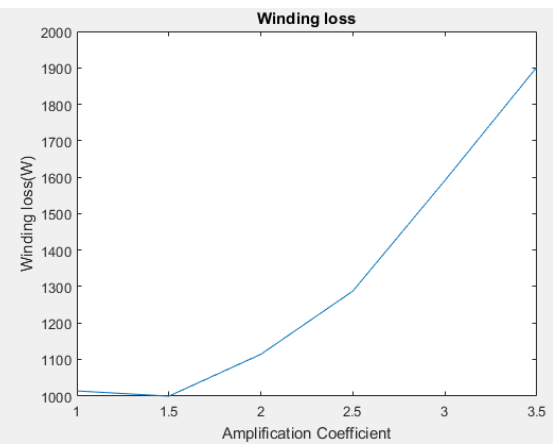
(c)



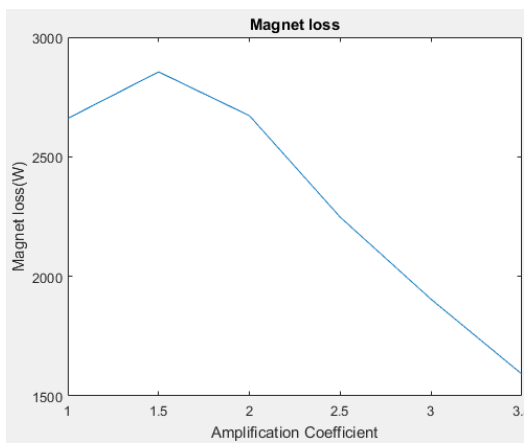
(d)



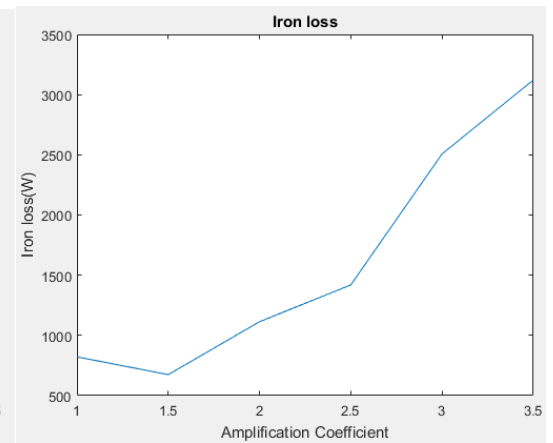
(e)



(f)



(g)



(h)

Figure 3-10: Motor performance trends

Figure 3-10 (a) shows the torque hovering around 305 Nm, indicating these motor designs have the same output power. The motor mass curve shown in Figure 3-10 (b) is as

expected while ignore the mass of end winding, decreasing as the motor size increases until the motor diameter is three times as large as that of the original motor. The machine mass minimises at an amplification coefficient of three. Because the motor designs have the same output power, the power density, Figure 3-10 (c) shows the opposite trend as the motor mass. Power density reaches the highest value when the amplification coefficient is three and then decreases with the rise of the amplification coefficient.

The motor efficiency shown in Figure 3-10 (d) declines with the increase in the amplification coefficient because the motor's total loss increases continuously, as described in Figure 3-10 (e). As illustrated in Figure 3-10 (f), at low amplification coefficients, the winding loss decreases slightly because of the reduction in the length of the motor. However, it surges after doubling the rotor ID because of the increasing number of stator slots that results in the longer end winding. In other words, the increase in the length of the end winding is much more than the decrease in the length of winding in the slots.

The eddy current loss in PMs is associated with PM volume and frequency. Moreover, the motor length decreases continuously, reducing the PM volume. Therefore, the magnet loss declines as the diameters increase, as shown in Figure 3-10 (g).

Figure 3-10 (h) presents the trend of the iron loss, which increases from around 900 W to more than 3000 W from the high frequency.

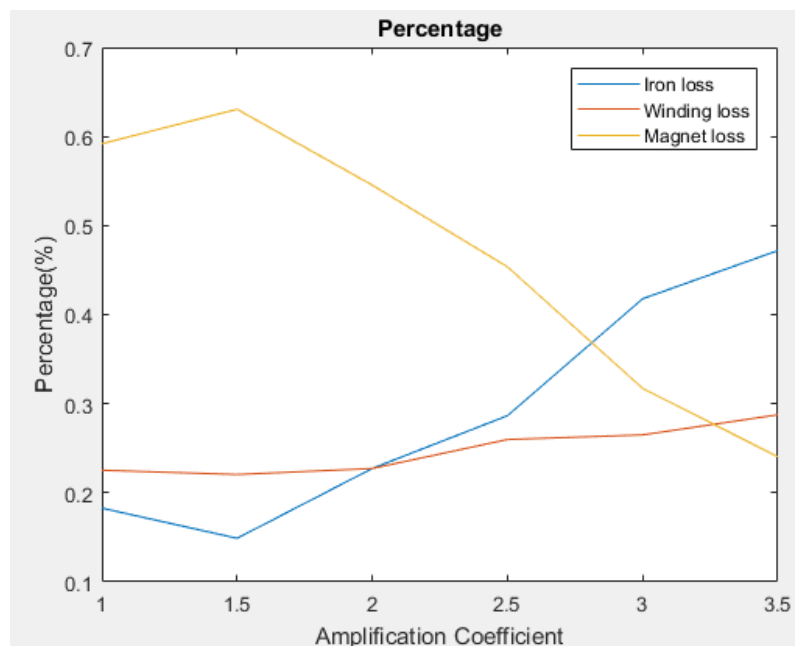


Figure 3-11: Percentages of the different types of losses

Figure 3-11 shows the percentages of different types of losses in these scenarios. At low amplification coefficients, the magnet loss accounts for around 60%, while the winding and iron losses each occupy 20%. Along with the increase of motor diameter, the winding and iron losses increase continuously as the magnet loss declines. Finally, the iron loss occupies around 48% of the total loss, while the winding loss and magnet loss account for 28% and 24%, respectively.

In summary, although the power density is maximum when the motor diameter is three times that of the original motor, the losses are also high, decreasing efficiency. Therefore, the trade-offs between power density and efficiency should be considered. As a result, the optimal amplification coefficient of the motor is two. The power density does not change significantly with an amplification coefficient range of 2–3.5. In addition, the winding and iron losses remain lower when the motor diameter is doubled.

3.6 Conclusion

In this chapter, a literature review of the electrical machine topologies is provided. Then, a comparison of different motor topologies leads to a suitable motor architecture, the PM motor. Afterwards, an overview of the different magnetic materials is provided. A preliminary design of the motor is based on the requirements of the machine. Finally, the geometric parameters of the motor are optimised to achieve a higher power density.

Chapter 4 Loss analysis

4.1 Introduction

More electric aircraft, compared with conventional systems, offer higher power density and efficiency, the reduction of emissions and noise, and lower operational and maintenance costs. However, even at high efficiency the loss density in the machine is high: care is needed to ensure that the losses are kept to a minimum. As a result, the losses of the machine which include winding loss, magnet loss and iron loss should be studied in detail. It is also important to mention that the total motor losses also include wind resistance, mechanical losses such as bearing losses, etc.

In this chapter, the losses of the motor have been calculated in a more comprehensive manner. Firstly, the winding loss, including DC loss and AC loss has been calculated by 2D FEA. A method to reduce the total winding loss in the stator windings has been described as well. Then, the PM losses are considered, with particular focus on harmonic effects and several methods that try to reduce this effect are proposed.

4.2 Winding loss

The winding has an additional copper loss because of eddy currents which result from the alternating magnetic field [117]. The eddy current loss consists of skin effect and proximity effect [118]. The skin effect is the high-frequency AC current flow on the surface of the conductor. The proximity effect is caused by the alternating magnetic field generated from the adjacent conductors while the AC current flows in these conductors. As a result, the total total winding loss can be calculated as

$$P_{Tot} = P_{DC} + P_{sk} + P_{pr} \quad (4.1)$$

where P_{Tot} is the total winding loss, P_{DC} is the DC loss, P_{sk} is the loss caused by the skin effect, and P_{pr} is the loss caused by the proximity effect.

In order to accurately calculate the total winding loss in stator windings, the winding part of the CAD model should be improved, as shown in Figure 4-1. In this model, the insulation of the wire is neglected and only the coil in the slot is considered in the calculation of DC losses.

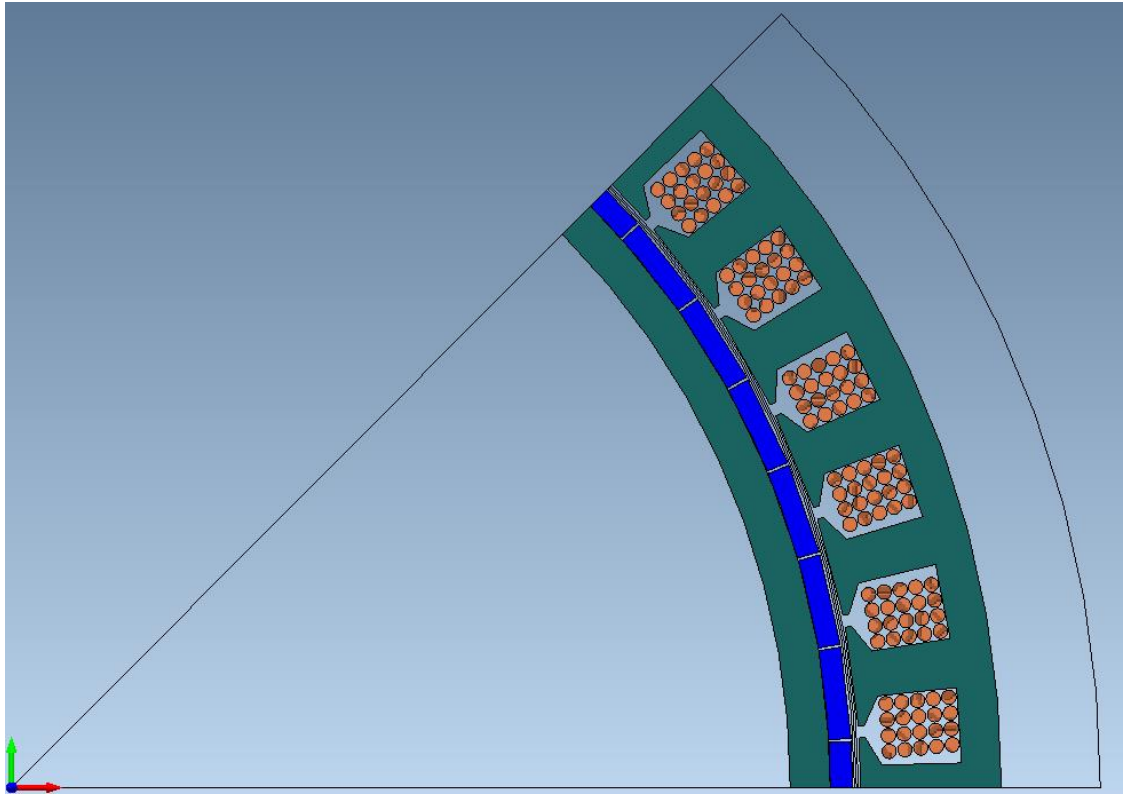


Figure 4-1: The CAD model of the motor with 20 conductors

Figure 4-1 shows one-eighth of the whole model which replaces the block winding in the slot area with 20 individual conductors which fit the required current density and output torque. The winding loss is described in Table 4-1.

Table 4-1: Winding loss (20 conductors per slot)

DC Loss (W)	534
AC Loss (W)	3930

From Table 4-1, the results show AC loss is nearly eight times the DC loss, which means the loss caused by the skin effect and the proximity effect occupy around 85% of the total losses. It is important to study the methods that could reduce AC loss by weakening the skin effect and the proximity effect. Different sizes of conductors have been chosen to compare the winding losses. Figure 4-2 shows the model which changes the diameter and number of conductors. In order to simplify the model, only one phase is changed, with results extrapolated to include the whole machine.

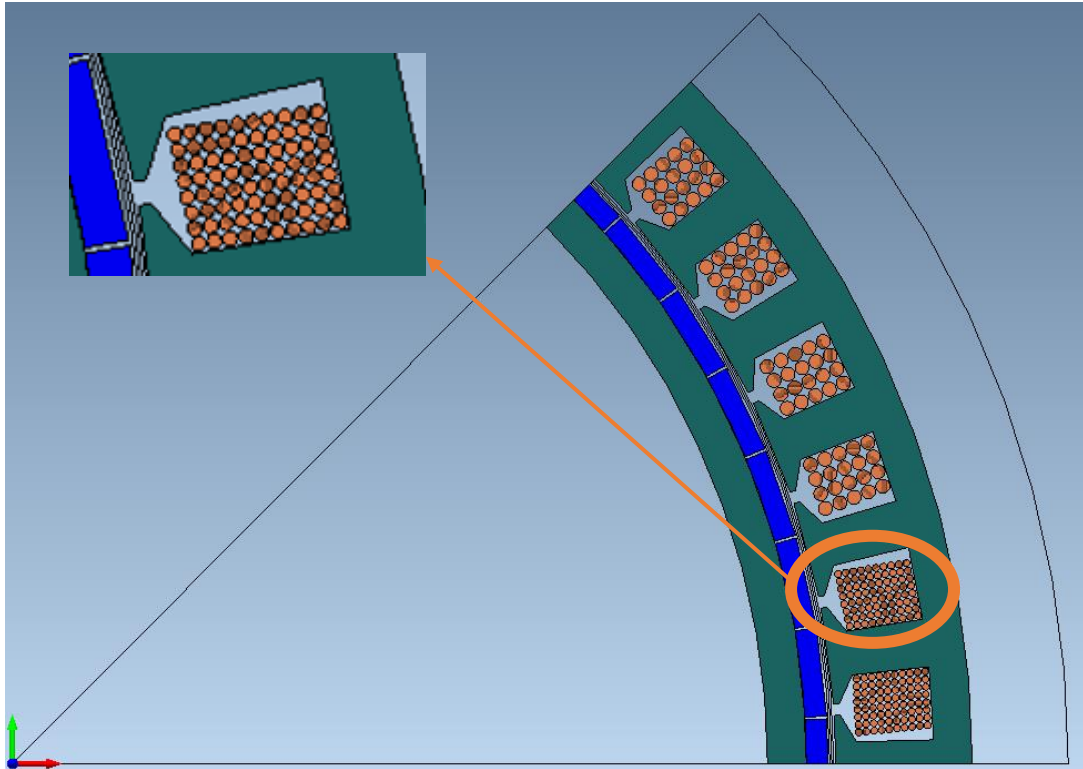


Figure 4-2: The CAD model of the motor with 80 conductors

In this model, the radius of the conductors in the first phase reduces by 50% compared with other phases, which means the area of the conductor is a quarter of the conductor in Figure 4-1. As a result, to keep the same output power, the number of conductors increases to 80, which is four times greater than before. The result is shown in Table 4-2.

Table 4-2: Winding loss (80 conductors per slot)

DC Loss (W)	534
AC Loss (W)	1550

Compared with Table 4-1, although the DC loss of these two models is the same, the losses because of the skin effect and the proximity effect decrease to 29% of the model with 20 conductors per slot.

Besides, the frequency of input current would have a great influence on the value of AC loss. Figure 4-3 and Figure 4-4 show the winding loss while changing the frequency from 1 Hz to 1000 Hz for the model with 20 conductors and 80 conductors respectively. From these two figures, it could be found that the AC loss of the winding will increase continuously through the increase of the frequency regardless of the number of conductors per slot.

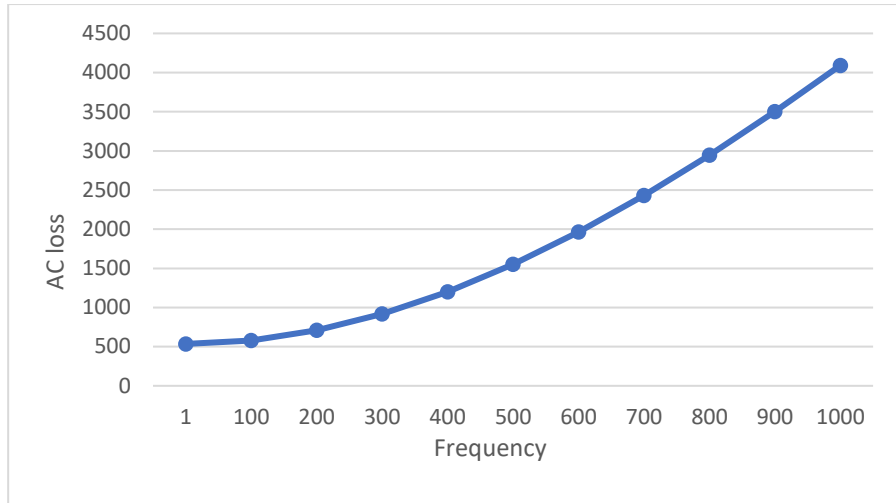


Figure 4-3: AC loss from 1Hz to 1000Hz (20 conductors per slot)

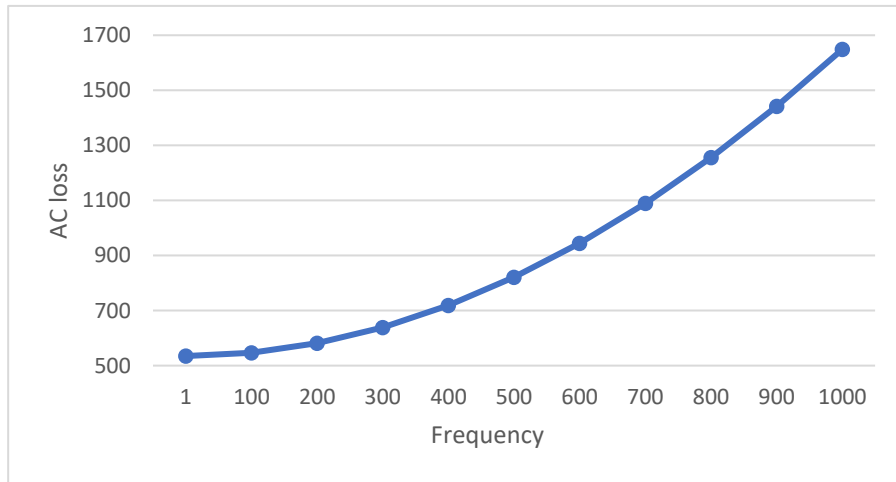


Figure 4-4: AC loss from 1Hz to 1000Hz (80 conductors per slot)

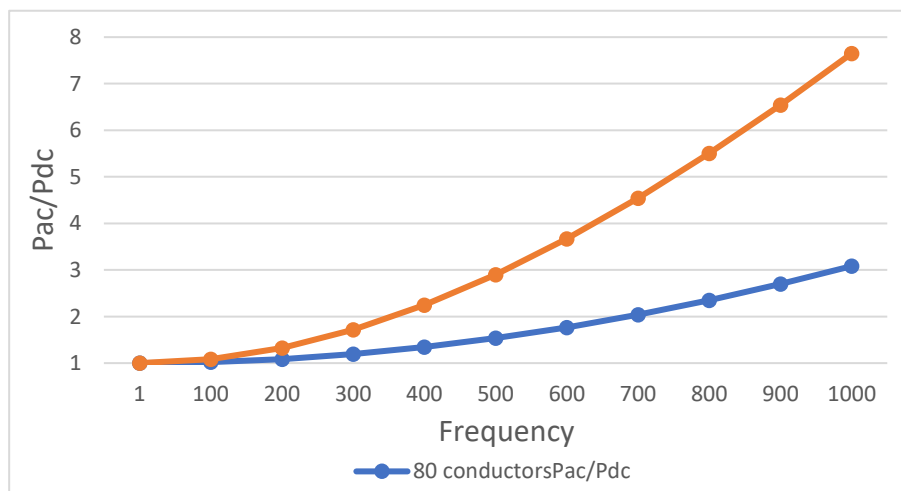


Figure 4-5: The trend of AC loss/DC loss from 1 Hz to 1000Hz

Figure 4-5 shows the trend of AC loss/DC loss from 1 Hz to 1000 Hz which compares the model with 20 conductors per slot and the model with 80 conductors per slot. By comparing these two curves, no matter what the wire sizes, the losses caused by the skin and proximity effects grow significantly while the frequency increases. In summary, for the machine with high-frequency input current, it is necessary to reduce AC loss by using multiple strands of thinner wire for the winding.

4.3 PM loss

Because the permanent magnets are exposed to the air gap in surface-mounted PM motors, there is a large number of harmonics which include spatial harmonics created by the concentrated winding and time harmonics due to current ripple, which lead to eddy current loss in the PMs. This loss can result in a high temperature in the PMs, which will decrease the performance of the motor, increase the risk of demagnetization of the PMs and could cause the failure of the sleeve which used to hold the PMs. As a result, it is necessary to study the eddy current loss in PMs [119], [120].

There are many methods to reduce the rotor eddy current loss in PMs caused by spatial harmonic, such as segmenting the PM in axial, circumferential and radial directions. In [121], an analytical method has been proposed to assess the influence of circumferential and axial segmentation, which shows that both of these two methods would lead to the reduction of eddy current losses when the skin effect is negligible. Also, the circumferential segmentation of PMs has been considered an efficient method of reduction of the eddy current losses in [122]-[126]. In addition, [127] demonstrated a significant reduction of losses by segmenting the PM in the axial direction. In [128], [129], the effect of the segmentation of the PM has been presented.

Moreover, some papers proposed several methods to reduce the loss by optimizing the geometry model of the PM machine. In [130], the eddy current loss in the PM for both planar and cylindrical arrangements are compared, indicating a deviation of only $\pm 5\%$. A new method has been mentioned in [131] which optimizes the shape of the rotor and stator without significant decreases in the torque. In [132], auxiliary slots with optimized size and position are proposed to reduce the PM eddy current loss. Also, a large air gap has been used in machine design to reduce PM losses in [133]. However, it will also cause a reduction in output torque.

Furthermore, high order time harmonic, which are caused by pulse width modulation from the inverter also will result in eddy current loss in the PMs. The space harmonics of Magnetomotive force (MMF) created by concentrated windings, vary according to the coil pitch and whether there are an integral number of slots per pole pair. However, care is needed to ensure that the selected arrangement does not significantly reduce the fundamental, torque producing, component of MMF [134].

4.3.1 Surface-mounted PM motor VS Interior PM motor

In order to understand the PM losses caused by the harmonic effect, a surface-mounted PM motor that was mentioned in chapter 2 and an Interior PM motor, which replaces surface-mounted PM with V-shape PMs, are compared. Figure 4-6 shows the two radial cross-section models with different rotor topologies. These two motors have same stator geometry, input current and output power and torque.

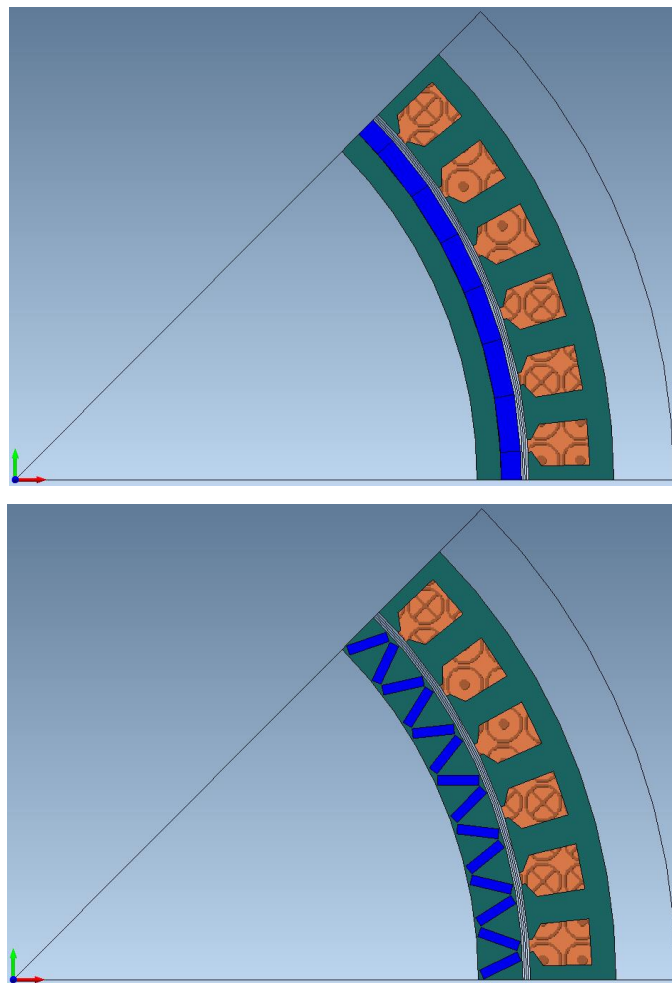


Figure 4-6: (a) Surface-mounted PM motor (b) Interior PM motor

4.3.2 The surface-mounted PM motor

4.3.2.1 Segmentation of surface-mounted PM motor

The idea of segmentation of PMs to reduce the eddy current loss could be found in an analytical model (4-2) [121], usually used to calculate the iron loss in laminated steel, which explains the eddy current loss per unit volume.

$$P_e = \frac{\pi^2 f^2 B_m^2 w^2}{6\rho} \quad (4 - 2)$$

where f is the frequency of the motor input current, B_m is the maximum instantaneous flux density in PMs, w is the width of PM segmentation and ρ is PM resistivity. This equation indicates that the eddy current losses are proportional to the square of the width w . As a result, the losses will decrease when the PMs are divided into small, insulated segments. Note, however, that this model assumes that the eddy currents have no effect upon the magnetic flux, resulting in a resistance value limited situation on PMs. At high frequencies this is not always the case and eddy currents can start to flow in a skin.

The results of 2D simulation by FE analysis illustrate the effect of eddy current losses in PMs by using circumferential segmentation, as shown in Table 4-3. Figure 4-7 shows one magnet divided into four small equal circumferential segments.

Table 4-3: The results of PM losses by FEA simulation

No. of segments	PM loss
1	5493 W
2	1960 W
3	955 W
4	635 W

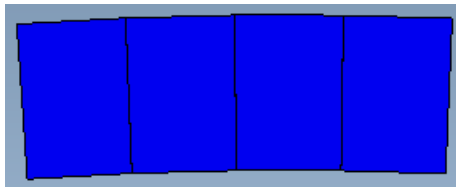


Figure 4-7: Segmentation per PM

Figure 4-8 illustrates the trend of PM losses while using circumferential segmentation. The results show that circumferential segmentation is an effective way to reduce eddy current loss in PMs.

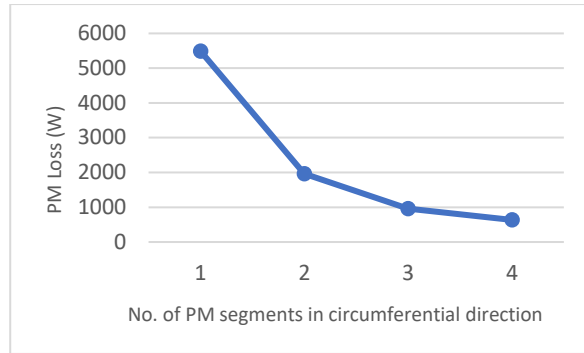


Figure 4-8: The trend of PM losses by circumferential segmentation

Segmenting PMs in the axial direction is another common method used to diminish the loss in PMs. 3D FE analysis has been used to calculate the eddy current loss. Figure 4-9 shows the PMs segment in the axial direction. There is a 0.1 mm gap between each magnet segment in the axial direction in order to become electrically isolated. Table 4-4 shows the value of PM loss and length per PM while the number of segments increases from 2 to 16.

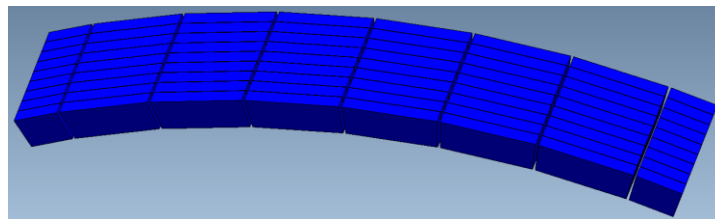


Figure 4-9: Segmentation in the axial direction

Table 4-4: PM length and loss by axial segmentation

No. of segments	Length per PM	PM loss
2	14.45 mm	3345 W
3	9.6 mm	1927 W
4	7.18 mm	1195 W
5	5.72 mm	796 W
6	4.75 mm	538 W
7	4.06 mm	407 W
8	3.54 mm	310 W
9	3.13 mm	244 W
10	2.81 mm	187 W
11	2.55 mm	138 W
12	2.33 mm	105 W
13	2.14 mm	81 W
14	1.98 mm	65 W
15	1.84 mm	54 W
16	1.72 mm	46 W

Compared with the result without segmentation, the total PM losses diminish greatly, especially the number of segments over 11. However, the length of PM less than 2.5 mm which would cause huge cost on manufacturing. Figure 4-10 shows the trend of PM losses while using axial segmentation.

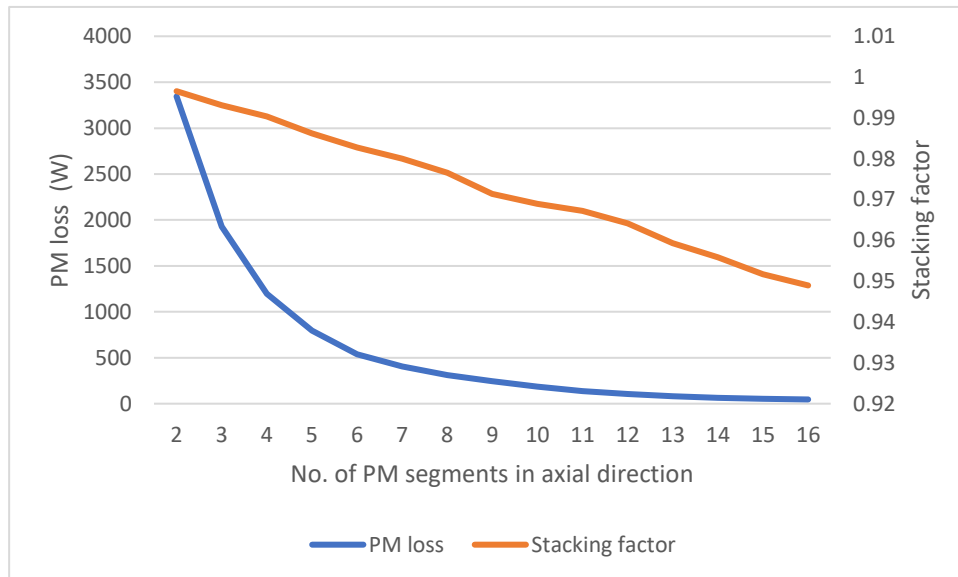


Figure 4-10: The trend of PM losses by axial segmentation

4.3.2.2 Time harmonic effect

Time harmonics caused by pulse width modulation of the inverter also will result in eddy current loss in the PMs. In all work up to this point, the default current source used for simulation is a perfect sinewave, shown by the blue line in Figure 4-11. A separate drive system model has been used to generate more realistic current waveforms, which are then used as sources in the FE model. Two different PWM switching frequencies have been simulated by Matlab. The first one has a 40 kHz switching frequency, giving a total harmonic distortion (THD) of 5.8%, which is shown by a red line in Figure 4-11. The second one has a 100 kHz switching frequency, with a THD of 2.3% and is shown by the yellow line. Such a high switching frequency would require the use of wide band-gap switching devices, such as Silicon Carbide. Table 4-5 shows the simulation result of the model without any segmentation. The model with circumferential segmentation has also been simulated with the different current sources, with the results illustrated in Table 4-6.

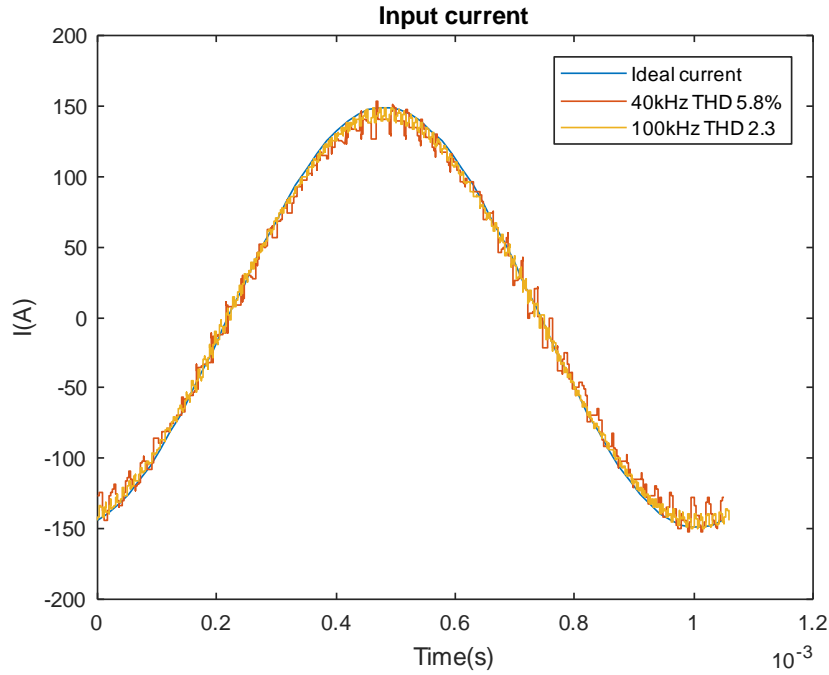


Figure 4-11: Three different types of input current

Table 4-5: Simulation result of the model without segmentation

	Ideal current	40kHz THD 5.8%	100kHz THD 2.3%
Magnet loss (W)	5682	7432 (131%)	6004 (110%)
Iron loss (W)	387	553 (143%)	382 (99%)

Table 4-6: Simulation result of the model with circumferential segmentation (4 segments)

	Ideal current	40kHz THD 5.8%	100kHz THD 2.3%
Magnet loss (W)	635	4878 (768%)	1378 (217%)
Iron loss (W)	387	422 (109%)	386 (99.75%)

The magnet losses vary hugely between the three different input current sources. In Table 4-5, where the magnets are not segmented, the induced loss increases by 36% due to the time harmonics generated by the 40 kHz switching frequency and by 10% with the 100kHz switching frequency. Clearly, in the absence of segmentation the space harmonics are the major contributor to loss.

When segmentation is introduced the losses due to space harmonics drop by almost an order of magnitude, but the segmentation can be seen to increase the losses due to time harmonics. The model with circumferential segmentation has losses due to time harmonics which are seven times higher than due to space harmonics, whilst at 100kHz the time harmonic loss is approximately equal to that caused by the space harmonics.

Figure 4-12 shows the trend of PM loss with increasing circumferential segmentation of the magnets, using the three different current sources. It shows that the segmentation will not reduce losses effectively with a 40 kHz switching frequency. The results with 100 kHz switching frequency have better performance, although the time harmonic induced losses are still significant.

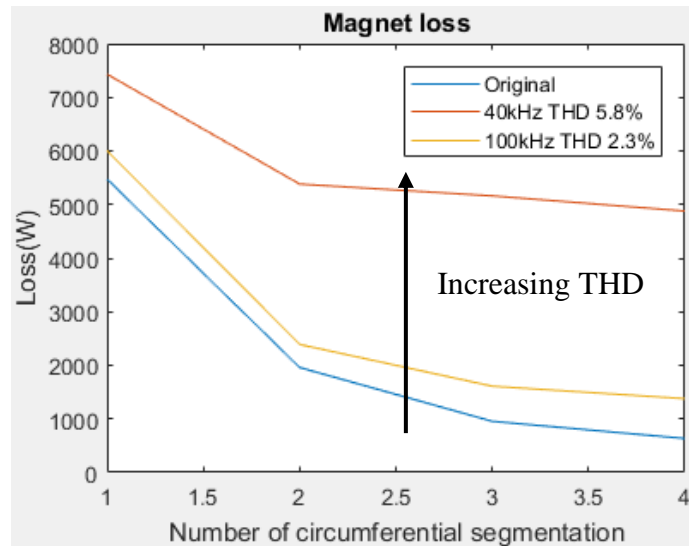


Figure 4-12: The trend of PM losses with three type current sources and circumferential segmentation

In summary, segmentation will reduce the losses due to space harmonics of flux, as displayed when excited with a sinusoidal current. However, time harmonics of current also give rise to significant loss and this loss is not reduced so much by segmentation.

The level of time harmonics can only be very low in order to produce an acceptable rotor loss: it seems that, in this case the switching frequency has to be of the order of 100kHz to achieve this.

4.3.3 Optimization methods

In order to understand the PM losses and then optimize the motor to reduce them, the PM loss distribution with 40kHz time harmonics in the input current is shown in Figure 4-13. According to Figure 4-13, most losses can be found on the surface of the PMs and at the junction between the PMs due to the shallow penetration depth of high-order time harmonics in the PMs. The higher the order of the time harmonics, the shallower the penetration depth. As a result, many high-order time harmonics generate eddy currents only on the surface of PMs to produce eddy currents.

Several methods have been proposed to decrease losses in PMs. For comparison purposes, the same legend is used for all PM loss distributions. The current with a 40kHz switching frequency will be used as the current input for comparison.

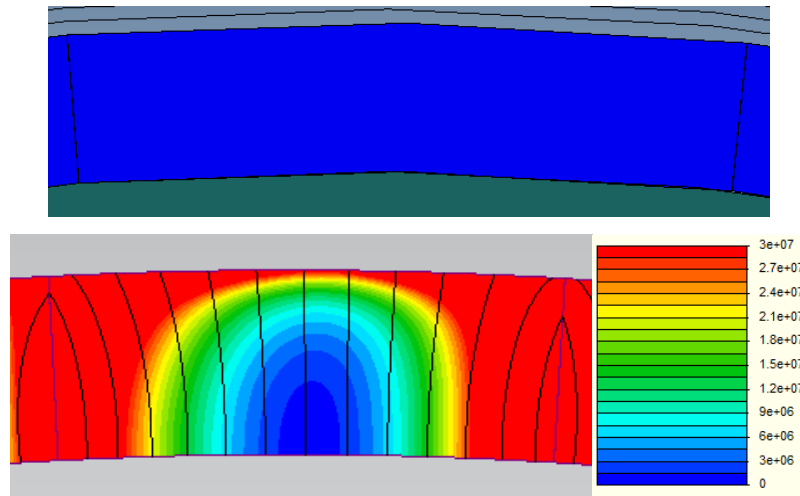


Figure 4-13: The structure of the PM and finite element analysis of PM losses distribution in the presence of a current with additional 40kHz PWM harmonics.

(Legend of PM loss density distribution in Wm^{-3})

4.3.3.1 Introduction of a Conducting Rotor Shield

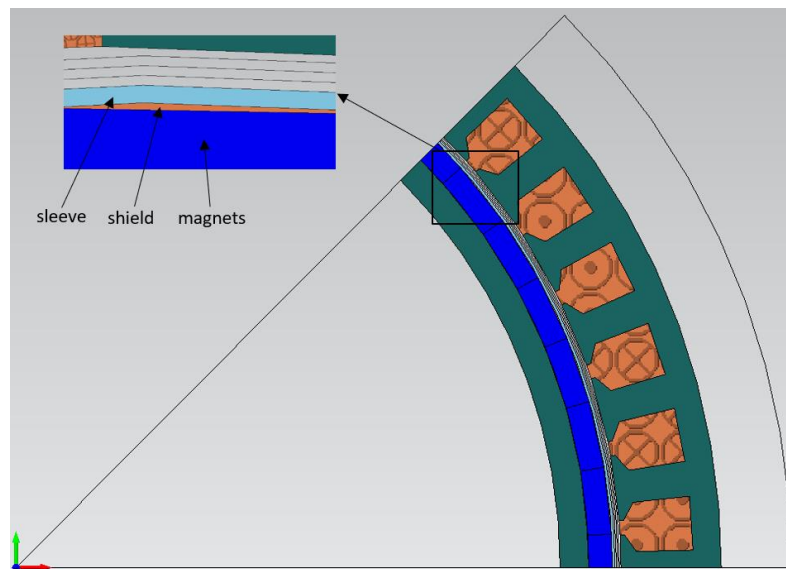


Figure 4-14: 1/8th model of the motor with rotor sleeve and copper shield

The high frequency time harmonic fields produce eddy currents in the magnets which effectively cancel out the stator time harmonic MMF and stop deep penetration of the harmonic flux into the rotor. The rotor MMF is therefore effectively equal to the harmonic MMF of the stator. The addition of a copper shield between the PM and the

protective sleeve has been proposed. The copper shield has a high electrical conductivity and hence can carry the time induced eddy currents with far less loss than the highly resistive magnets. Figure 4-14 shows a model of a motor where the rotor sleeve is non-magnetic, with a copper shield inside the sleeve. Figure 4-15 shows the loss density distribution of the permanent magnets with a 0.1 mm copper shield for a motor with time-harmonic input currents.

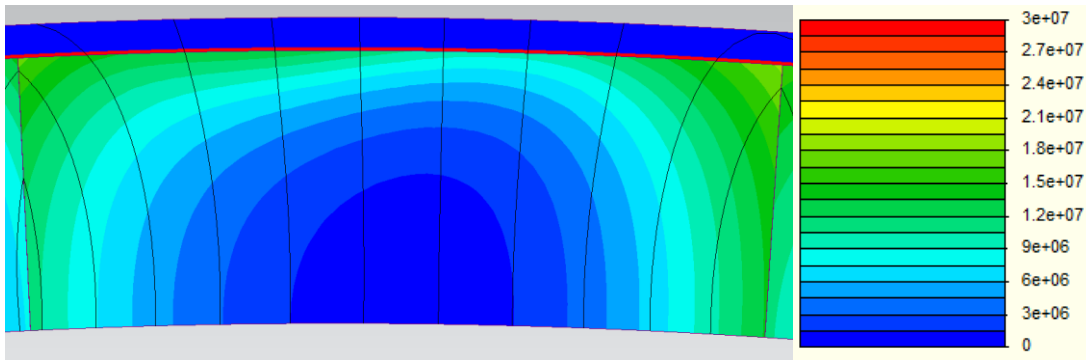


Figure 4-15: PM loss density distribution for the motor with 0.1mm copper shield

A comparison with Figure 4-13 shows that the losses in the PMs are greatly reduced when the copper shield is added. However, very large losses are generated in the copper shield. This results in a significant increase in the total rotor losses, which will cause excessive rotor heating and very low efficiency. Figure 4-16 shows the PM and copper shield losses for different copper shield thicknesses excited by an input current with additional 40kHz PWM harmonics.

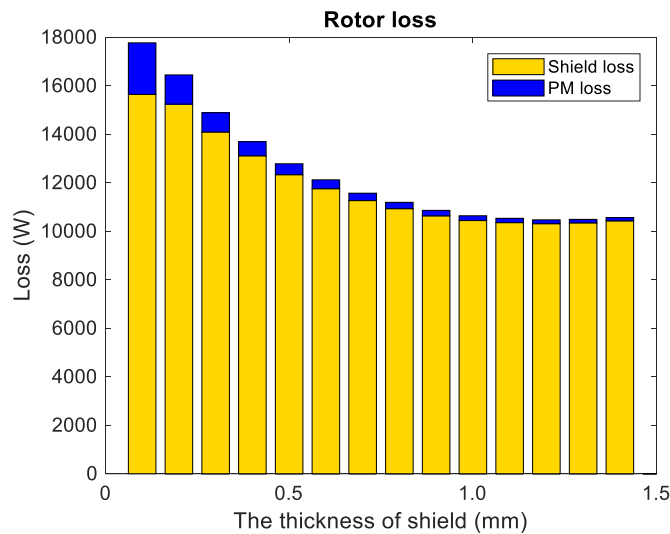


Figure 4-16: Rotor loss with current with additional 40kHz PWM harmonics

As can be seen from Figure 4-16, with the addition of the copper shield to the rotor, most of the losses are generated in the copper shield. Also, the thickness of the copper shield has an influence on the rotor losses. As the thickness of the copper shield increases, the losses decrease for both the copper shield and the PMs. This is because the resistance of the copper shield decreases as the thickness increases, which reduces the losses in the copper shield until its thickness exceeds the eddy current skin depth.

The above leads to the question as to why the shield has such high losses, when other researchers have demonstrated it to be effective [148], [149]. Closer examination of the shield currents has revealed that, whilst the time harmonics are cancelled effectively without excessive losses, it is the space harmonics of flux which are causing the very high shield loss. The space harmonics of stator MMF are both large and at a much lower frequency than the time harmonics, so that the space harmonic flux can penetrate through the shield. Under these conditions, which are sometimes referred to as “flux forced”, the eddy current losses are directly proportional to the conductivity of the shield, and it therefore increases this component of rotor loss.

Previous cases of successful use of an eddy current shield have been employed on motors with distributed windings, where there are small space harmonics for flux. It became clear that an eddy current shield could not be successfully employed in a machine with single tooth windings because the large space harmonics of flux induce excessive sleeve losses.

4.3.3.2 Rotor cage in q axis

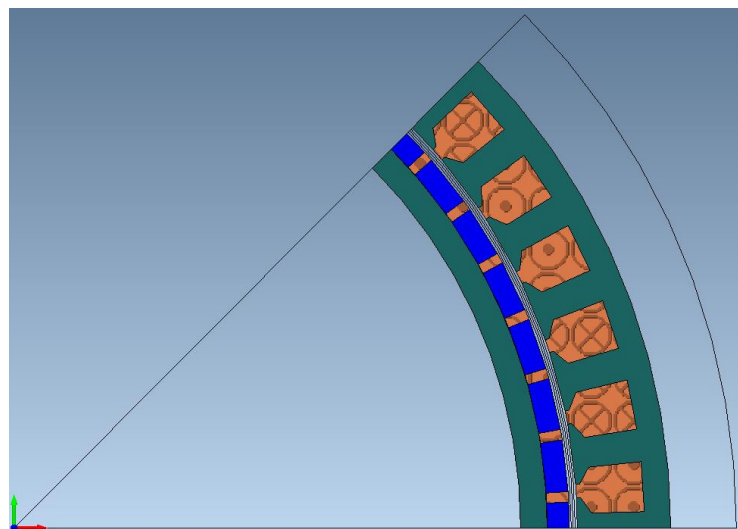


Figure 4-17: Structure of model with rotor cage on the q-axis

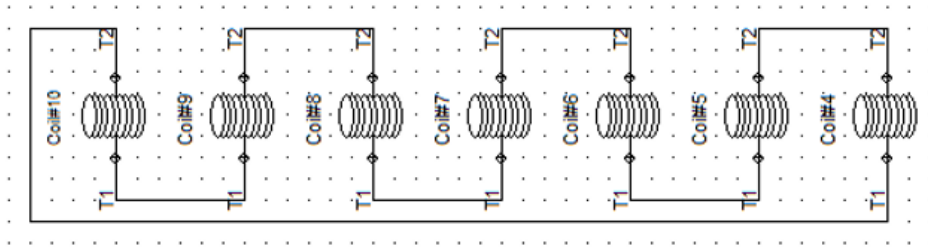
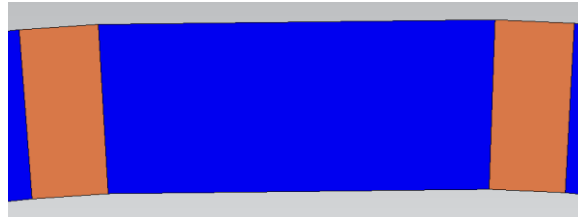
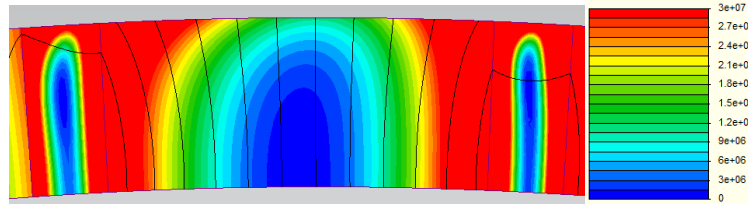


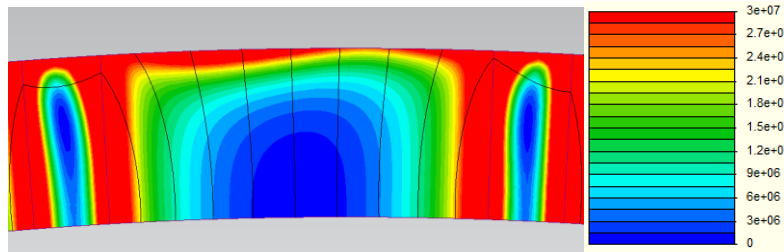
Figure 4-18: The connection of the rotor cage



(a)



(b)



(c)

Figure 4-19: (a) The structure of the PM with rotor cage on q-axis (b) PM losses distribution with ideal current input (c) PM losses distribution with current with a 40kHz switch frequency

The question was therefore posed as to whether an eddy current shield could be created to reduce the time harmonic losses, without incurring large space harmonic losses. A cage concept was studied, with the cage consisting of copper bars in the q-axis, with the bars all shorted at the axial ends of the machine. It was thought that this cage would not link any even space harmonics of flux and may produce a successful solution.

Figure 4-17 shows a radial cross-section of one-eighth of the motor with the rotor cage on the q-axis. The coppers bars are shorted, as demonstrated by the effective circuit diagram in Figure 4-18. The loss distribution with different current inputs is shown in Figure 4-19, and Table 4-7 illustrates the specific loss values for PMs and cages with different input currents.

Table 4-7: PM and cage loss with different input current

	Motor without rotor cage		Motor with rotor cage	
	Ideal current	40kHz THD 5.8 %	Ideal current	40kHz THD 5.8 %
Total loss (W)	5682	7432	5755 (101%)	7560 (102%)
PM loss (W)	5682	7432	3616 (64%)	5327 (72%)
Cage loss (W)			2139	2233

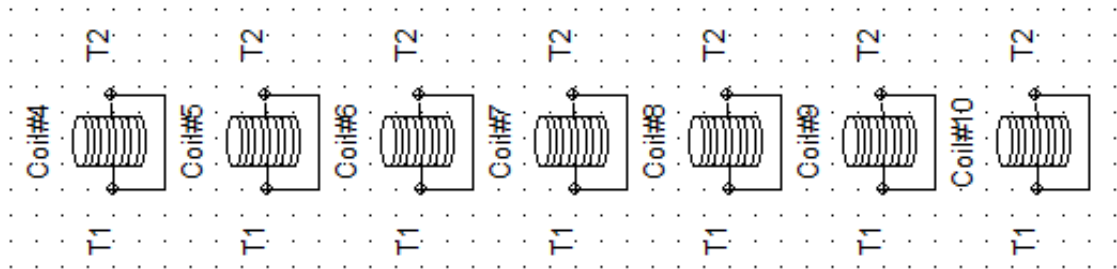
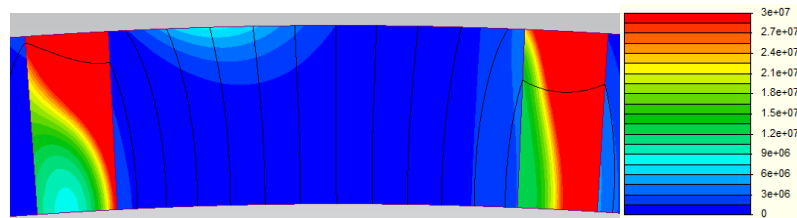
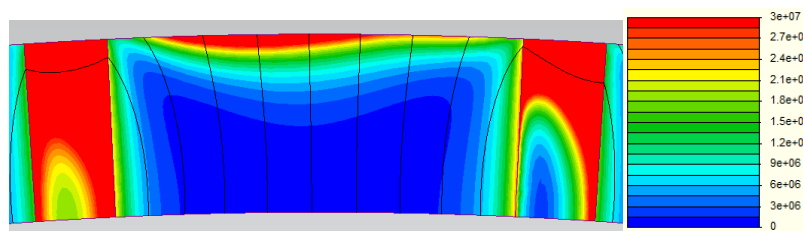


Figure 4-20: The connection of the rotor cage



(a)



(b)

Figure 4-21: (a) PM losses distribution with ideal current input (b) PM losses distribution with current with a 40kHz switching frequency

From Figure 4-19 and Table 4-7, compared with the model without the rotor cage, the magnet loss dropped 36% for the ideal current and 28% for the current with a 40kHz switching frequency due to the rotor cage on the q axis. However, there continue to be large losses generated in the rotor cage by the space harmonics, so that the total loss comprising PM loss and cage loss is almost unchanged.

In order to understand whether the connection of the rotor cage affects the PM loss, another rotor cage connection is shown in Figure 4-20. Each copper cage now forms a short circuit. With this arrangement the cage will stop non-integer space harmonics. Figure 4-21 shows the loss distribution in the PMs while inputting different currents. The total PM loss and cage loss are displayed in Table 4-8.

Table 4-8: PM and cage loss with different input current

	Motor without rotor cage		Motor with rotor cage	
	Ideal current	40kHz THD 5.8 %	Ideal current	40kHz THD 5.8 %
Total loss (W)	5682	7432	3691 (65%)	4337 (58%)
PM loss (W)	5682	7432	193 (3%)	1154 (16%)
Cage loss (W)			3498	3183

Regardless of the type of current, the PM loss is significantly reduced. For the ideal current, it drops to 193W, which means a 96.60% reduction in losses compared to the motor without the rotor cage. Meanwhile, for the current with a 40kHz switch frequency, it has an 84% reduction, which decreases from 7432W to 1154W. However, compared to the previously proposed connection, it is notable that the cage loss has increased by around 150%. Although this connection reduces total losses by almost half, excessive losses in the copper cage can still cause thermal damage to the PMs. As a result, the rotor cage on both d-axis and q-axis has been proposed.

4.3.3.3 Rotor cage on the d-axis and q-axis

Figure 4-22 illustrates the structure of the model with the rotor cage on both d-axis and the q-axis. There are two short circuits above the rotor, one is for the rotor cage on the d axis and the other one on the q axis. The loss distribution of the PM for two different input currents is shown in Figure 4-23 and the calculated loss is presented in Table 4-9.

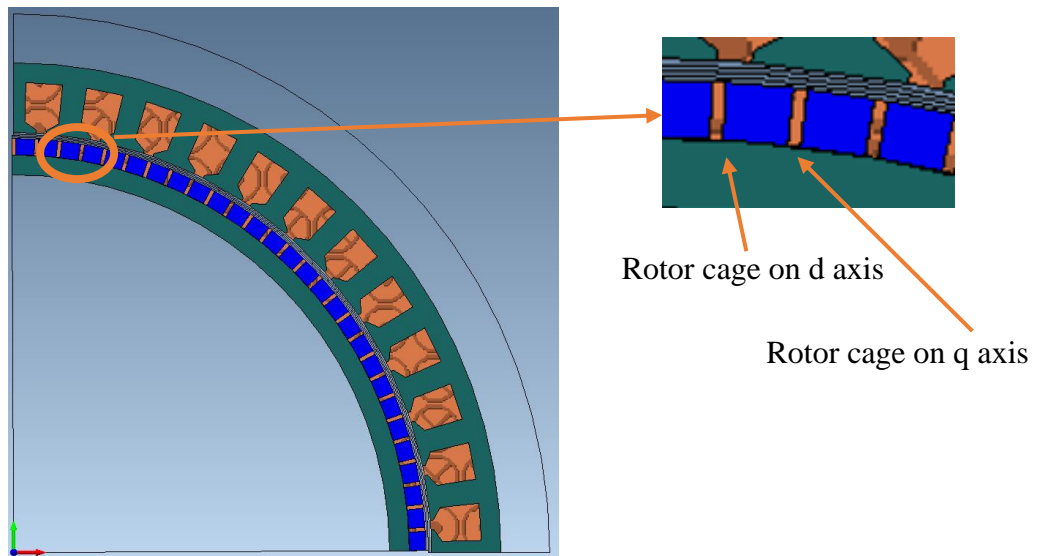
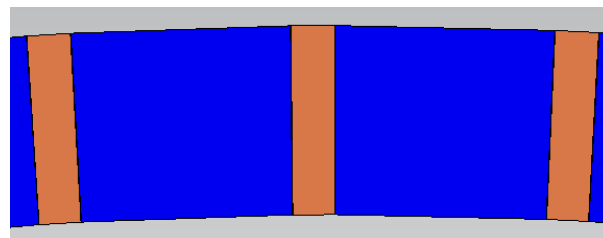
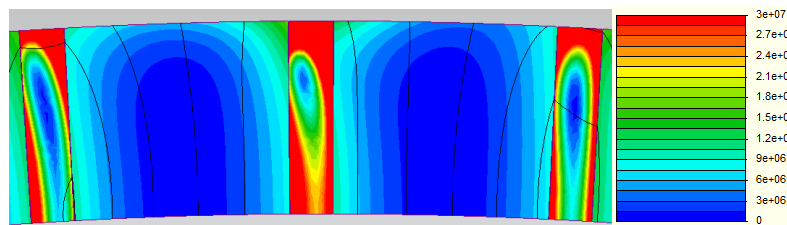


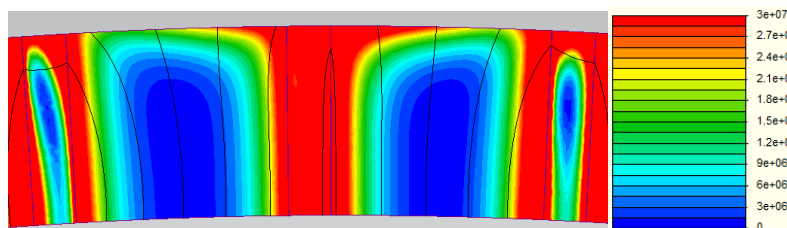
Figure 4-22: Structure of model with rotor cage in d axis and q axis



(a)



(b)



(c)

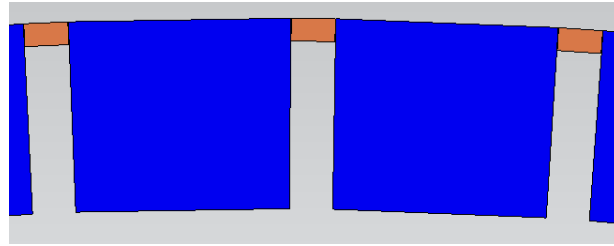
Figure 4-23: (a) The structure of the PM with rotor cage on both d-axis and q-axis (b) PM losses distribution with ideal current input (c) PM losses distribution with current with a 40kHz switch frequency

Table 4-9 compares the total loss which includes PM loss and cage loss. Because copper bars are inserted in both the d-axis and the q-axis to achieve an effect similar to that of circumferential segmentation PMs, the PM loss of the motor with rotor cage is compared with those of the motor with circumferential segmentation only. For the ideal input current, the motor with the rotor cage has a 39.08% reduction in PM loss. Although the rotor cage reduces some of the PM losses caused by the space harmonics, the space harmonics result in 1798 W of additional losses in the rotor cage. Meanwhile, for the current with a 40kHz switch frequency, the PM loss decreased from 5382W to 4091W while adding the rotor cage. However, the total loss including PM loss and cage loss has a 138% increase due to the harmonic effect on the rotor cage. As a result, the rotor cage insert in both the d-axis and the q-axis could have a 39.08% and 23.99% reduction in PM loss respectively for different current inputs, but the overall loss still rises when calculating the loss on the rotor cage.

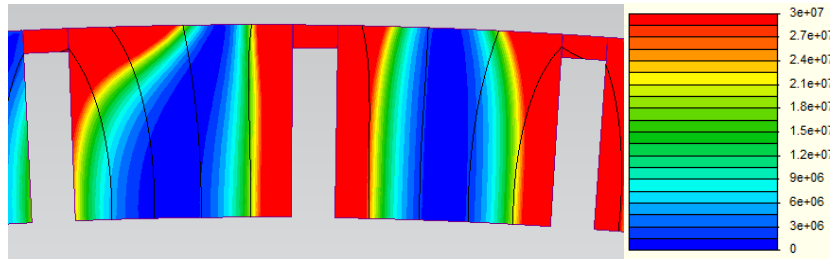
Table 4-9: PM and cage loss with different input currents for different models

	Motor with circumferential segmentation		Motor with rotor cage	
	Ideal current	40kHz THD 5.8 %	Ideal current	40kHz THD 5.8 %
Total loss (W)	1960	5382	2992 (153%)	7415 (138%)
PM loss (W)	1960	5382	1194 (61%)	4091 (76%)
Cage loss (W)			1798	3324

This approach does reduce the losses in the PMs considerably at the cost of much higher losses in the rotor cage. It has been proposed to optimize the rotor cage, as shown in Figure 4-24 (a), by applying a smaller volume rotor cage at the surface of the rotor, with the thinking that this may reduce radial penetration of the flux. Meanwhile, the PM loss distribution for current with 40kHz switch frequency is described in Figure 4-24 (b) and the calculated loss is illustrated in Table 4-10. According to the simulation results, compared with Table 4-9, the losses on PMs are again reduced from 4091W to 3409W and the cage loss reduces by 1122W as well. Although the total losses still increase compared to the motor without the rotor cage, they drop by 1804 W when the large cage is replaced by a small cage.



(a)



(b)

Figure 4-24: (a) The structure of the PM with a small rotor cage on both d-axis and q-axis (b) PM losses distribution with current with a 40kHz switch frequency

Table 4-10: PM and cage loss of motor with a small rotor cage with current with a 40kHz switch frequency

	Motor with circumferential segmentation	Motor with rotor cage
Total loss (W)	5382	5611 (104%)
PM loss (W)	5382	3409 (63%)
Cage loss (W)		2202

4.3.3.4 Three-phase rotor cages over PMs

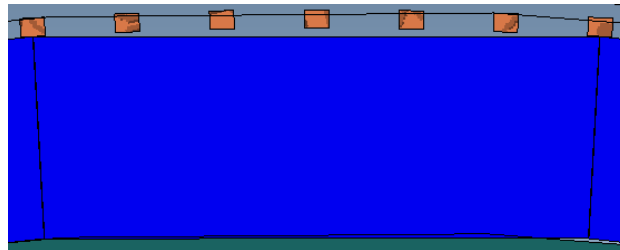
Figure 4-25 shows the structure of the model with a three-phase rotor cage in order to decrease the PM loss. In this model, there are three short circuits which means every two conductors connect together to form a circuit. The PM losses are given in Table 4-11 and Table 4-12 respectively. Also, the model with circumferential segmentation has been considered as shown in Figure 4-26.

Table 4-11: Ideal input current

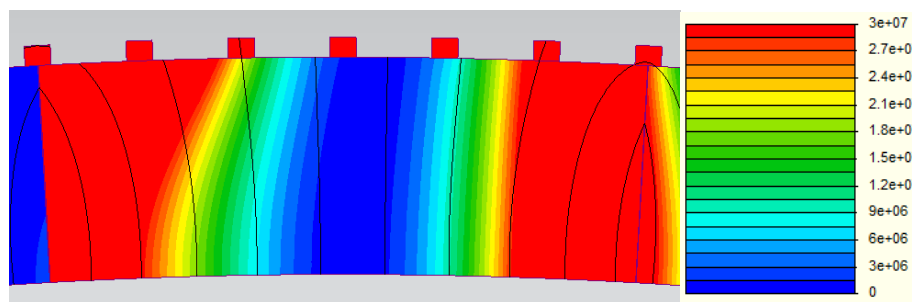
	Motor without rotor cage		Motor with rotor cage	
	without segmentation	with segmentation	without segmentation	with segmentation
Total loss (W)	5682	1960	7164	4108
PM loss (W)	5682	1960	4482	1318
Cage loss (W)			2682	2790

Table 4-12: Current with 40kHz time-harmonic

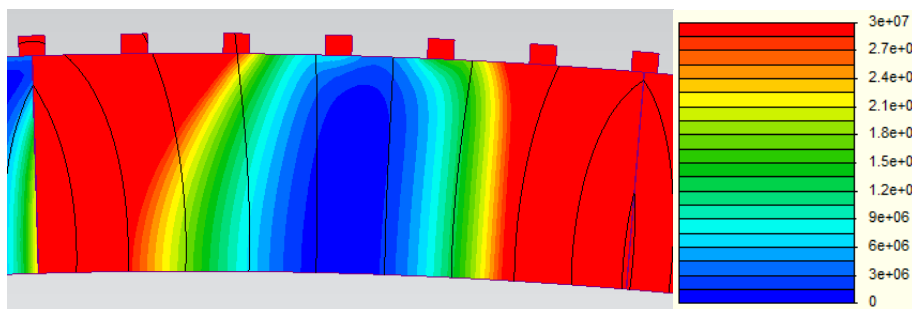
	Motor without rotor cage		Motor with rotor cage	
	without segmentation	with segmentation	without segmentation	with segmentation
Total loss (W)	7432	5382	8635	6774
PM loss (W)	7432	5382	5894	3901
Cage loss (W)			2741	2873



(a)

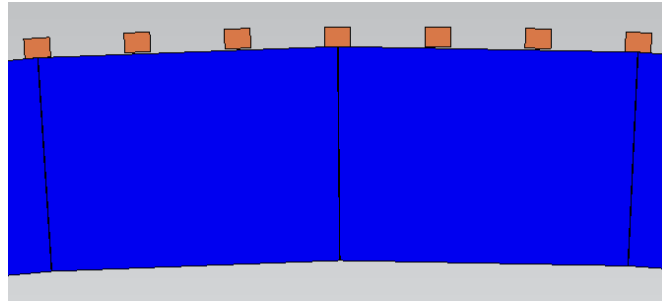


(b)

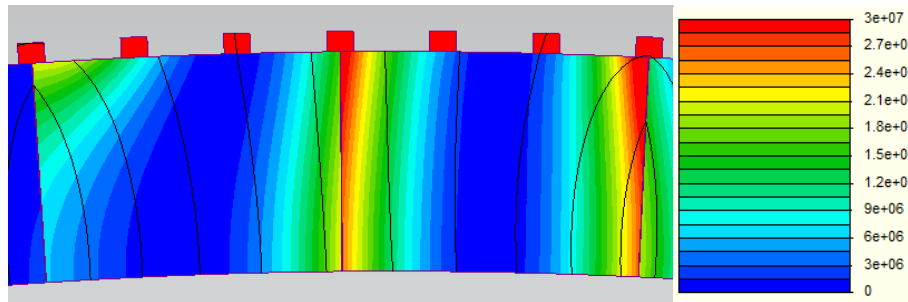


(c)

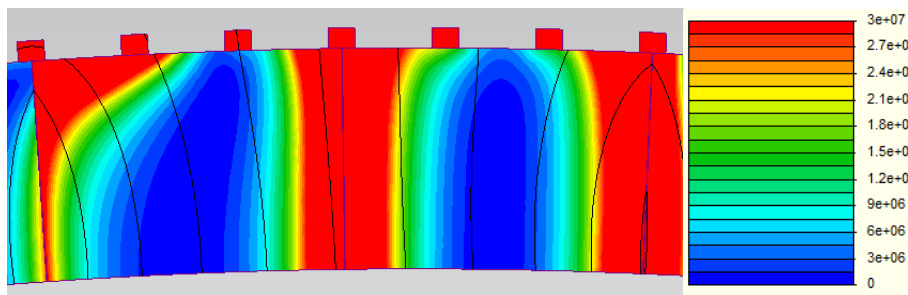
Figure 4-25: (a) The structure of the small rotor cage above PM (b) PM losses distribution with ideal current input (c) PM losses distribution with current with a 40kHz switch frequency



(a)



(b)



(c)

Figure 4-26: (a) PM with circumferential segmentation and small rotor cage (b) PM losses distribution with ideal current input (c) PM losses distribution with current with a 40kHz switch frequency

The results in Table 4-11 show that the total loss including magnets loss and cage loss increased by nearly 1500W while adding the rotor cage. There is because the space harmonic forms a closed loop through the rotor cage and generates huge losses in the cage. However, when a current with time harmonics is fed in, the losses in the rotor cage do not increase much in relation to the effects of space harmonics, and the losses in magnets increase less than in the model without the rotor cage. This is because the rotor cage prevents flux penetration and the low resistance of the copper rotor cage results in a small increase in losses in the rotor cage.

The overall conclusions are that none of the cage concepts has been particularly successful. Moving from a continuous shield to a cage shield has reduced the losses in the shield, but at the expense of poorer shielding of the magnets.

4.3.4 The interior PM motor

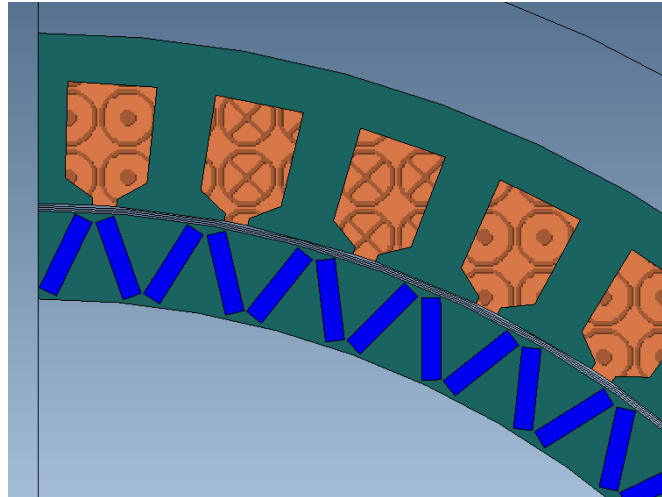


Figure 4-27: The structure of the interior PM model

Figure 4-27 shows the structure of the interior PM model, and the rotor loss is shown in Table 4-13.

Table 4-13: The rotor loss of the interior PM model

	Ideal current	Current with 40kHz time-harmonics
Rotor loss (W)	4015	5272
PM loss (W)	3962	5139
Iron loss (W)	53	133

Table 4-13 shows the rotor loss with idea current and time-harmonic respectively. The PM loss increases by 30% due to the current time-harmonics. However, the magnet losses are reduced compared to the surface-mounted PM motor, especially in the case of input currents with time harmonics. This is because, for the structure with surface-mounted PM, there are two different magnetic circuits: one is stator tooth – permanent magnet – rotor core – stator tooth and another passes through stator teeth – rotor core – stator teeth. In the case of the interior PM model, there is an additional path, stator teeth – rotor core surface – stator teeth and the time-harmonic flux passes more through the rotor core to form a closed loop. Therefore, the eddy current losses in the PMs are significantly reduced.

4.3.4.1 Circumferential segmentation

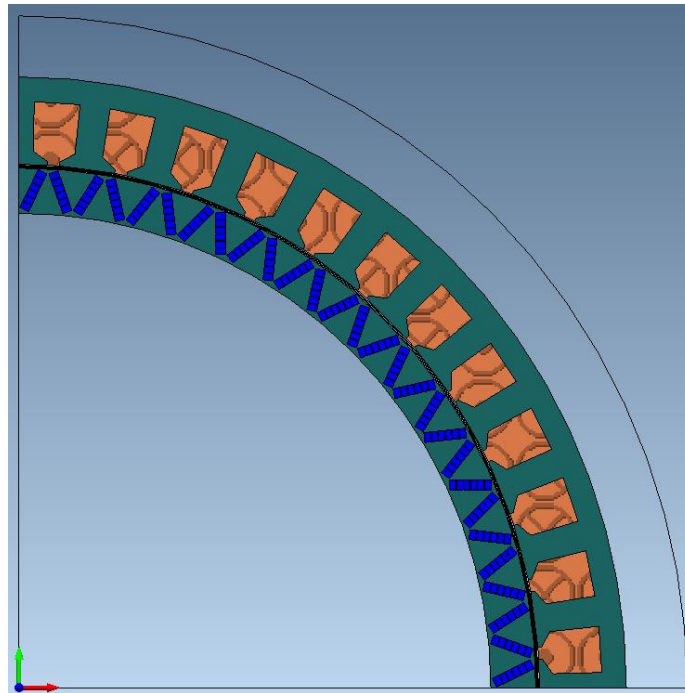


Figure 4-28: The interior PM model with circumferential segmentation

Figure 4-28 shows the model with PM segmentation in the circumferential direction. The rotor with different current inputs is recorded in Table 4-11 and Table 4-12 respectively. Also, the trend of the PM loss with circumferential segmentation is illustrated in Figure 4-26. From Figure 4-29, the PM loss decreases sharply when the PMs split from one to two. For the model with sinewave current, the PM loss decreased by 96 % when the number of segments increased to 6. Also, the model with time-harmonic reduces 82% loss while splitting the PMs into 6 pieces. Clearly the time harmonic induced losses are greatly reduced with the interior PM configuration. This seems to give the overall lowest rotor loss when combining interior magnets with segmentation and no shielding.

Table 4-14: The PM loss of interior PM model with ideal current

No. of segmented PMs	1	2	3	4	6
PM loss (W)	3962	1024	457	264	130
Rotor Iron loss (W)	53	54	58	60	68
Rotor loss (W)	4015	1078	515	324	198

Table 4-15: The PM loss of interior PM model with 40kHz time-harmonic

No. of segmented PMs	1	2	3	4	6
PM loss (W)	5139	2848	2234	1603	929
Rotor Iron loss (W)	133	139	174	189	211
Rotor loss (W)	5272	2987	2408	1792	1140

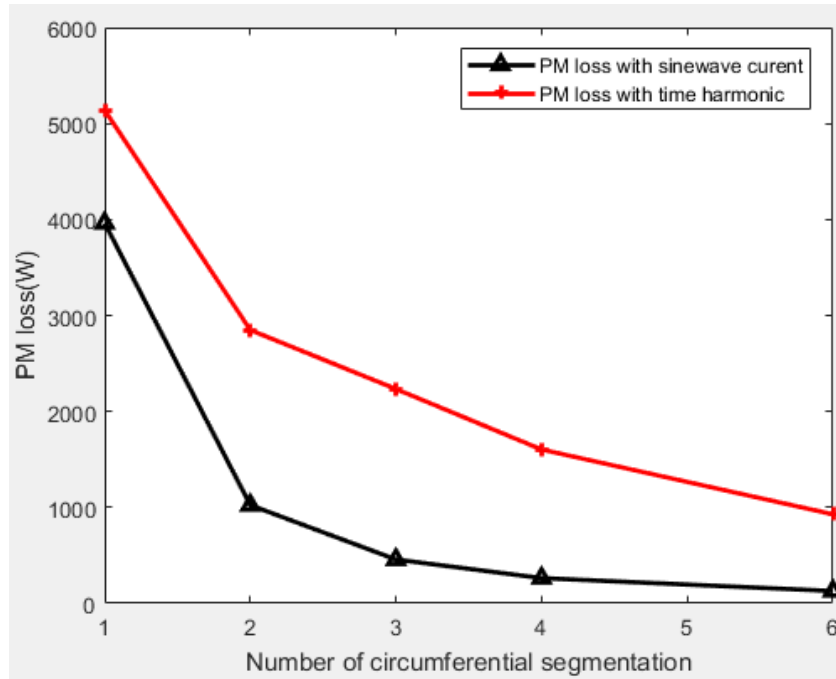


Figure 4-29: The PM loss of interior PM model with circumferential segmentation

4.3.4.2 Axial segmentation

Figure 4-30 described the trend of PM loss while inputting different currents and split the PMs in an axial direction from two to eight. Table 4-16 and Table 4-17 show the losses and the dimension of the PMs with axial segmentation. From the figure and tables, the huge loss is reduced while the PMs split into two pieces in the axial direction. Compared with circumferential segmentation, the model with sinewave current input both reduces 87% loss on PMs while splitting the PMs from two to six pieces. However, for the input current with time-harmonic, these two models reduce 67% and 81% loss respectively. It seems that axial segmentation is just as effective as circumferential segmentation.

Table 4-16: The rotor loss of interior PM model with ideal current

No. of segmented PMs	2	3	4	6
PM length	14 mm	9 mm	6.5 mm	4 mm
PM loss (W)	2380	1365	791	299
Iron loss (W)	76	81	81	89
Rotor loss (W)	2456	1446	872	388

Table 4-17: The rotor loss of interior PM model with 40kHz time-harmonic

No. of segmented PMs	2	3	4	6
PM length	14 mm	9 mm	6.5 mm	4 mm
PM loss (W)	3682	2392	1813	708
Iron loss (W)	376	400	429	455
Rotor loss (W)	4058	2792	2242	1163

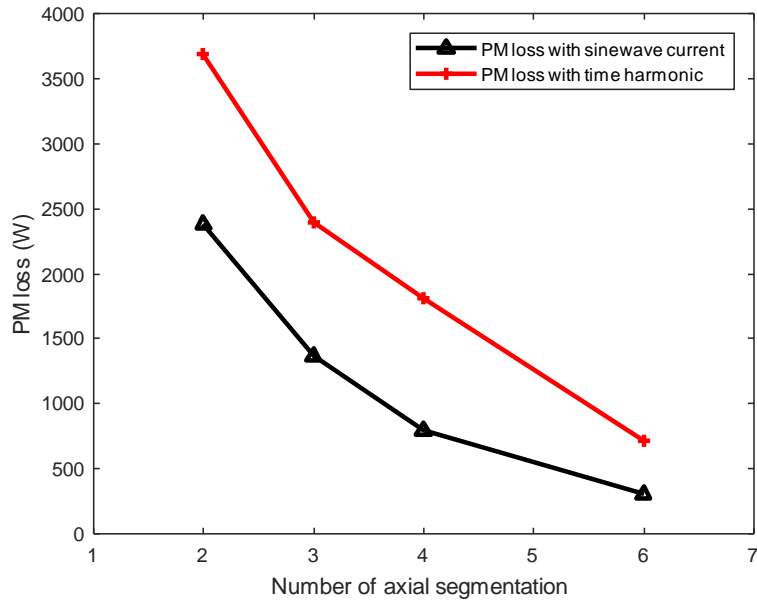


Figure 4-30: The PM loss of interior PM model with axial segmentation

4.3.4.3 The model with rotor cage

In this part, the model with rotor cage and PM segmentation has been discussed. Figure 4-31 shows the model with a rotor cage over the PMs. The trend of the rotor loss has been illustrated in Figure 4-32. Also, the results of the simulation which include PM loss, cage loss and rotor iron loss are shown in Table 4-18 and Table 4-19.

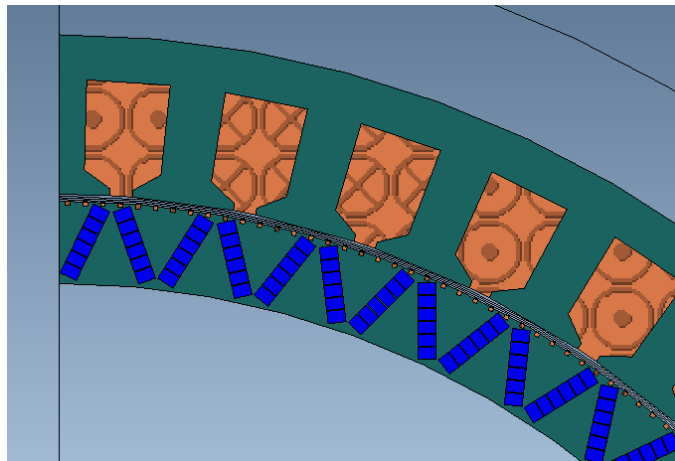


Figure 4-31: The interior PM model with circumferential segmentation and rotor cage

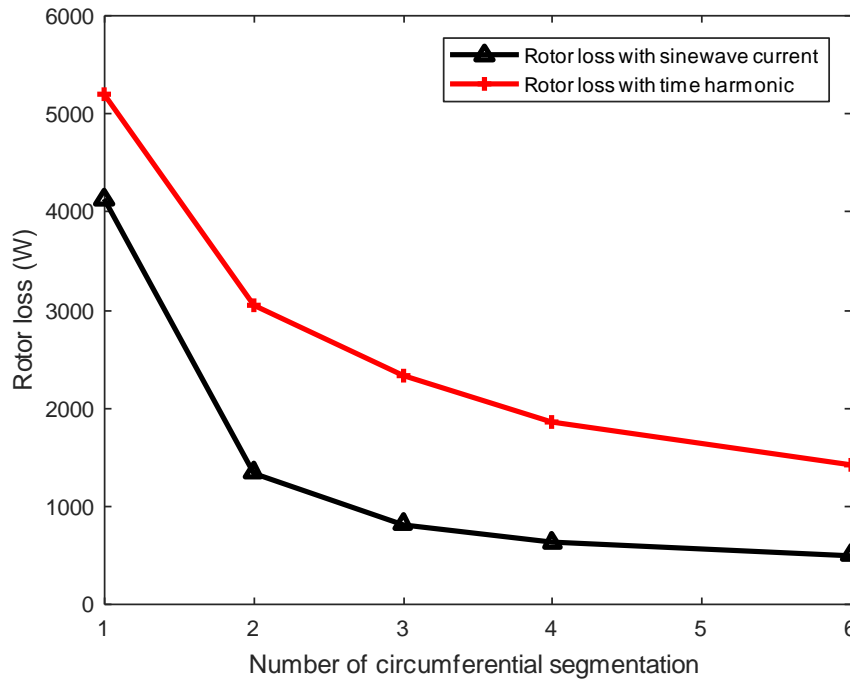


Figure 4-32: The Rotor loss of interior PM model with circumferential segmentation and rotor cage

Table 4-18: The rotor loss of interior PM model with rotor cage and sinewave current

No. of segmented PMs	1	2	3	4	6
PM loss (W)	3755	968	437	253	124
Cage loss (W)	320	318	319	317	313
Rotor Iron loss (W)	51	53	56	57	62
Rotor loss (W)	4126	1339	812	627	499

Table 4-19: The rotor loss of interior PM model with rotor cage and time-harmonic

No. of segmented PMs	1	2	3	4	6
PM loss (W)	4467	2291	1543	1069	607
Cage loss (W)	629	636	641	647	648
Rotor Iron loss (W)	109	119	137	143	164
Rotor loss (W)	5205	3047	2321	1859	1419

Table 4-20: The rotor loss of interior PM model with rotor cage, time-harmonic and axial segmentation

No. of segmented PMs	2	4	6	8
PM length	14 mm	6.5 mm	4 mm	2.75 mm
PM loss (W)	3515	1537	569	306
Cage loss (W)	766	268	782	519
Rotor loss (exclude Iron loss) (W)	4281	1805	1351	825

Table 4-20 shows the model with rotor cage and axial segmentation. Compared with the model, which split PMs in the circumferential direction and PM loss by 74%, it decreased PM loss by 84% as the number of the PM segments increased from two to six. However, the cage generates more loss when splitting the PMs in the axial direction.

4.3.5 Comparison

Table 4-5 and Table 4-13 show the losses of the surface mounted and interior magnet rotors without any segmentation or screening. With 7.4kW of magnet loss, the surface mounted magnet loss exceeds that of the interior magnet, which has 5.2kW of loss. The main cause of this difference is a reduction in the magnet losses due to space harmonics of flux in the interior magnet design. Space harmonic losses comprises 5.7kW with the surface mounted magnets and just under 4kW with the interior magnets. Time harmonic induced losses are 1.75kW with the surface mounted magnets, falling to 1.2kW with the interior magnets. Overall, this data shows that, compared with the surface-mounted PM motor, the interior PM model could reduce PM loss by about 30%.

Axial segmentation is very effective at reducing space harmonic losses. For example, with six axial segments, the space harmonic losses are reduced by 83% and 87% for the two magnet arrangements. Circumferential segmentation is equally effective.: the surface-mounted PM motor reduces space harmonic losses by 88% when the PM is segmented from one to four pieces. The interior PM model can also decrease losses by 87%, although the PMs need to separate into six pieces. Segmentation has less effect upon the high frequency time harmonic losses. Circumferential segmentation could reduce more loss by 69% in the interior PM model compared to 34% in the surface-mounted PM motor when the PMs are split into four pieces.

A range of shielding cages have been investigated with limited success. This method reduces the overall rotor losses by at least 20% when compared to a surface-mounted motor with a copper shield.

Compared to motors without any rotor cage or copper shielding, the overall rotor loss increased when adding the rotor cage. The PM losses tend to decrease, but this is more than countered by large shielding losses.

In summary space harmonic induced losses can be reduced by over 80% by segmentation in the axial or circumferential directions. Time harmonic induced losses are also reduced but by a smaller margin.

4.4 Conclusion

This chapter calculates the winding losses including the influence of the AC current, and the magnet losses including the influence of the space and time harmonics. Segmentation of the magnets has been shown to be an effective method for reducing losses, whilst the use of eddy current screens has been shown to actually increase rotor losses and so is not recommended.

In the next chapter the structure of the motor model will be optimized to reduce space harmonics and a fault tolerant design will be proposed.

Chapter 5 Harmonic analysis and fault tolerant operation

5.1 Introduction

This chapter first analyses the non-synchronous winding harmonics of the previously proposed motor to reduce PM losses based on Fourier decomposition so that the complex, space-varying air-gap magnetisation field is decomposed into its constituent harmonics. Then some combinations of pole slots are selected to reduce harmonics and rotor losses, and their non-synchronous winding harmonics are analysed to select a suitable combination.

In order to improve the reliability of the motor, two fault-tolerant models are presented in the next section. Some key parameters have been calculated and optimised to maximise performance. This is followed by a discussion of healthy operation and fault conditions. In addition, methods for varying the peak fault current are considered. Finally, a comparison of two fault-tolerant designs is discussed.

5.2 Harmonic analysis

5.2.1 Analysis of the proposed model

In order to simplify the calculations, the motor is split into a series of units, with each unit comprising of 12 slots and 14 poles. This means that the previously proposed 48 slots, 56 poles single layer concentrated winding motor comprises four-unit motors.

Table 5-1: Slot angle distribution for a 12 slot and 14 poles unit motor

No. of slot	Electrical angle	Phase
1	0°	A+
2	210°	A-
3	60°	C-
4	270°	C+
5	120°	B+
6	330°	B-
7	180°	A-
8	30°	A+
9	240°	C+
10	90°	C-
11	300°	B-
12	150°	B+

Table 5-1 describes the slot angle distribution for this unit motor. The electrical angle is calculated according to Formula (5-1).

$$\theta_e = P \frac{360}{s} \quad (5 - 1)$$

Where θ_e is the electrical angle, P is the number of pole pairs, and s is the number of slots.

In order to derive the harmonic spectrum of the air gap magnetic field by FEA, the magnets are represented as demagnetised, as shown in Figure 5-1. The red line in Figure 5-1 is selected to obtain the magnetic field strength waveform of the air gap by field extractor as shown in Figure 5-2.

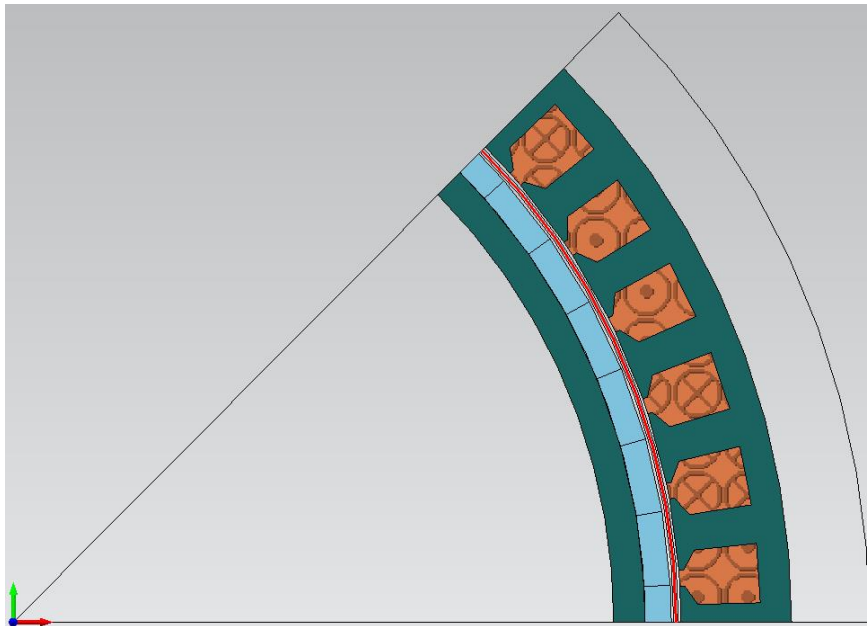


Figure 5-1: One-eighth of the motor

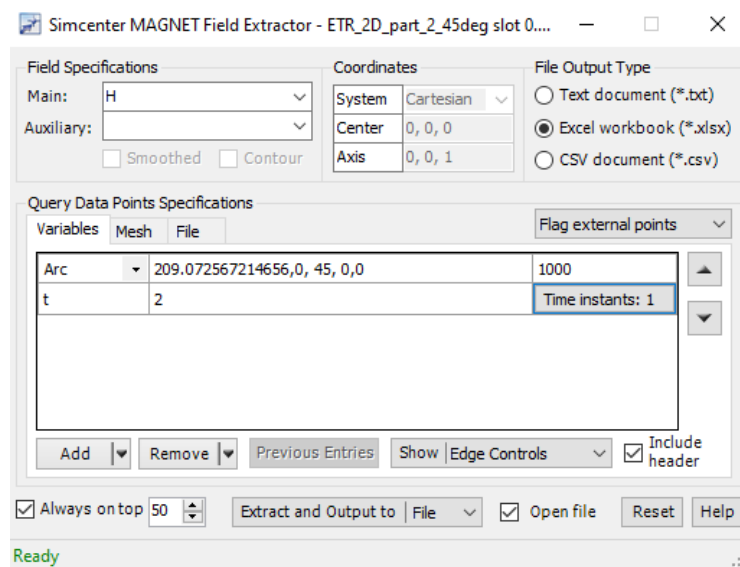


Figure 5-2: Field extractor in Simcenter MAGNET

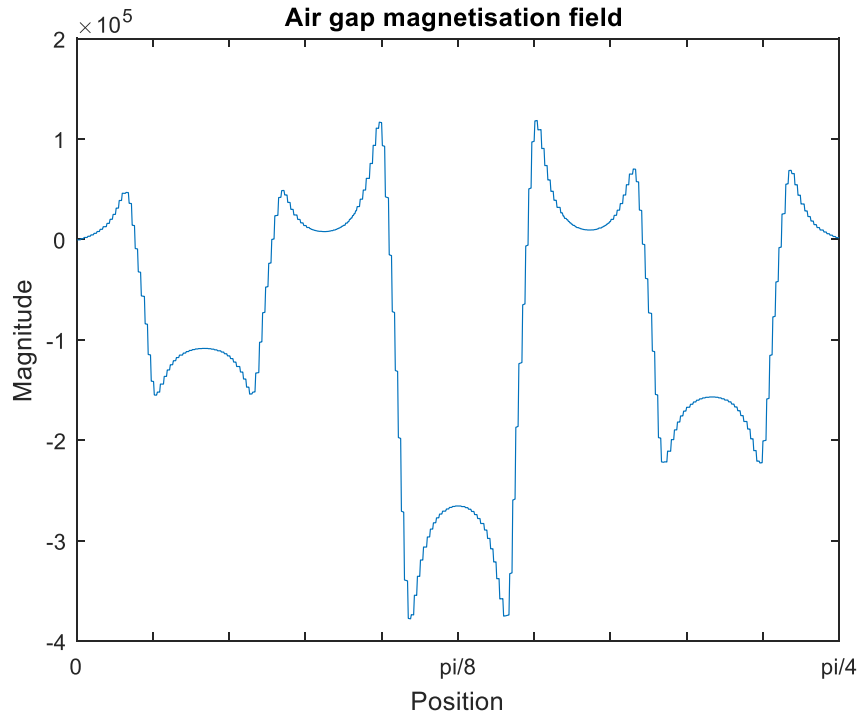


Figure 5-3: Air gap magnetisation field of the motor with 48 slots and 56 poles

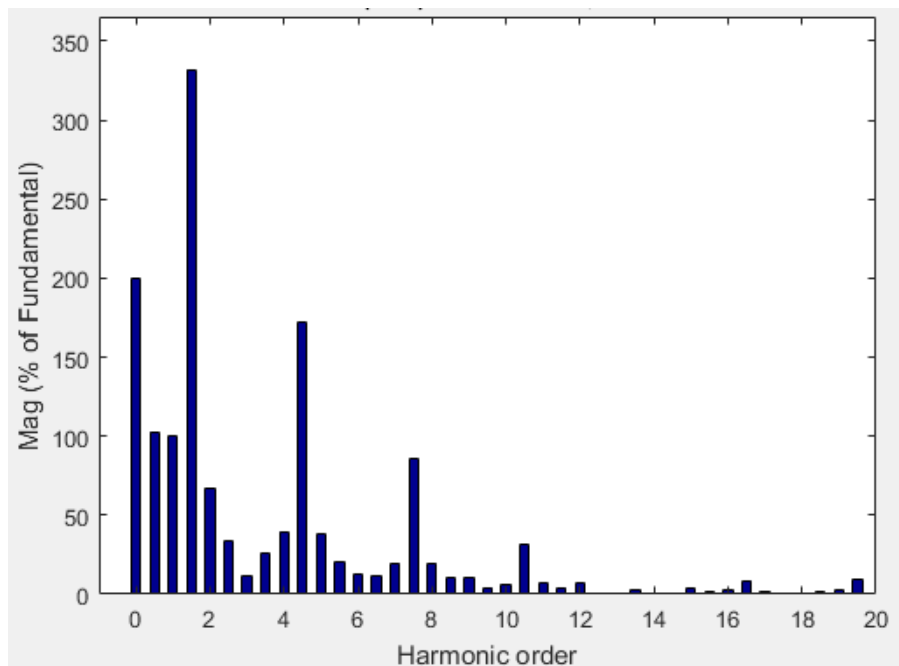


Figure 5-4: Air-gap harmonic spectrum of the motor with 48 slots and 56 poles

Figure 5-3 shows the variation of the magnetic field strength with air gap position for a motor with 48 slots and 56 poles when the input current is a perfect sinewave. According to Figure 5-3, the air gap harmonic spectrum is decomposed by the Powergui FFT Analysis Tool in MatLab Simulink, as shown in Figure 5-4.

5.2.2 Motor with 48 slots and 32 poles

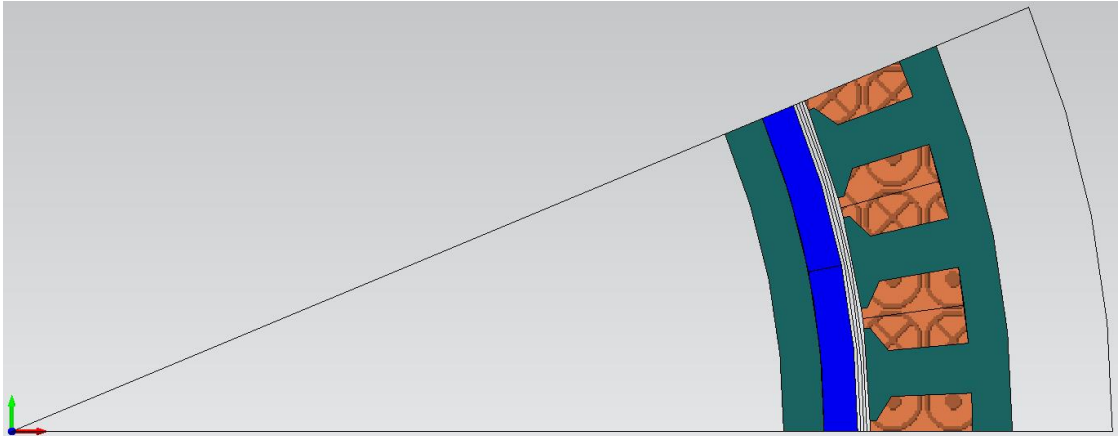


Figure 5-5: 1/16th of the motor with 48 slots and 32 poles

In order to reduce the effects of non-synchronous winding harmonics, motors with 48 slots and 32 poles are also proposed and compared, as shown in Figure 5-5. Table 5-2 describes the slot angle distribution for this unit motor.

Table 5-2: Slot angle distribution for 12 slots and 8 poles unit motor

No. of slot	Electrical angle	Phase
1	0°	A+
2	120°	B+
3	240°	C+
4	0°	A+
5	120°	B+
6	240°	C+
7	0°	A+
8	120°	B+
9	240°	C+
10	0°	A+
11	120°	B+
12	240°	C+

Figure 5-6 and Figure 5-7 show the air gap magnetisation field and air gap harmonic spectrum of the motor with 48 slots and 32poles respectively. A comparison with the previous motor shows that the motor with 48 slots and 32poles greatly reduces the non-synchronous winding harmonics that can produce eddy current losses in the PMs. Table 5-3 shows a comparison of the performance of the two motors.

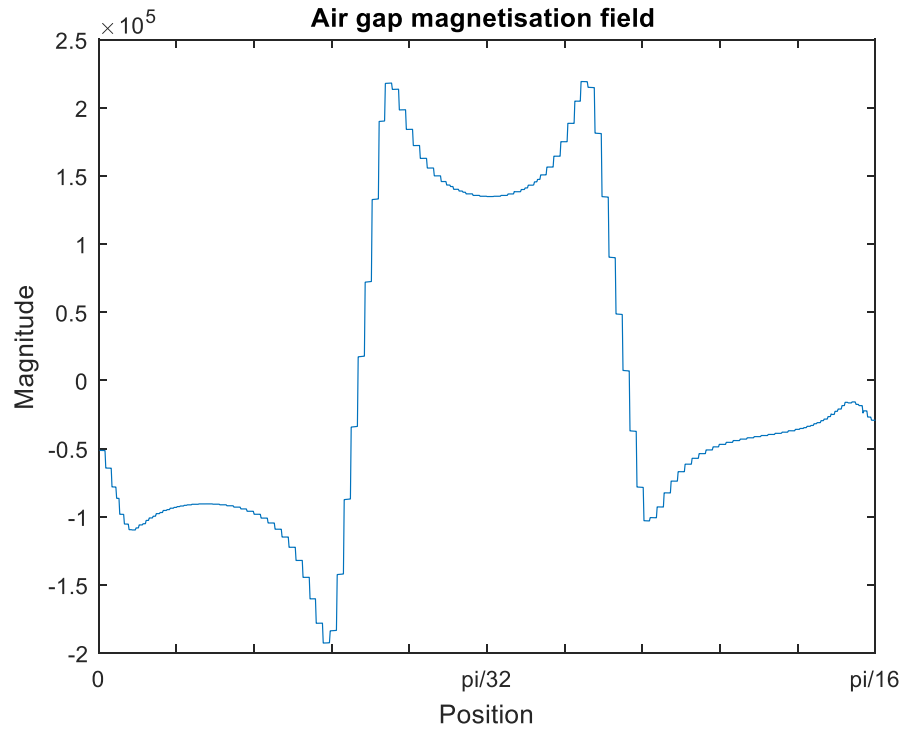


Figure 5-6: Air gap magnetisation field of the motor with 48 slots and 32 poles

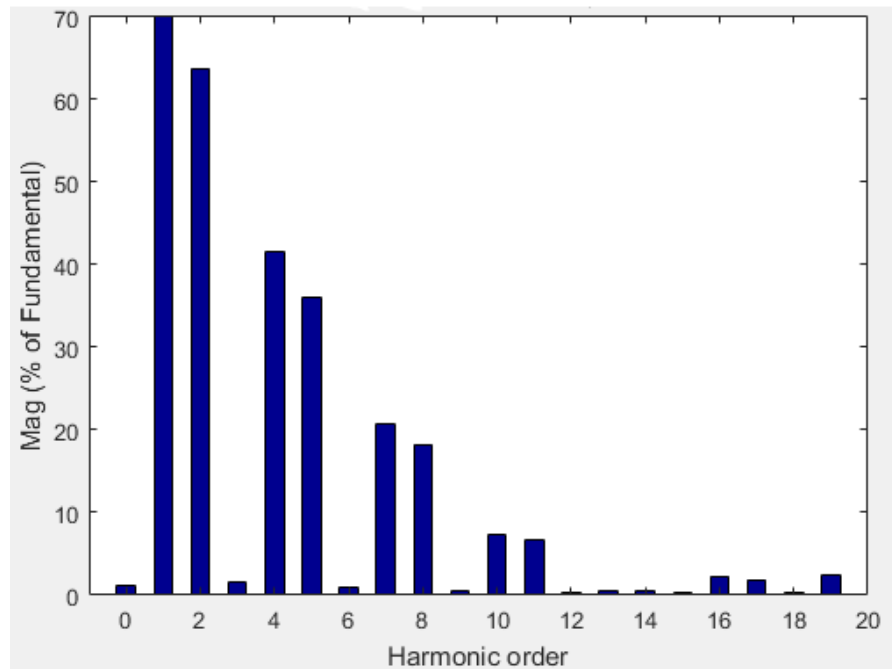


Figure 5-7: Air-gap harmonic spectrum of the motor with 48 slots and 32 poles

As can be seen from Table 5-3, the PM loss of the motor with 48 slots and 32 poles is reduced by 79% relative to the other motor when the same torque is output and the input

current has the same current density, before any optimisation method is added to the PMs, such as segmentation.

Table 5-3: Key parameters and performance comparison

Slots and poles	48 slots, 56 poles	48 slots, 32 poles
Output torque	310 Nm	310 Nm
Stator OD	490 mm	490 mm
Stator ID	420 mm	420 mm
Rotor OD	414 mm	414 mm
Rotor ID	380 mm	380 mm
Stack length	29 mm	29 mm
Air gap	3 mm	3 mm
PM thickness	8.25 mm	8.25 mm
Current density	10 A/mm ²	10 A/mm ²
PM loss	5682W	1179W

5.3 Fault-tolerant design

In this section, fault-tolerant designs are presented for motors with 48 slots and 32 poles. Because of the harsh operating environment, the electric tail rotor system requires high reliability and safety [135]. The use of multiphase machines which could allow the motor to operate continuously with a faulty phase is the main method under consideration [136, 137]. A short circuit at the terminals of a winding could occur due to either a winding fault or, more likely a fault in the power electronic converter. Under such circumstances it is necessary to limit the short circuit current, to prevent damage to the stator winding due to overheating. To reduce the short circuit current, the machine structure needs to be optimized to increase the inductance [138, 139]. Each unit of the machine can be supplied from a separate inverter, so that when one unit fails, the motor can maintain the output torque by increasing the current in the healthy units [140]–[142].

5.3.1 A comparison between two fault-tolerant designs

Two fault-tolerant designs have been selected for comparison. These two designs increase the number of poles from 32 to 34. The first one is an alternative segmented winding which separates the model into one upper and one lower lane, as shown in Figure 5-8. Figure 5-9 illustrates the second fault-tolerant design with essentially four lanes. If opposite lanes are connected in parallel to create a single lane, then a two-lane system results. This second alternative minimises unbalanced magnetic pull forces acting on the rotor structure. The differences between the two models are highlighted by the yellow circles.

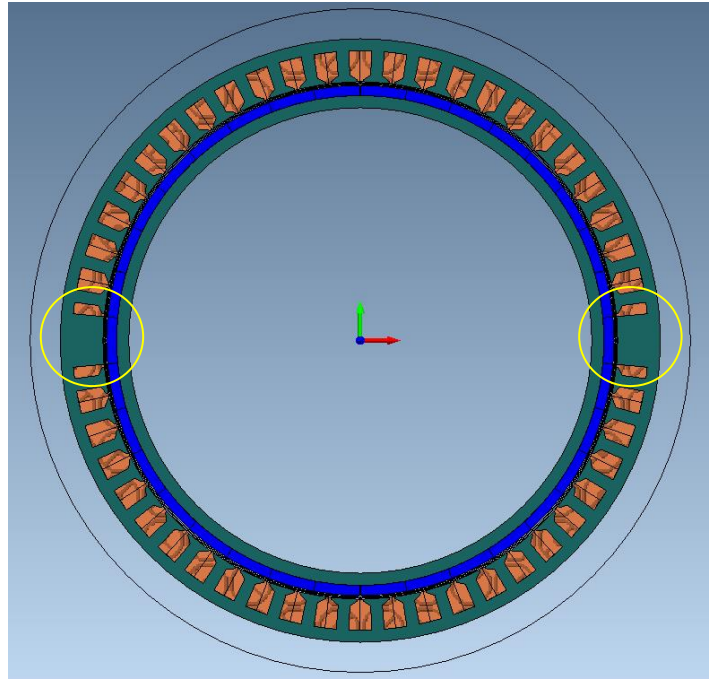


Figure 5-8: Fault-tolerant design with alternative segmented winding

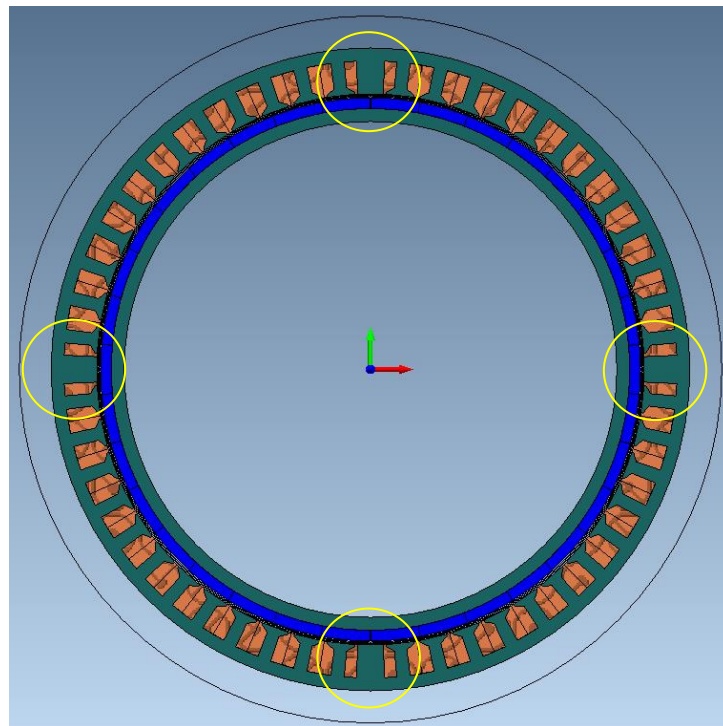


Figure 5-9: Fault-tolerant design with interspersed winding

5.3.2 Key parameters design

Helicopter manufacturers advise that, following a fault, the remaining healthy lane must be capable of producing two-thirds of the rated torque. The torque produced by the

healthy lane needs to increase by 33% as a consequence: this can be achieved by either increasing the stack axial length or by increasing the current density. Table 5-3 shows a comparison of the output torque and PM loss with different stack lengths and current input densities for the model with 48slots and 32poles.

Table 5-4: A comparison of the torque and PM loss

	Current density: 10 A/mm ²	Current density: 15 A/mm ²
Length: 29mm	402Nm (1179W)	581Nm (2310W)
Length: 39mm	541Nm (1586W)	781Nm (3107W)

In Table 5-4, when the length increases from 29 mm to 39 mm, the torque and PM loss increases by a factor of 1.34. However, when the current density rises by 50% from 10 A/mm² to 15 A/mm², the average torque only rises by 45% which expect to double because of magnetic saturation effects. Furthermore, the PM loss will nearly double.

The key parameters of the original model with a current density of 10 A/mm² which is designed to produce four-thirds of torque are shown in Table 5-3. When increasing the current density to 15 A/mm² and producing an output torque of 310Nm the stack length can be reduced to 15.5mm. Figure 5-10 shows the back-EMF of the basic model (48Slots, 32Poles) with the new stack length. Assuming the inductive voltage drop is the same size, the required back-EMF has been calculated in Table 5-5.

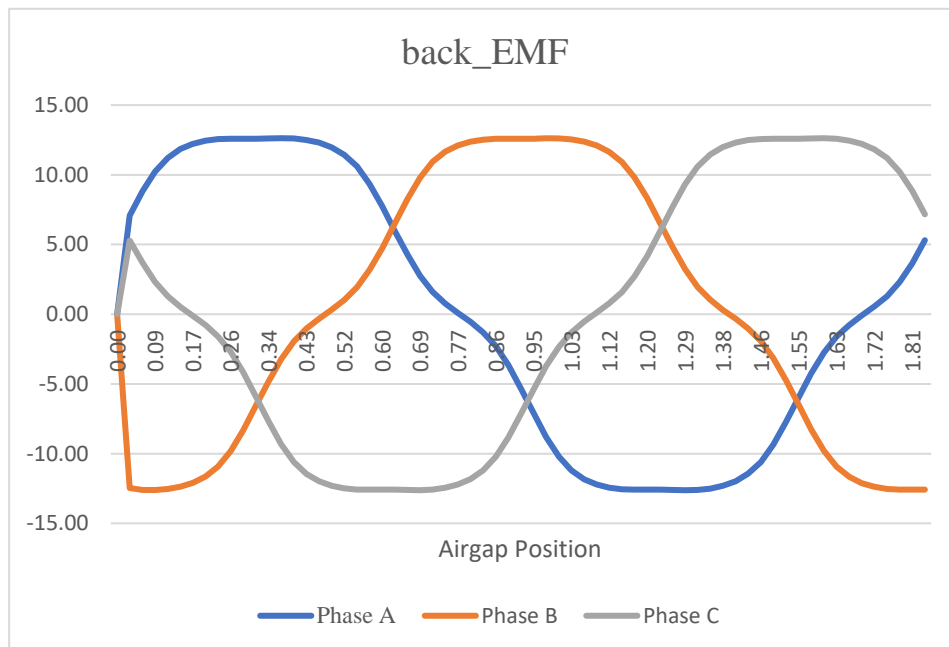


Figure 5-10: The back-EMF of the model (48Slots, 32Poles)

Table 5-5: Voltages needed to give the required back-EMF

Power supply	500 V
Peak line back-EMF	353.6 V
Peak back-EMF per phase	204.1 V
Peak line back-EMF of one set of coils	44.2 V
Peak back-EMF per coil	25.5 V

From Figure 5-10, the peak back-EMF per coil of the basic model was calculated which is equal to 12.6V. To give the required 25.5V the number of turns should be increased to 18. As a result, some key parameters of the basic model have been changed, as listed in Table 5-6. Figure 5-11 shows the new predicted back-EMF results, based on the parameter list in Table 5-6. The back-EMF results shown in Figure 5-11 are close to the required values.

Table 5-6: Updated key parameters for original model

Number of turns per slot	18
Current density	15 A/mm ²
Fill factor	0.5
Slot area	418.30 mm ²
MMF	3137
Conductor area	5.81 mm ²
I rms	87.15 A
I peak	123.2 A

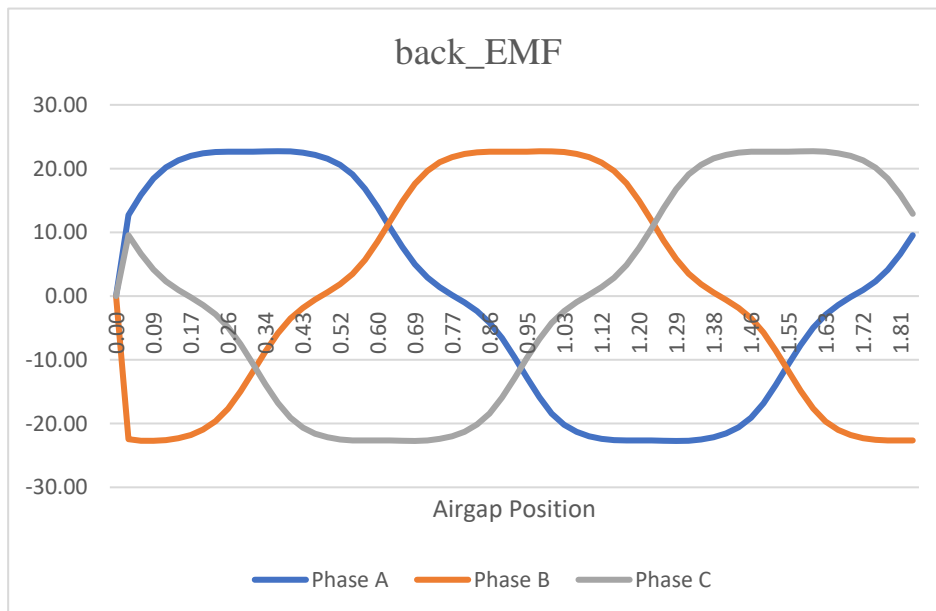


Figure 5-11: The updated back-EMF of the model (48Slots, 32Poles)

For the fault-tolerant design, one healthy lane needs to produce two-thirds of torque. According to the results in Table 5-4 and Table 5-6, the stack length needs to increase from 15.5mm to 20.7mm and the number of turns per slot needs to reduce from 18 to 13. The parameters for the fault-tolerant model are listed in Table 5-7 and the simulation results shown in Figure 5-12.

Table 5-7: Updated key parameters for fault-tolerant model

Number of turns per slot	13
Current density	15 A/mm ²
Fill factor	0.5
Slot area	418.30 mm ²
MMF	3137
Conductor area	8.06 mm ²
I rms	120.8 A
I peak	170.9 A
Torque	414 Nm

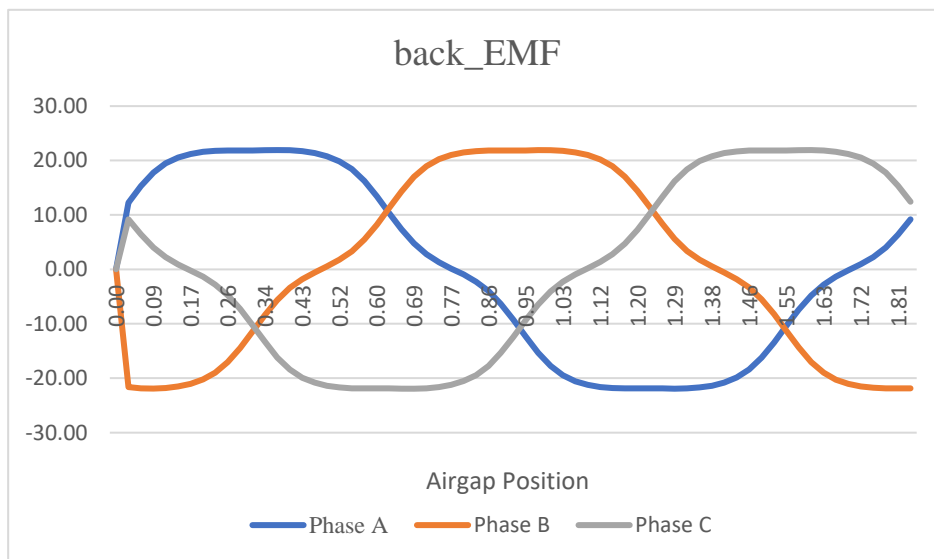


Figure 5-12: The updated back-EMF of the fault-tolerant model (48Slots, 32Poles)

5.3.3 Healthy operation simulation of the Fault Tolerant Design

The analysis above was based upon a 48 slot, 32 pole machine. However, to give greater isolation between lanes the two options of the “alternative segmented winding” of figure 5-8 and the “interspersed winding” of figure 5-9 have been introduced. In these designs a total of 48 coils has been retained, with each coil spanning 120 electrical degrees, but the number of poles has been increased from 32 to 34. This leaves 2 poles of space to be introduced between lanes. In the first case of the alternative segmented winding the two

lanes sit diametrically opposite one another, with one pole spacing between lanes. In the second case of the interspersed winding, each lane consists of two groups of coils, interspersed between the coils of the other lane. In this case the spaces between coil groups consist of one half a pole. Before calculating motor output torque, the back-EMFs of these fault tolerant models are compared in Table 5-8. The results presented in Table 5-8 shows that these models have similar peak back-EMF and peak line back-EMF.

Table 5-8: Back-EMF of two FT design model

	Alternative segmented winding	Interspersed winding
Peak back-EMF per coil	22.0 V	21.9 V
Peak line back-EMF of one set of coils	41.4 V	41.4 V

Motor output torque and torque ripple are calculated by 2D FEA which is shown in Table 5-9. According to this table, compared with the alternative segmented winding, the model with an interspersed winding design gives higher torque and lower torque ripple.

Table 5-9: Output torque and torque ripple of the model

	Torque (torque ripple)
Original model (48S32P)	310 Nm (1.0%)
alternative segmented winding	391 Nm (19.5%)
interspersed winding	402 Nm (4.4%)

5.3.4 Three phases terminal fault

Table 5-10 shows the torque of the fault tolerant model when one of the lanes is shorted at the terminals. The average torque of the model with an interspersed winding is equal to 223Nm, which is 71.9% of torque, as expected. However, the output torque of the alternative segmented design reduces to 63.2% (196 Nm).

Table 5-10: Output torque of the model

	Average torque
alternative segmented winding	196 Nm
interspersed winding	223 Nm

5.3.5 Fault current

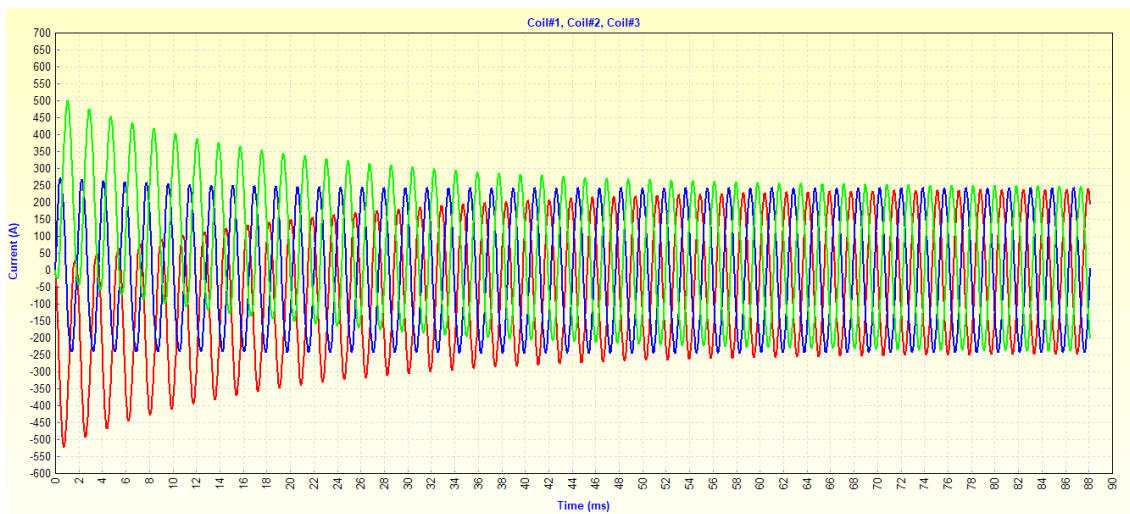


Figure 5-13: Fault current while shorted one lane at the terminal

In order to avoid thermal runaway problems, the rated value of the fault current should be calculated. Figure 5-13 shows the current with one of the lanes are shorted at the terminals. Compared with the peak rated input current of 170.9A (see Table 5-7), the fault current is about 40% higher.

The fault current is limited by the phase inductance and so the inductance needs to be increased. This can be achieved by increasing the radial depth of the slot tip. Figure 5-14 shows the model where the slot tip is equal to 5mm, and Table 5-11 shows the results with different heights of the slot tip.

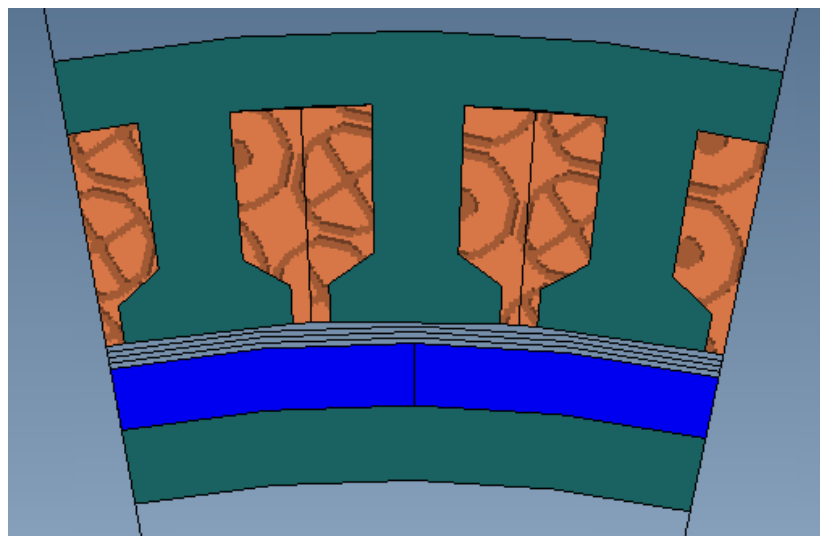


Figure 5-14: The model with 5mm height slot tip

Table 5-11: Short current with different height of slot tip

The height of slot tip	1.5mm	2mm	3mm	4mm	5mm
Peak value of short current	286 A	275 A	250 A	230 A	215 A

From Table 5-11, the results show that compared with the 1.5mm slot tip, the model with a 5mm height slot tip would reduce the shorted current by 70A. However, these results are produced from a two-dimensional finite element model, which ignores end-winding inductance. Because the stack length of the machine is short, it was thought that end-winding inductance may be large and so a 3D machine model was produced. This revealed that, with the additional effect of the end-winding, the peak value of the short-circuit current is actually only 148 A. It is clear that the short-circuit current is now less than rated current and will not give thermal problems for the motor or converter.

This section proposed two fault tolerant designs which aim to increase the reliability and safety of the motor by introducing physical spacing between lanes. Both the “interspersed winding” and “alternative segmented winding” can meet the output torque requirement in healthy operation although the alternative segmented winding has higher torque ripple. When one of the lanes is shorted, the design with an interspersed winding can produce over 70% of its unfaulted output torque, which achieves the requirements of the fault tolerant design. In comparison the alternative segmented winding only produces 63.2% of its un-faulted torque.

It is shown that the fault current which flows following a terminal short circuit can be reduced by increasing the slot opening leakage inductance. It is also shown that the end-winding inductance is relatively large and further contributes to a large synchronous inductance.

5.4 Conclusion

This chapter first shows the non-synchronous winding harmonics of a 56 pole, 48 slot motor by means of FE simulations and MatLab FFT analysis. Another motor with 48 slots and 32 poles is demonstrated to have far fewer space harmonics and is therefore preferable in terms of reducing rotor loss.

A fault tolerant design has been introduced by introducing two lanes, with spacings between lanes. Two options have been considered: one in which each lane takes up a continuous 180 degrees of arc. Termed the “alternative segmented” arrangement and one

in which each lane has two 90 degree segments placed diametrically opposite each other. This is termed the “interspersed winding” Both arrangements give the same torque during healthy conditions, but the interspersed winding arrangement is seen to be preferable because it:

- (a) Has lower torque ripple
- (b) Give greater torque during faulted operation
- (c) Will not give rise to unbalanced magnetic pull during faulted operation.

Chapter 6 Thermal analysis

6.1 Introduction

Due to space and weight constraints, motors used in helicopter ETR systems must be of high energy density and torque density, which results in high input current densities. These high input current densities result in very steep temperature rises in the stator winding, which reduces the service life of the motor insulation and brings the risk of demagnetising the PMs. To avoid the risk of overheating, a cooling design for the stator winding is essential.

This chapter begins with a brief description of several methods of thermal analysis and proposes a benchmark design. The initial temperature rise of the winding after simple cooling is then obtained by CFD simulation, followed by the addition of forced air cooling and the optimisation of some key parameters, such as the shape and size of the cooling channels and air turbulence to improve the cooling performance. Finally, a new hybrid cooling solution is proposed and compared.

6.2 Thermal analysis approaches

Motor thermal management is an important part of the motor design process, which allows the temperature distribution of the motor to be predicted by thermal analysis methods. Common thermal analysis methods include lumped parameter thermal networks (LPTN), FEA, and CFD.

The LPTN analysis provides a method for quickly determining the internal temperature distribution of a motor, allowing the variation caused by different input parameters to be quickly determined. LPTN models are often made up of different components and simplified to represent more complex geometries. The LPTN resembles a circuit network in which voltage represents temperature, current represents heat flow, and resistance and capacitance represent thermal resistance and capacitance, respectively [92]. The LPTN model then predicts the steady-state or transient heat flow within the motor as well as the temperature of each component. The more detailed the network, the more accurately the temperatures in different areas within the machine can be determined. However, one disadvantage of the LPTN approach to thermal analysis is that it involves a lot of work to create an accurate model, which is highly time-consuming.

FEA involves dividing the components in a model into many tiny mesh nodes and elements to analyse the variation in these dimensions. Processing time, however, is a disadvantage of FEA. FEA thermal analysis has advantages only when the geometry becomes too complex to use the LPTN model.

Compared to the LPTN and FEA methods, CFD is often the most accurate method of temperature prediction. It can be used to determine input heat transfer boundaries and can perform simulations to predict fluid flow characteristics and optimise cooling methods such as air cooling.

6.3 Benchmark design and software setting

The optimisation is performed on a fault-tolerant PM synchronous machine designed to power an electric tail rotor on a helicopter, which was presented in previous chapters. The motor has 48 slots and 34 poles with surface-mounted permanent magnets, and concentrated windings are used in a double-layer winding arrangement. Table 6-1 presents several key parameters of the proposed motor. The cross-section of the complete motor is shown in Figure 6-1, while Figure 6-2 illustrates a twenty-fourth CAD model for thermal simulation.

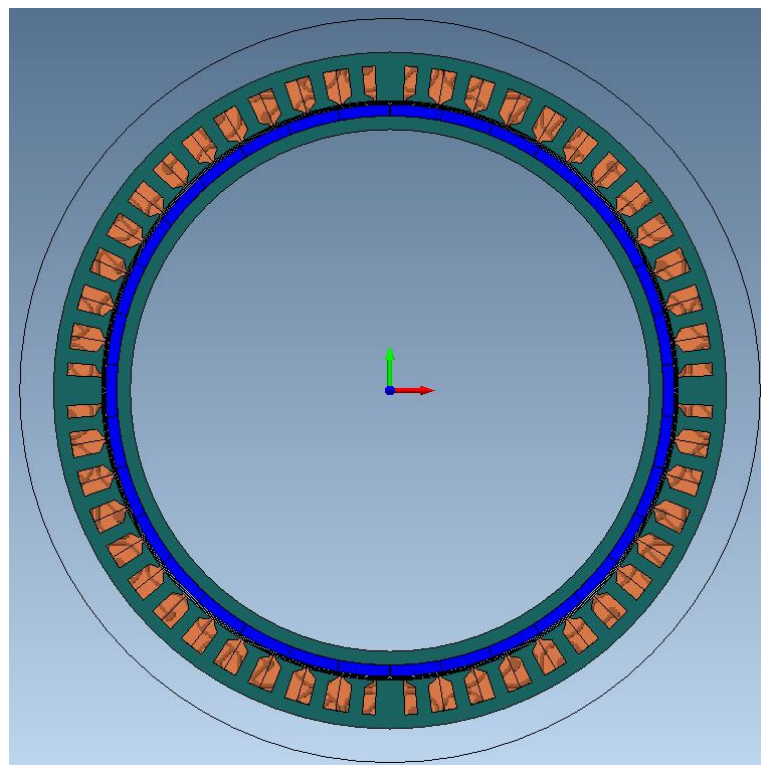


Figure 6-1: A 2D cross-section of the machine

Table 6-1: Key parameters of the proposed motor

Rated Power	65 kW
Outer Stator Diameter	490 mm
Inner Stator Diameter	420 mm
Outer Rotor Diameter	416 mm
Inner Rotor Diameter	380 mm
Stator Length	20.7 mm
N. Poles	32
N. Stator Slots	48
Slot Area	394 mm ²
Coil Turns/Slot	104
Copper Wire OD	1.13 mm
Enamel Thickness	0.025 mm
Air Gap	2 mm
Current Density	15 A/mm ²

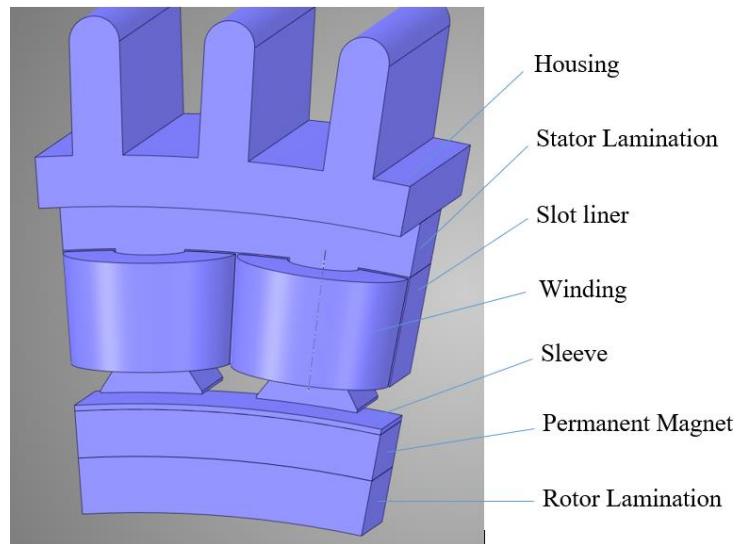


Figure 6-2: The segment used for CFD thermal simulation

As shown in Figure 6-2, the fin, rotor, and slot liner have been added to the simulation to provide a more realistic simulation of the heat dissipation in the stator winding of the motor. Based on the choice of materials used in the previous motor design, Table 6-2 shows the properties of these materials, including their thermal conductivity, mass, volume, and loss density, which are used for thermal simulation. Regarding the winding section, only the properties of copper are listed in the table; in reality, there is enamel on the outside of the copper wire, and drawing each copper wire separately when building the simulation model would considerably increase the complexity of the model and the simulation time. As can be seen from Figure 6-2, an equivalent coil module according to actual size has been selected to replace the copper wire. Consequently, the copper and

enamelled wire should be placed together when calculating the thermal conductivity of the winding.

Table 6-2: Properties of materials

	Thermal conductivity (W/(m. °C))	Volume (m³)	Loss Density (W/m³)	Specific Heat Capacity (J/(kg. °C))	Mass Density (kg/m³)
Rotor Lamination (Vacoflux 48)	30	3.10×10 ⁻⁴	1.35×10 ⁵	372	8120
Permanent Magnet (N42SH)	7.6	3.05×10 ⁻⁴	1.03×10 ⁷	460	7500
Sleeve (Non-magnetic)	0.026	3.78×10 ⁻⁵	0	1005.6	1000
Stator Lamination (Vacoflux 48)	30	8.84×10 ⁻⁴	5.77×10 ⁵	372	8120
Slot liner	0.139	1.99×10 ⁻⁵	0	2310	960
Winding in slots (Copper:98% IACS)	386	4.69×10 ⁻⁴	4.27×10 ⁶	393.5	8940

The fact that each copper wire cannot be wound perfectly together results in air or impregnation insulation in the equivalent coil module. The simplest approximation of the equivalent thermal conductivity of a composite material is applied to the series and parallel models of the two materials, i.e. (6-1) and (6-2), and is derived from the theory of equivalent thermal resistance [143].

$$k_e = \frac{k_1 k_2}{v_1 k_2 + v_2 k_1} \quad (6 - 1)$$

$$k_e = v_1 k_1 + v_2 k_2 \quad (6 - 2)$$

where k_e , k_1 and k_2 are the equivalent thermal conductivity and the thermal conductivity of each material, and v_1 and v_2 are the volume ratio of each material, with $v_1 + v_2 = 1$.

However, an accurate result cannot be obtained for a stacked cylinder such as a coil. To obtain a more accurate equivalent thermal conductivity, formula 6-3 was derived by Hashin and Shtrikman, which is more applicable to windings [144].

$$k_e = k_i \frac{(1+v_c)k_c + (1-v_c)k_i}{(1-v_c)k_c + (1+v_c)k_i} \quad (6 - 3)$$

where v_c is the volume ratio of the conductors, v_i is the volume ratio of the insulation materials, and k_c and k_i represent the thermal conductivity of conductor and insulator materials, respectively. Notably, this formula only applies to two materials laminated together.

To include three materials, by assuming that the impregnation insulation and the conductor insulation can be combined into one material and can be represented by a parallel model, the thermal conductivity of the equivalent insulation is calculated according to formula 6-4 [143].

$$k_a = k_{ii} \frac{v_{ii}}{v_{ii}+v_{ci}} + k_{ci} \frac{v_{ci}}{v_{ii}+v_{ci}} \quad (6 - 4)$$

where k_a is the equivalent thermal conductivity of the insulation, v_{ii} and v_{ci} represent the volume ratio of the impregnation insulation and the conductor insulation, respectively, and $v_{ii} + v_{ci} \neq 1$. The equivalent anisotropic thermal conductivity is calculated according to Equations 6-2, 6-3 and 6-4, and is shown in Table 6-3.

Table 6-3: Equivalent thermal conductivity of winding

CFF	(k_x, k_y, k_z)	(k_r, k_t, k_z)
63.5%	(1.5, 1.5, 216.3)	(1.5, 216.3, 1.5)

The coil fill factor (CFF) indicates the proportion of copper wire in the equivalent winding module. Cartesian coordinates and a local cylindrical coordinate system is used to estimate the equivalent anisotropic thermal conductivities (k_x, k_y, k_z) and (k_r, k_t, k_z) respectively [8], where the subscripts x, y, z represents the directions in the x, y, z axis of the middle-winding, and the subscripts r, t, z represents the radial, tangential and axial directions of the end-winding.

Figure 6-3 shows the computational domain for the thermal simulation. Periodic boundary conditions are used to reduce the computational cost. The external domain is used for simulating air cooling on the stator casing and the internal domain is used for simulating air cooling inside the motor. The motor rotor does not rotate, only the temperature distribution of the motor stator at rest is considered. The mesh details are presented in Figure 6-4.

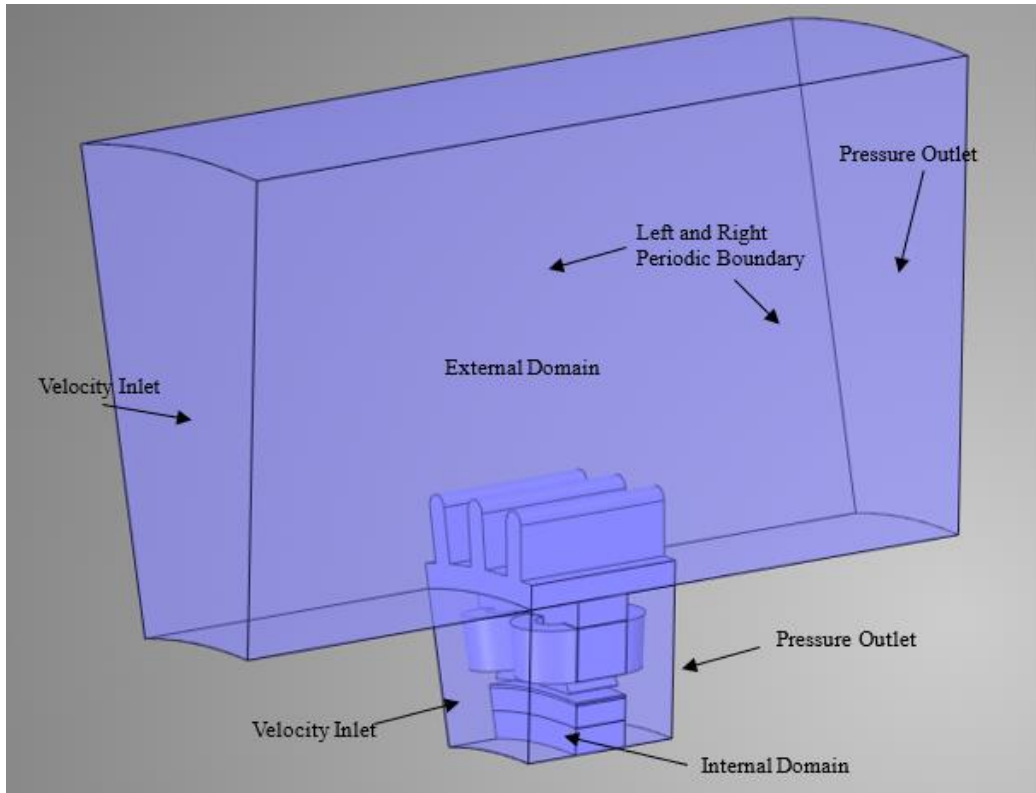


Figure 6-3: The computational domain in upstream view

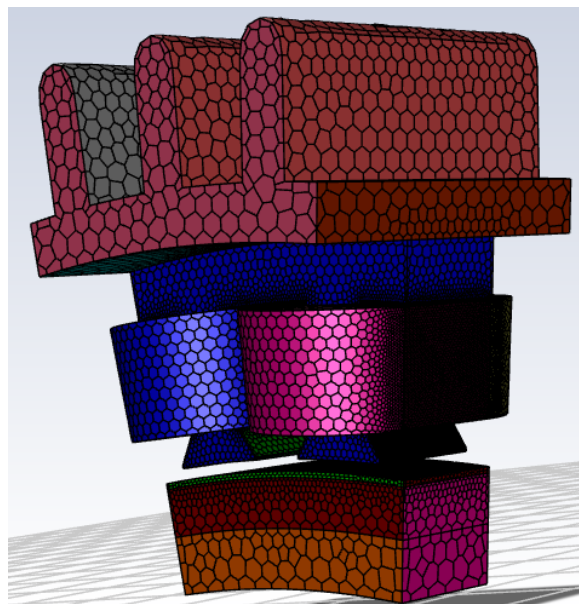


Figure 6-4: Mesh details in upstream view

Also, due to the harsh environment in which the motor operates, the ambient temperature of this simulation and the temperature of the input air flow are both set to 323K as shown in Figure 6-5, which corresponds to 50 degrees Celsius.

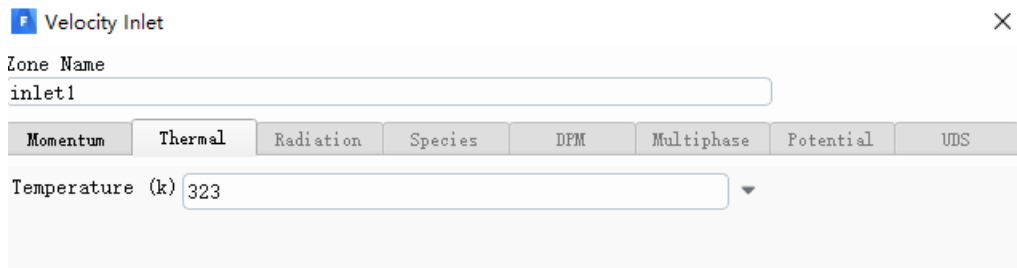
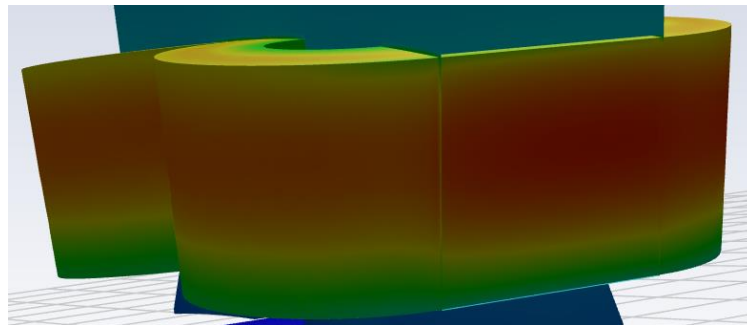
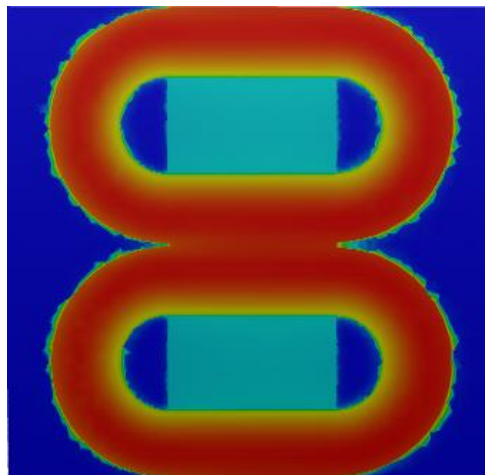


Figure 6-5: Input air flow temperature



(a)



(b)

Figure 6-6: (a) Temperature distribution in the 3D stator at an air speed of 10 m/s. (b) Temperature distribution in a 2D cross-section through the winding at an air speed of 10 m/s. The flow direction is left to right.

The main losses of the stator include 510W of iron loss and 2837W of winding loss. The cooling performance of the benchmark design was estimated by CFD simulations, as shown in Figure 6-6. The air-flow velocity and air-turbulence intensity are set to 10 m/s

and 0.5%, respectively. The air flows over both the inner radius of the coil and over the cooling fins on the stator housing.

The simulation results show that the maximum temperature rise in the winding is 115 K, corresponding to a hotspot of 165 degrees Celsius. The contours illustrate that the hot spots are in the centre of the winding. Because the air flow is restricted to the air gap between the rotor and stator, there is relatively poor heat transfer owing to the limited contact area between the air flow and the winding. In Figure 6-6, the air temperature at the winding inlet on the left appears to resemble that at the winding outlet on the right. While a rise of 7 degrees is calculated, the rise is not obvious, due to the range of the shaded graph over 100 degrees.

The high-temperature rise in the stator winding is due to the following causes:

- The slot liner prevents the majority of conduction heat transfer from the winding to the stator due to its low thermal conductivity.
- The conductivity of the winding in the radial direction is more than 200 times lower than that in the axial direction of the conductor. Thus, it is more difficult to transfer heat from the centre of the winding to the surface.
- The velocity vector of the airflow shown in Figure 6-7 demonstrates that the air channel through the stator is restricted to the rotor-stator air gap. This causes insufficient contact area between the airflow and the main heat source, resulting in poor heat transfer at the winding surfaces.

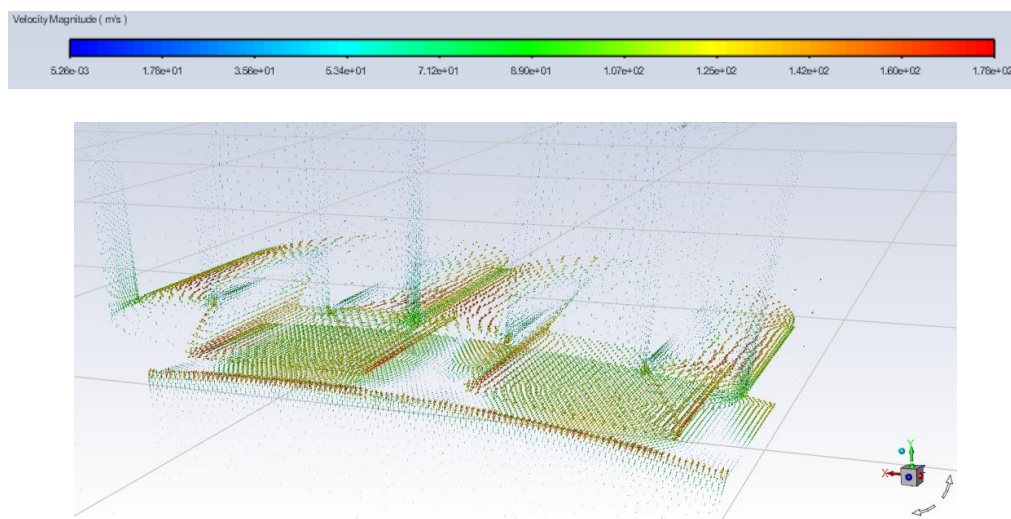


Figure 6-7: The velocity vector of the air flow in the 3D stator with an input airspeed of 10 m/s

6.4 Air cooling optimization

The model has been optimised based on the simulation results of the baseline design, by introducing air channels, modifying the width of the air channels, and comparing different shapes of the air channels.

6.4.1 Air flow velocity

First, a 0.5 mm-wide air channel was introduced between two windings, as shown in Figure 6-8. To compare the temperature rise at the same loss, due to the addition of air channels, the volume of the equivalent coil module for this model has been reduced, which results in an increase in CFF, loss density, and thermal conductivity of the equivalent coil, as shown in Table 6-4 for comparison of the specific values. For the compressed winding, the volume of coil module is reduced, but the volume of the coil is constant, which cause the CFF increases.

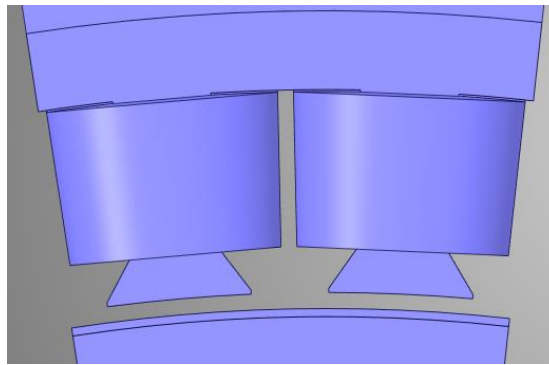


Figure 6-8: The CAD model with a 0.5 mm air channel between windings.

Table 6-4: Comparison of model parameters with and without air channels

Width of air channel	0 mm	0.5 mm
Loss density	$4.15 \times 10^6 \text{ W/m}^3$	$4.27 \times 10^6 \text{ W/m}^3$
CFF	63.5%	65.5%
(k_x, k_y, k_z)	(1.5, 1.5, 216.3)	(1.6, 1.6, 231.2)
(k_r, k_t, k_z)	(1.5, 216.3, 1.5)	(1.6, 231.2, 1.6)

Figure 6-9 shows the temperature distribution in a 2D cross-section of the winding. For ease of comparison, the 2D cross-section and temperature distribution legends were chosen to be the same as those of the benchmark design. Both simulations also have the same input airspeed and air turbulence intensity. A comparison of Figure 6-9 with Figure 6-6 shows that the maximum temperature rise at the hot spot has been reduced considerably, from 115 to 77 K. This is because the contact area between the cooling air

and the windings has been greatly increased with the addition of the air channel, which results in more heat being carried away by air.

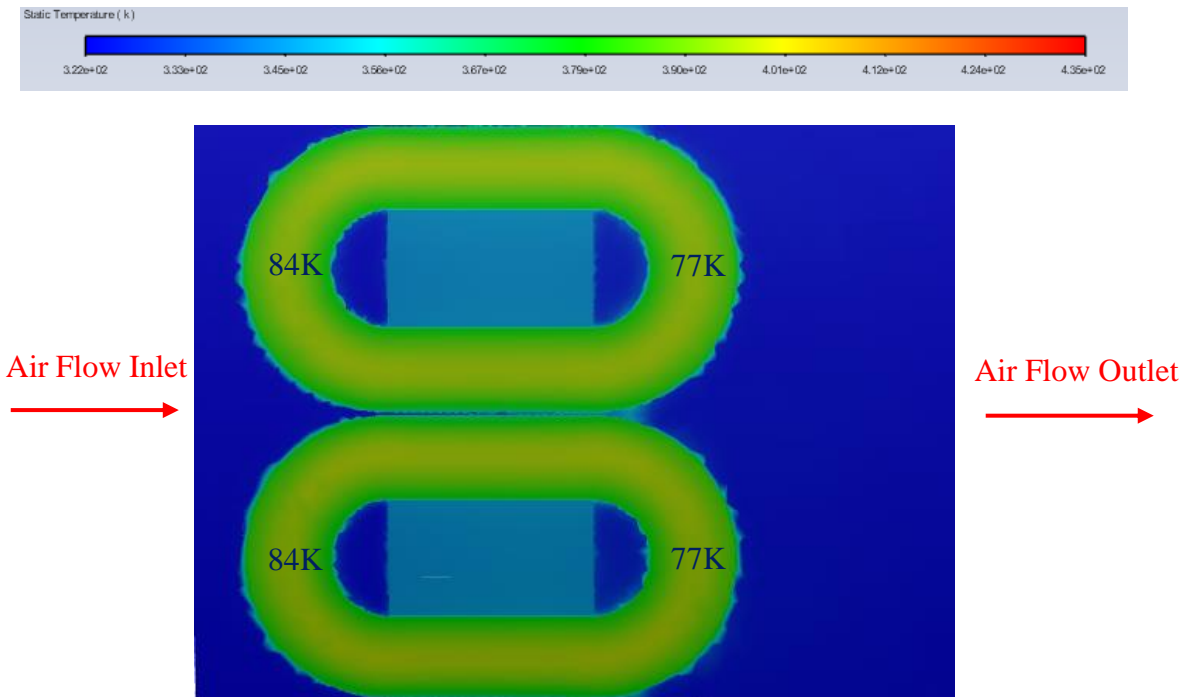


Figure 6-9: Temperature distribution in a 2D cross-section of the winding at an input airspeed of 10 m/s. The flow direction is left to right.

Because the velocity of the air is one of the main influencing factors in air cooling, the effect of airflow velocity on the cooling effect was investigated. Based on the model with a 0.5-mm air channel between two windings, the airflow velocity ranging from 10 to 100 m/s is applied in the following simulation to calculate the trend of the temperature decrease. In this case, the air turbulence intensity is set to 0.5%, which reflect laminar flow.

Figure 6-10 shows the temperature distribution in a 2D cross-section of the winding for airflow velocities of 10, 20, 30 and 40 m/s. In Figure 6-10(a), at an airflow velocity of 10 m/s, a maximum temperature of 400 K is observed at the hot spot, which corresponds to a temperature rise of 77 K relative to the ambient temperature. As the airflow velocity increases to 20 m/s, the maximum temperature drops to 386 K and continues to decrease as the airflow velocity continues to increase. When the air velocity reaches 30 and 40 m/s, the maximum temperature drops to 379 and 375 K, respectively. Additionally, in all four figures, the temperature rise at the end winding surface on the upwind side will be somewhat lower than the temperature rise at the end winding surface on the downwind

side, but this is not obvious due to the resolution of the figure legend. Furthermore, the difference between the maximum temperatures at these two ends decreases as the airflow velocity increases.

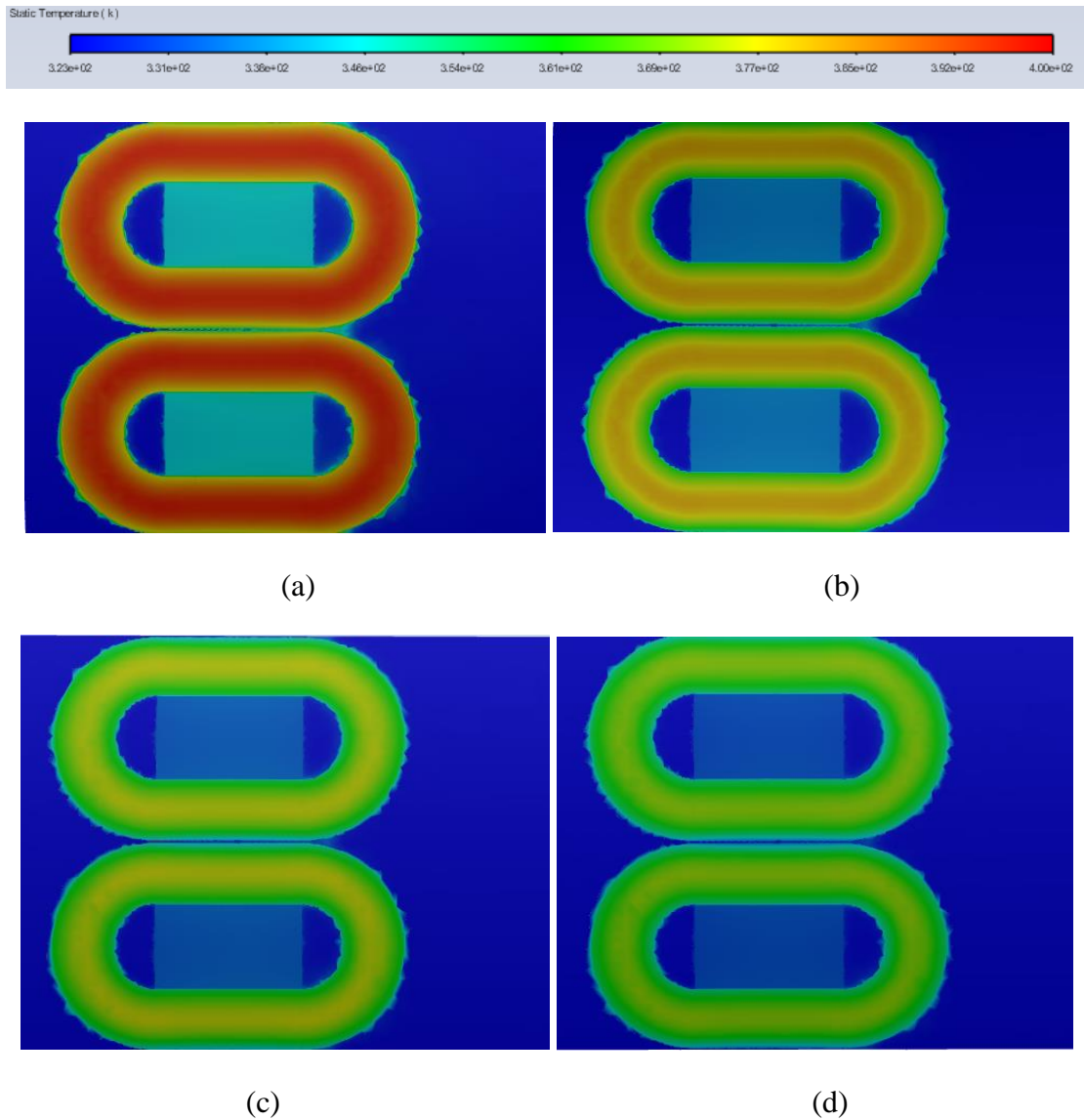


Figure 6-10: Temperature distribution in a 2D cross-section through the winding at an airspeed of (a) 10 m/s, (b) 20 m/s, (c) 30 m/s, and (d) 40 m/s. The flow direction is left to right.

Figure 6-11 shows the maximum temperature rise of the winding as the input airspeed rises. From the graph, the temperature rise decreases as the airflow rate increases.

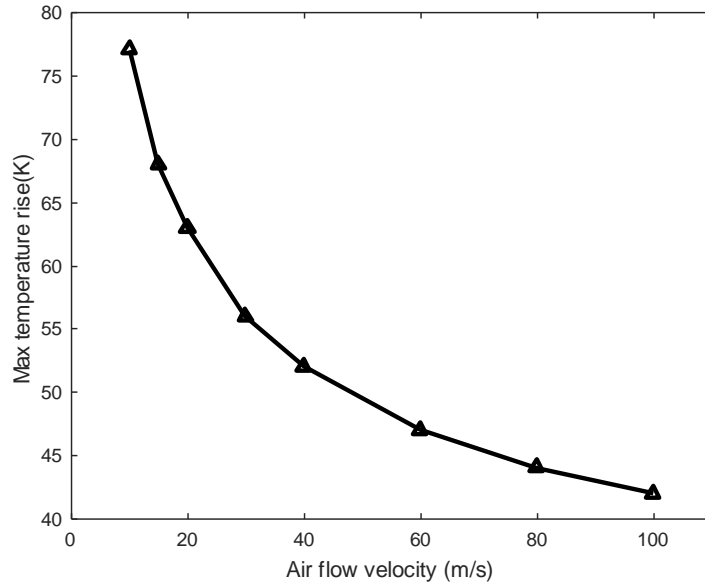


Figure 6-11: Maximum temperature rise when the input airspeed increases from 10 to 100 m/s.

6.4.2 Width of the air channel

After investigating the effect of airflow velocity on winding temperature, the width of the air channel was investigated. Previous research [145]–[147] has studied the relationship between the cooling performance of the winding and the winding compression across its width, with a gap between adjacent coils. Compression of the winding creates greater thermal conductivity because of a higher packing factor, but it also introduces an additional cooling channel. This can cause a reduction in the temperature rise of up to 40%, primarily because there is a greater contact area between the air and coils. Table 6-5 shows the variation of some key parameters when increasing the width of the air channels while maintaining the same winding losses.

Table 6-5: The change of key winding parameters while increasing the width of the air channel

Width of air channel	Loss density	CFF	(k_x, k_y, k_z)	(k_r, k_t, k_z)
0.5 mm	$4.27 \times 10^6 \text{ W/m}^3$	65.5%	(1.6, 1.6, 231.2)	(1.6, 231.2, 1.6)
1.0 mm	$4.40 \times 10^6 \text{ W/m}^3$	67.5%	(1.7, 1.7, 238.3)	(1.7, 238.3, 1.7)
1.5 mm	$4.54 \times 10^6 \text{ W/m}^3$	69.6%	(1.8, 1.8, 245.7)	(1.8, 245.7, 1.8)
2.0 mm	$4.68 \times 10^6 \text{ W/m}^3$	71.9%	(2.0, 2.0, 253.7)	(2.0, 253.7, 2.0)
2.5 mm	$4.84 \times 10^6 \text{ W/m}^3$	74.3%	(2.1, 2.1, 262.2)	(2.1, 262.2, 2.1)
3.0 mm	$5.01 \times 10^6 \text{ W/m}^3$	76.9%	(2.3, 2.3, 271.3)	(2.3, 271.3, 2.3)

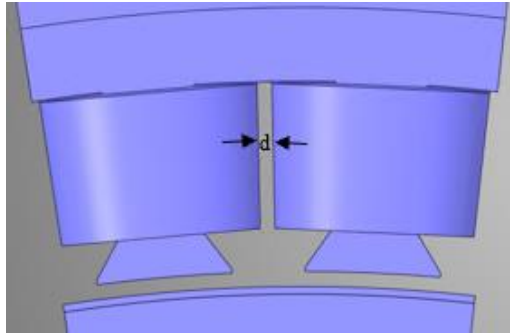


Figure 6-12: Definition of the width of the air channel, d , between windings.

Figure 6-12 shows the definition of the width of the air channel, d , between the windings. Figure 6-13 shows the variation in the maximum temperature of the windings as the input airspeed is increased with different widths of the air channel. When the airspeed is equal to or greater than 20 m/s, the temperature at the hot spot generally decreases as the air channel width increases. This is because the thickness of the boundary layer is reduced at higher airspeeds, and peak temperatures will generally increase slightly with smaller air channel widths.

However, with an airspeed of 10 m/s, the peak temperature of the hot spot is predicted to initially rise as the gap increases to 1.5 mm. This may be inferred from the boundary layer flow interaction that occurs between windings. With gaps of less than 1.5mm the boundary layer is not fully formed, there is more mixing of the air, and the heat transfer coefficient is higher. Conversely, with gaps of more than 1.5 mm, the high turbulent air currents disturb the boundary layer and also increase the heat transfer from the surface boundary layers.

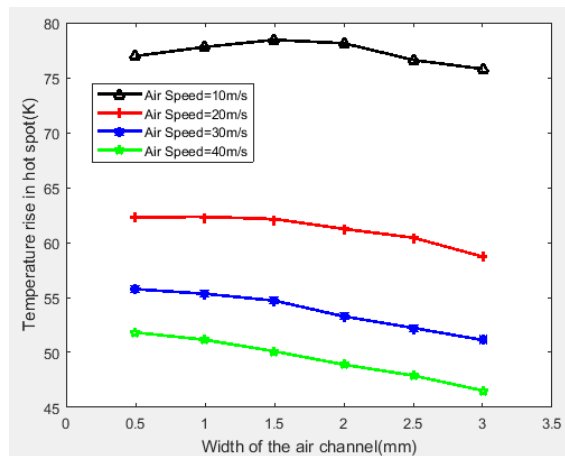


Figure 6-13: Maximum temperature rise variation as the width of the air channel increases from 0.5 to 3 mm with different input airspeeds.

6.4.3 Shape of the air channel

For simplicity, the air channel is generally modelled as rectangular, as shown in Figure 6-14 (a). However, in reality, the shape is tapered due to the angle between windings, as illustrated in Figure 6-14 (b). When comparing the two different shapes of the air channels, 2 mm is selected as the width of the rectangular air channel, and the simulation maintains the same air channel volume and the same winding losses for the tapered air channel.

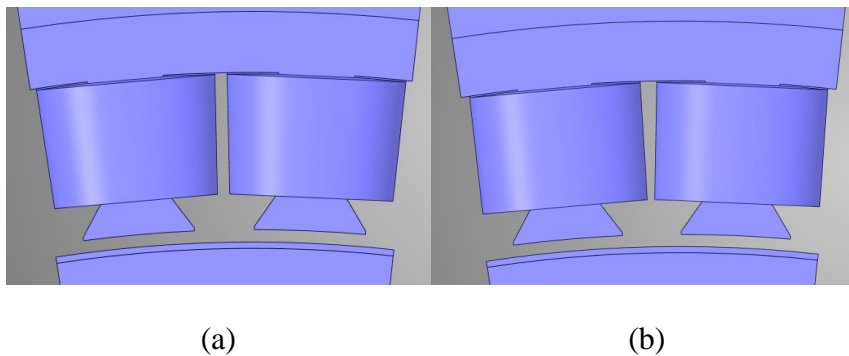
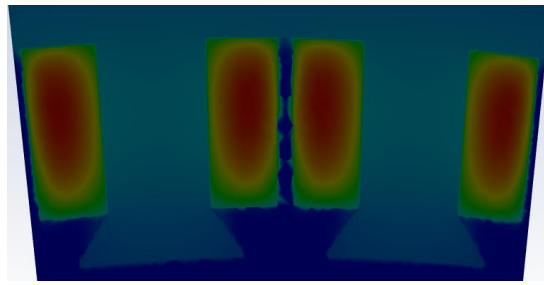
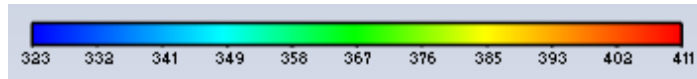


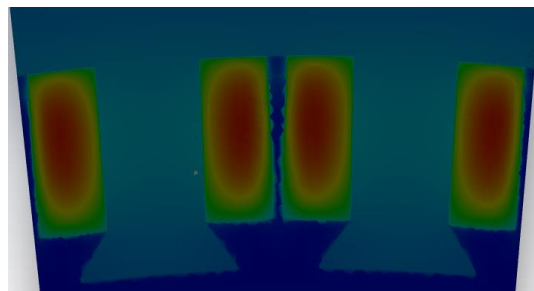
Figure 6-14: (a) The rectangular channel. (b) The tapered air channel.

Figure 6-15 presents simulation results for these two models which had the same air channel volume at an air speed of 10 m/s. The tapered model had an approximately 2% lower temperature rise at the hot spot. This is likely to be because the channel was wider near the core back, leading to increased cooling near the hotspot.

Figure 6-16 shows the trend of maximum temperature rise with air flow rate for different shaped air channels. As is clear from the diagram, the two different shaped air channels have a similar cooling effect on the windings at air velocities below 20 m/s. However, when the air velocity is greater than 30 m/s, the rectangular channel has a better cooling performance, with a 10% improvement compared to the tapered channel. Despite this, the difference between the models is sufficiently small to show that the rectangular approximation is valid at air velocities below 20 m/s.



(a)



(b)

Figure 6-15: (a) Temperature distribution of the model with a rectangular air channel in a 2D cross-section contour at an air speed of 10 m/s (b) Temperature distribution of the model with a triangular air channel in a 2D cross-section contour at an air speed of 10 m/s

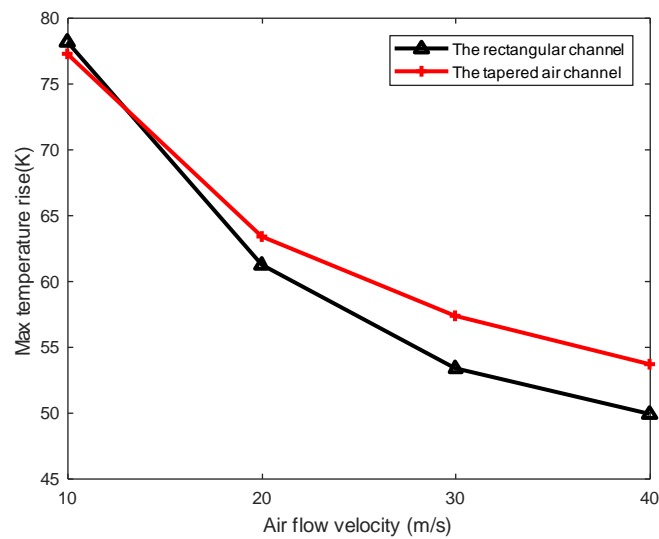


Figure 6-16: Maximum temperature rise for different shaped air channels as a function of air flow rate

6.5 The influence of air turbulence intensity

Air turbulence intensity is defined as the ratio of the standard deviation of the fluctuating wind speed to the mean wind speed. It indicates the intensity of wind speed fluctuations. Previous studies [145]–[147] have shown that the heat transfer coefficient increases alongside the intensity of turbulence, improving the cooling performance of the windings.

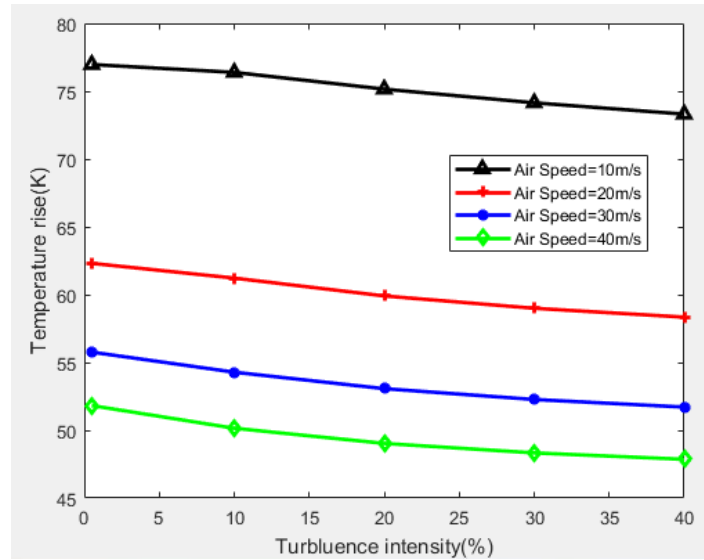


Figure 6-17: The maximum temperature rise variation as air turbulence intensity increase from 0.5% to 40% with different air flow velocity

The maximum temperature rise of the model with an air channel width of 0.5mm was affected by air turbulence intensity and is presented in Figure 6-17. Clearly, an increase in turbulence intensity enhanced the cooling effect of air cooling, regardless of the air velocity's magnitude. This is because as the turbulence intensity increased, further boundary layers were broken down. This means that the air was more mixed, and the thermal conductivity was increased.

Figure 6-18 shows the percentage reduction in temperature rise when the turbulence level was increased from 0.5% to 40%. This was achieved by introducing features upwind of the machine. The figure shows the effect of the change in turbulence as the air-channel width was increased, with different curves for each air speed. Importantly, increased turbulence had a much greater effect when the channel width was large, and the air velocity was high. Increased turbulence never created more than an 8% effect when the channel was less than 1.0mm wide. However, for a channel width of 3.0mm, the effect was more than 10%, providing the air velocity was 20m/s or greater. This is because the

thickness of the boundary layer decreased as air flow velocity increased. A higher air turbulence intensity also severely disturbed the boundary layer, increased the heat transfer coefficient and allowed increased heat to be removed from the windings. This overall effect was smaller than anticipated, but still provided a useful contribution to reducing the temperature rise.

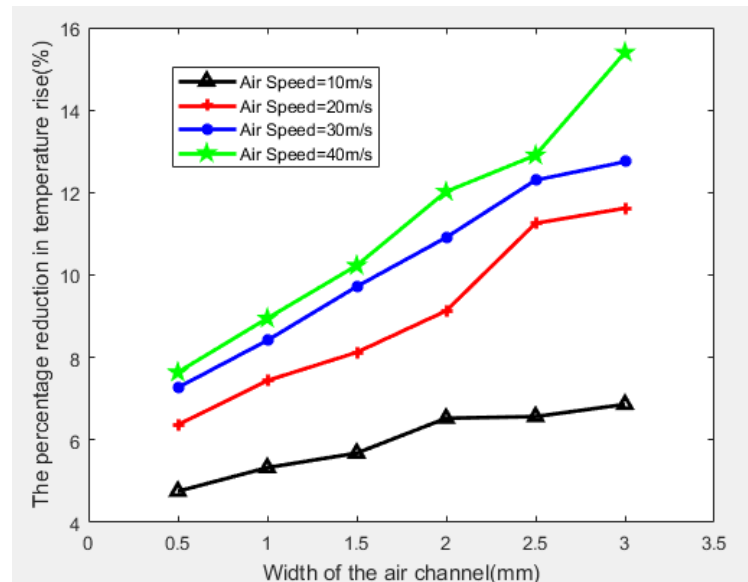


Figure 6-18: The percentage reduction in temperature rise when the air turbulence intensity is increased from 0.5% to 40%

6.6 Hybrid cooling

The previous sub-section showed that the maximum temperature of the winding was greatly reduced by increasing the width of the air channel. It was also reduced by increasing the air velocity and the intensity of the air turbulence. In practice, however, excessive air velocity or air turbulence intensity is challenging to achieve. This means that there is a significant amount of heat that is difficult to transfer from the centre of the winding to the surface. This is due to the high thermal resistance, which means that the air cooling cannot carry more heat that is generated from windings. The most direct and effective solution for removing heat from the central core of the winding is liquid cooling. A copper pipe is implanted through the hot spots of the winding, as presented in Figure 6-19. Water is selected as the coolant due to the low cost and the ideal operating temperature.

6.6.1 Model design

A new hybrid cooling design has been proposed and is shown in Figure 6-19. This design only buries the copper pipe in the middle winding; the connection on the upwind side is exposed to the air and not buried in the end winding. This is because the exposed pipes also benefit from the air cooling effect, allowing for better cooling of the windings. The pipes in each winding are connected in parallel, which allows each winding to have the same liquid cooling effect. A 0.5mm air channel width was chosen because it leads to a 34% improvement in air cooling compared to no air channel. Simultaneously, the stator slot will become more crowded due to the addition of the pipe. 2mm OD and 3mm OD pipes were chosen for comparison because of the space available in the stator slot. The wall thickness of each pipe was 1mm, which means that the inner diameters of the two pipes were 1mm and 2mm respectively. Table 6-6 shows the model parameters for the different pipe sizes, while maintaining the same winding losses. Figure 6-20 shows the mesh details of the hybrid cooling design in a downstream view.

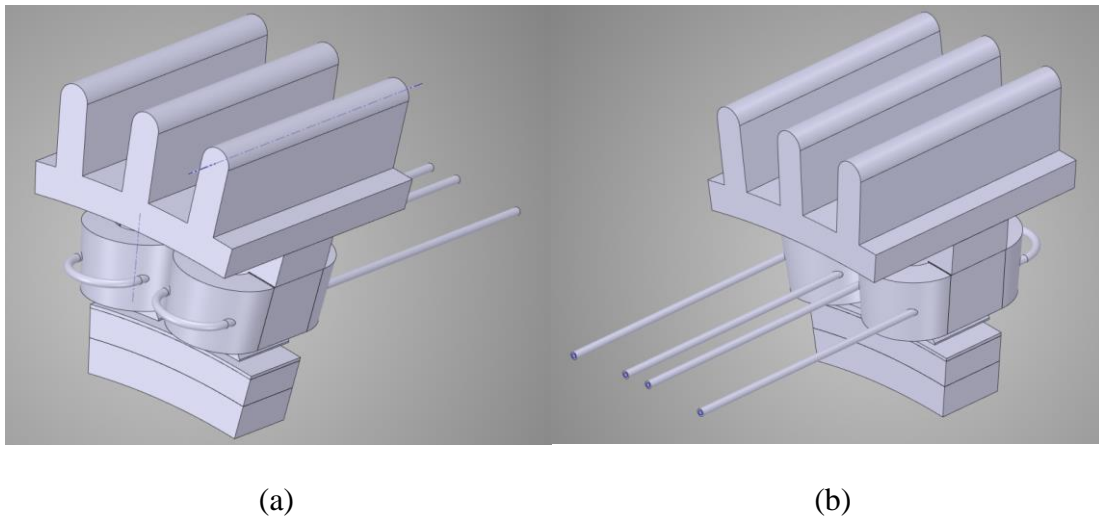


Figure 6-19: (a) The CAD model of the hybrid cooling design in (a) upstream view (b) downstream view

Table 6-6: Comparison of model parameters with different size pipe

Pipe OD	2 mm	3 mm
Loss density	$4.35 \times 10^6 \text{ W/m}^3$	$4.46 \times 10^6 \text{ W/m}^3$
(k_x, k_y, k_z)	(1.70, 1.70, 235.8)	(1.78, 1.78, 241.7)
(k_r, k_t, k_z)	(1.70, 235.8, 1.70)	(1.78, 241.7, 1.78)

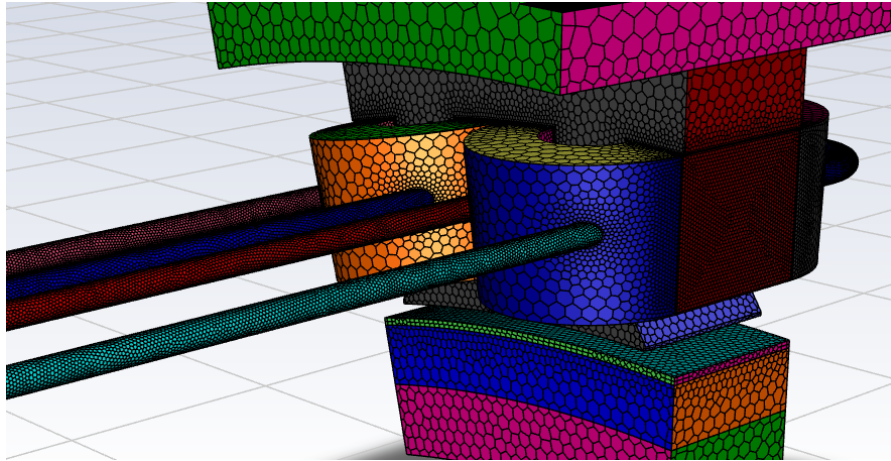


Figure 6-20: The mesh details of the hybrid cooling design in downstream view

6.6.2 CFD simulation results

Table 6-7 compares the temperature rise of the pure air-cooled and hybrid-cooled models for the same air speed and air turbulence intensity. Furthermore, in the model with hybrid cooling, there was no liquid in the pipes. By comparing the results, it is clear that the new hybrid cooling design improved the cooling effect to a certain extent when only the cooling airflow was introduced. This is due to the high thermal conductivity of the tube and the fact that it was buried in the middle of the winding, which allows more heat to be removed by thermal conduction.

Table 6-7: Temperature rises in hot spot for the two models

Model type	Temperature rises in hot spot (Kelvin)
Air cooling only	77
Hybrid cooling design (3mm pipe OD)	69

The effect of different water velocities on its heat dissipation was considered with a fixed air speed of 10 m/s, as shown in Figure 6-21. Water was selected as the coolant due to its low cost and ideal working temperature. Water could be replaced by other coolants if required. As the diagram shows, the overall cooling effect increased with increasing water flow velocity size, regardless of the tube's diameter. Additionally, the cooling effect of models with larger OD tubes was further improved. When the water velocity increased from 0.1 to 2m/s, the models with 2mm and 3mm tubes reduced the temperature rise of the hot spots by 8.6 K and 8.4 K, respectively. Simultaneously, the model with the 3mm OD tube maintained a reduced maximum temperature rise of around 3.5K compared to the other model, regardless of water velocity. Since a larger outside diameter pipe

creates a larger contact area and a higher flow rate, more heat can be removed from the winding.

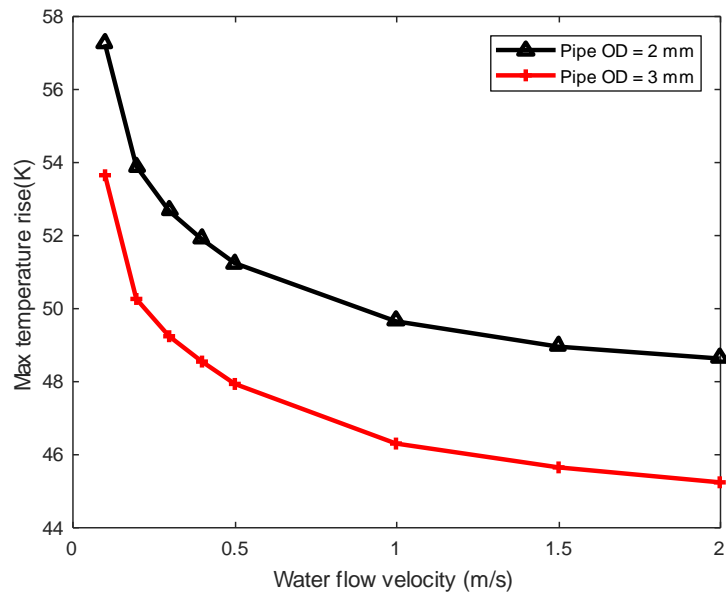


Figure 6-21: The influence of water flow speed upon hotspot temperature rise

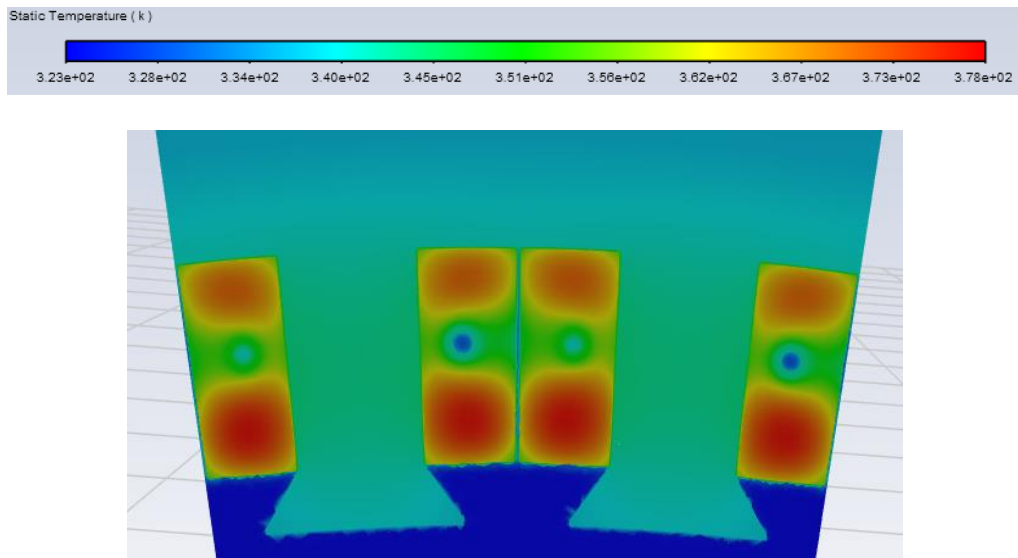


Figure 6-22: The cross-section of the model with a 3mm OD pipe at a water speed of 0.1m/s

Figure 6-22 shows the temperature distribution for a cross section of a model with a 3mm OD tube. It shows that after the centre of the winding was inserted into the tube, the position of the hot spot of the winding changed, moving above and below the tube.

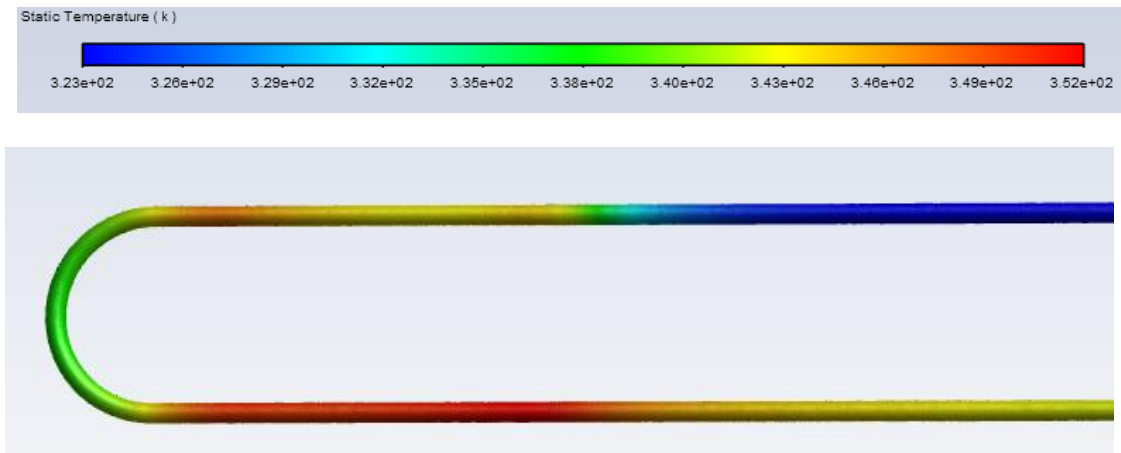


Figure 6-23: The temperature of the liquid inside the pipe of the model with a 3 mm OD pipe at a water speed of 0.1 m/s

Figure 6-23 shows the temperature distribution of the water in the water pipe. The temperature distribution demonstrates that the previous design conjecture was correct. The water flow took some of the heat out of the winding when it first flowed through it. Following this, the continuous air cooling also removed around 40% of the heat from the water flow through the copper tube when it reached the section of the tube that was exposed to the air. After this, the water flowed through the winding a second time and was cooled. This design allows for an optimal cooling performance.

6.7 Conclusion

In this chapter, the maximum temperature of the stator winding of a benchmark design was obtained using a CFD simulation based on the motor designed in the previous chapter. The effect on air cooling on this motor was then assessed by introducing air channels and studying the size and shape of the air channels, the magnitude of the air flow velocity and the intensity of the air turbulence. A new hybrid cooling design was proposed. It was studied regarding water flow velocity and pipe size and compared to a model with air cooling only. The following chapter will present experiments that verify the results of this CFD simulation.

Chapter 7: Prototype manufacturing and thermal experiment

7.1 Introduction

The previous chapters provided a detailed description of the motor design and the optimisation of the designed motor by including fault tolerance. This chapter presents a thermal simulation of the designed motor using CFD and proposes a corresponding design for hybrid cooling.

Based on the proposed design, a prototype design, wherein only a part of the stator was manufactured, is used to compare different cooling systems. The cooling systems considered herein are air and hybrid cooling systems. To obtain more accurate air cooling results, the experiments are performed in a wind tunnel to simulate suitable blowing effects.

7.2 Experimental preparation

The preparatory work includes the manufacturing of the test model, the fabrication and assembly of the other components, and the test process. To simulate a realistic motor model, the entire manufacturing process of the test models is discussed in section 7.2.1.

7.2.1 Test model for air cooling

The test model for air cooling comprises three steel stator tooth units and winding blocks, as shown in Figure 7-1. The middle unit is used to evaluate the temperature rise when the winding has an equivalent AC loss. The units on either side of this unit are also energised to ensure that the middle unit is in the same environment as it would be in the actual motor.

Two sets of models were built – one with a hand-wound set of coils and the other with a machine-wound set, as shown in Figure 7-2. The difference between these two sets is that the packing factor of the machine-wound coils is higher than that of the hand-wound coils. To protect the insulation of the coil from damage, the slot liner was replaced by a 3D printed cover, as shown in Figure 7-3; however, this cover is twice as thick as the slot liner.

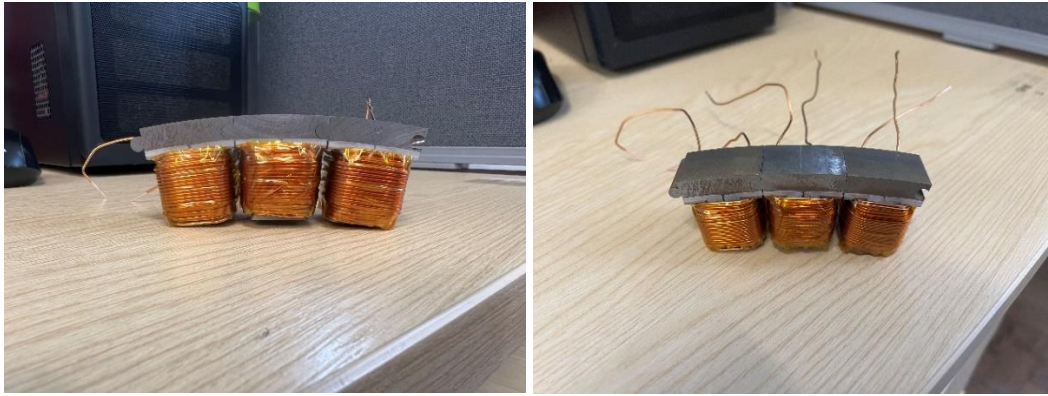


Figure 7-1: Test stator tooth units and winding blocks



Figure 7-2: Winding machine

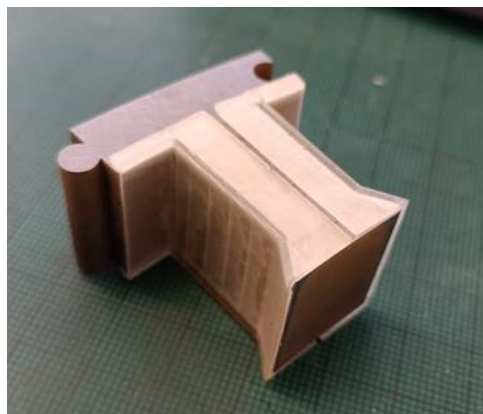


Figure 7-3: 3D printed cover

7.2.2 Base, pillars, and 3D printed tooth units and winding blocks

As the test model is suspended in the air during the experiment, a supporting structure is necessary. Furthermore, to reduce the effect on the airflow, the base and the pillars

on either side of the test model must be located sufficiently away from the test model – about five model widths. A heavy base was used to prevent the model from being blown over in the wind tunnel. Figure 7-4 shows the assembled supporting structure comprising the base and pillars.

Figure 7-5 shows the assembled 3D printed tooth units and winding blocks, which are made of a high temperature resin and offers a heat deflection temperature of 238 °C. Each side has five sets of tooth units and winding blocks. The high thermal resistance of these parts prevents the transport of heat away from the winding on both sides.

Type K plug-in thermocouples, as shown in Figure 7-6, were used to monitor the temperature variation in the test model.

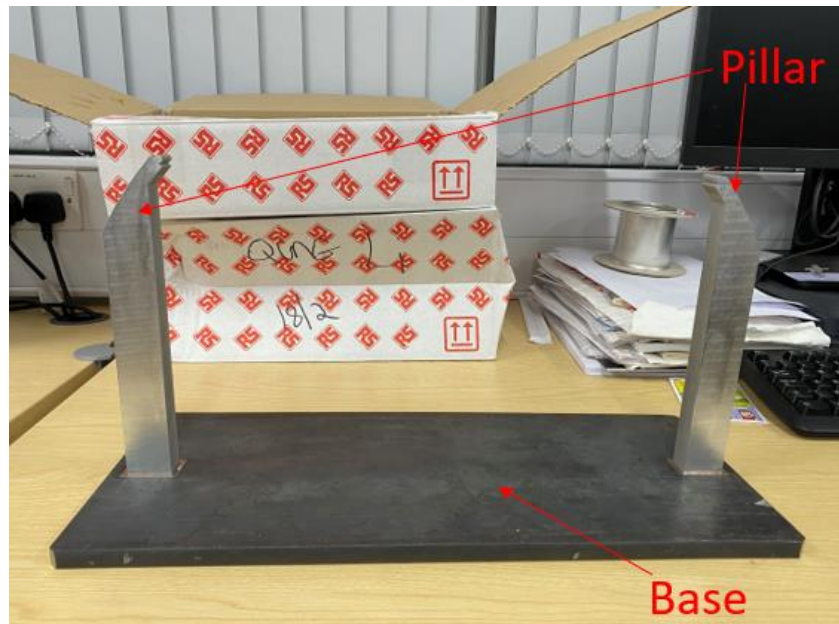


Figure 7-4: Assembled base and pillars



Figure 7-5: 3D printed tooth units and winding blocks

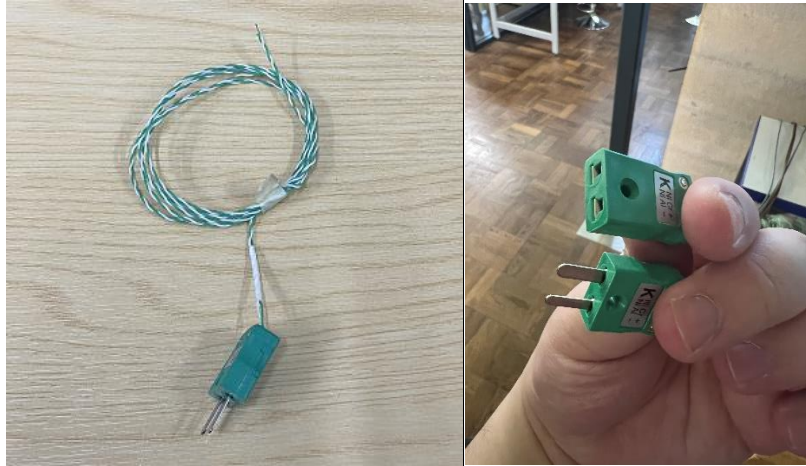


Figure 7-6: Type K plug-in thermocouple

7.2.3 Test model for hybrid cooling

Figure 7-7 shows the test model with the pipe, wherein the thermocouple was built-in during the winding process. The thermocouple measures the temperature of the hot spot of the model. To ensure that the cooling effect of the air cooling system is undisturbed, the outgoing wire of the thermocouple, the input and output wires of the coil, and the inlet and outlet of the water pipe are positioned on the downwind side of the models. Owing to the addition of the tubes, the stator slots are more crowded, and the 3D printed covers could no longer be used with these two models. To prevent short circuits in the windings, the corners of the stator tooth units were rounded, and insulating tape was wrapped between the windings and the teeth.



(a)

(b)

Figure 7-7: Test model with pipe of diameter: (a) 2 mm and (b) 3 mm

Figure 7-8 shows the design of the assembled hybrid cooling system. To ensure that each winding has the same water cooling effect, all three sets of pipes were connected

in parallel. Small water tanks were positioned at the left and right pillars, as shown in the inset of Figure 7-8. Each tank consists of a small sink for the input, which comprises the total input from the chiller, and three outputs corresponding to the inputs of the three tubes. The two tanks are oriented opposite to each other.

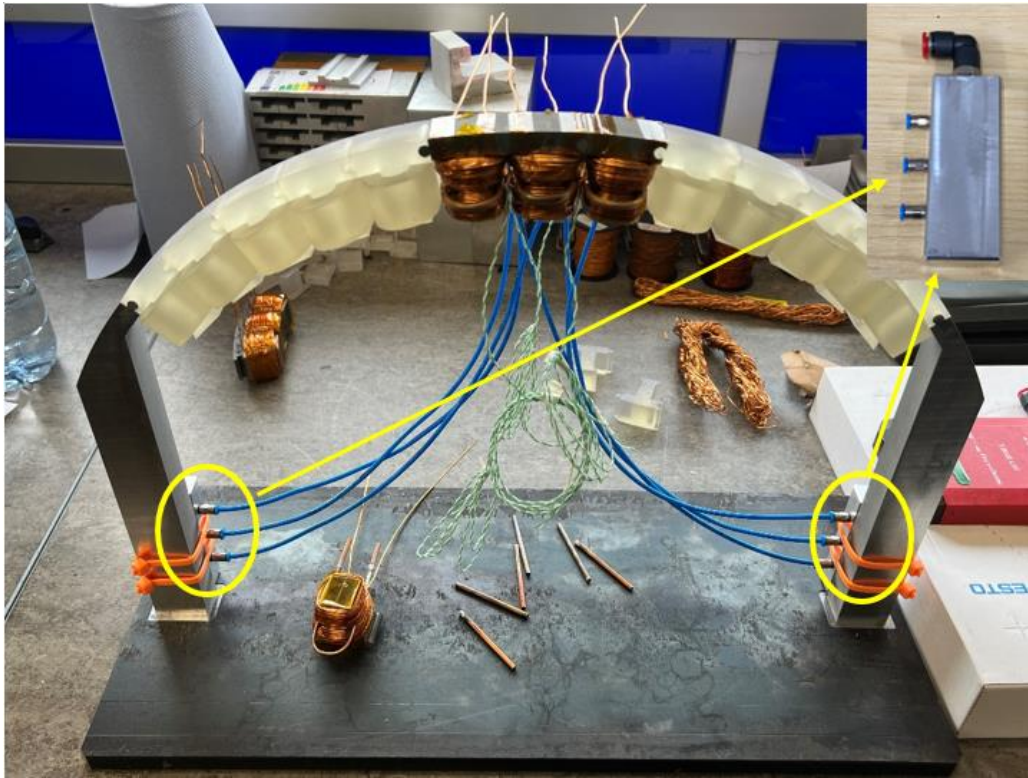


Figure 7-8: Assembled model for wind tunnel testing

The flow rate of the water must be controlled while testing the cooling performance of hybrid cooling system. The velocity and flow of the water are related according to Formula (7-1). The flow meter and valve control the total flow of water, which means that the flow rate must be calculated as the sum of the three pipes.

$$Q = SV \quad (7 - 1)$$

where Q is the flow rate, S is the area of the inner diameter of the pipe, and V is the water-flow velocity. The results of the calculations are shown in Table 7-1.

Table 7-1: Relationship between water-flow velocity and flow rate

Water pipe OD	Water-flow velocity	Flow rate
2 mm	1 m/s	10.26 l/h
	2 m/s	20.52 l/h
3 mm	1 m/s	37.41 l/h
	2 m/s	74.82 l/h

7.2.4 Calculation of coil resistance

Owing to the different insulation materials used between the coils and the teeth, and the need to maintain the same losses during the test, the resistance of the coils must be calculated. The resistance was measured directly using an inductance-capacitance-resistance meter. The results of the measured average resistance are shown in Table 7-2. The input voltage was also calculated and is listed in the table. At the same time, the input current densities all exceed 13 A/mm^2 .

Table 7-2: Key parameters of different models

Model	Average resistance	Input voltage
1	190.6 m Ω	8.3 V
2	196.5 m Ω	8.4 V
3	172.7 m Ω	8 V
4	171.1 m Ω	8 V

The first and second sets of models represent those without tubes – the first set represents the hand-wound coils and the second represents the machine-wound coils. The third and fourth sets represent the models with tubes, with outer diameters of 2 mm and 3 mm, respectively.

7.2.5 Changes to CAD model for thermal simulation

As the simulation model differed significantly from the actual test model, the model used for CFD simulation, which provides a comparison against the experimental test results, was redesigned, as shown in Figure 7-9.

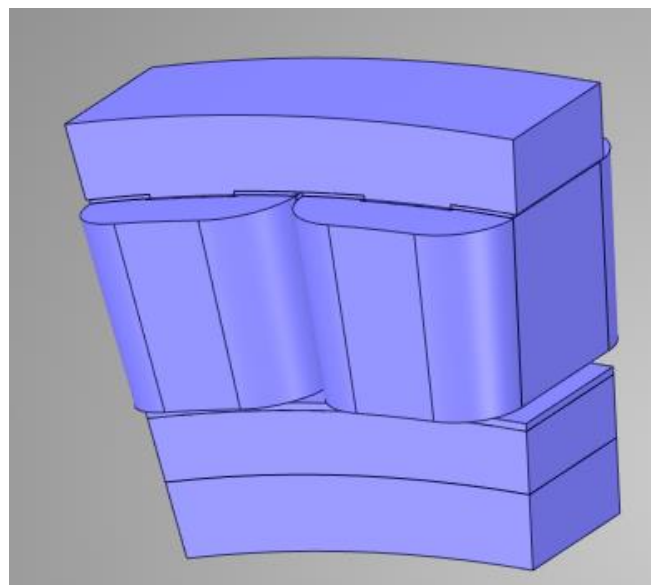


Figure 7-9: Redesigned CAD model

7.3 Tests and results

7.3.1 Pressure test

Before performing the thermal test in the wind tunnel, a pressure test must be conducted to ensure that there are no leaks in the cooling system, hoses, and tanks. The pressure test test rig is shown in Figure 7-10.

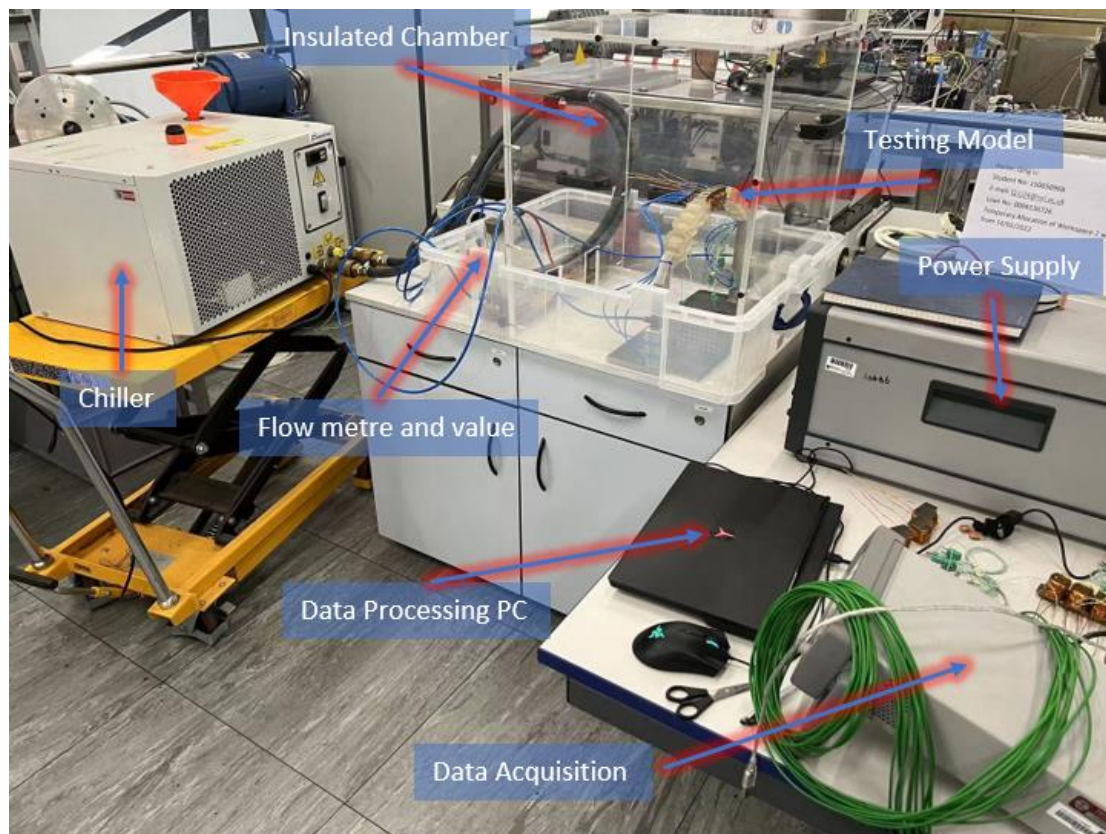


Figure 7-10: Test rig for pressure test

7.3.2 Test rig setup in wind tunnel

After the pressure test, the test model was moved into the wind tunnel. The subsequent experiments were conducted in the Wind Tunnel and Engine Test Cells at Northumbria University.

Figure 7-11 shows the model inside the wind tunnel. The front view reveals that all the lines and hoses are hidden behind the model or fixed to the floor using tape. This significantly reduces the impact on the airflow and increases safety. Figure 7-12 shows the experimental setup and configuration for the wind tunnel experiments.



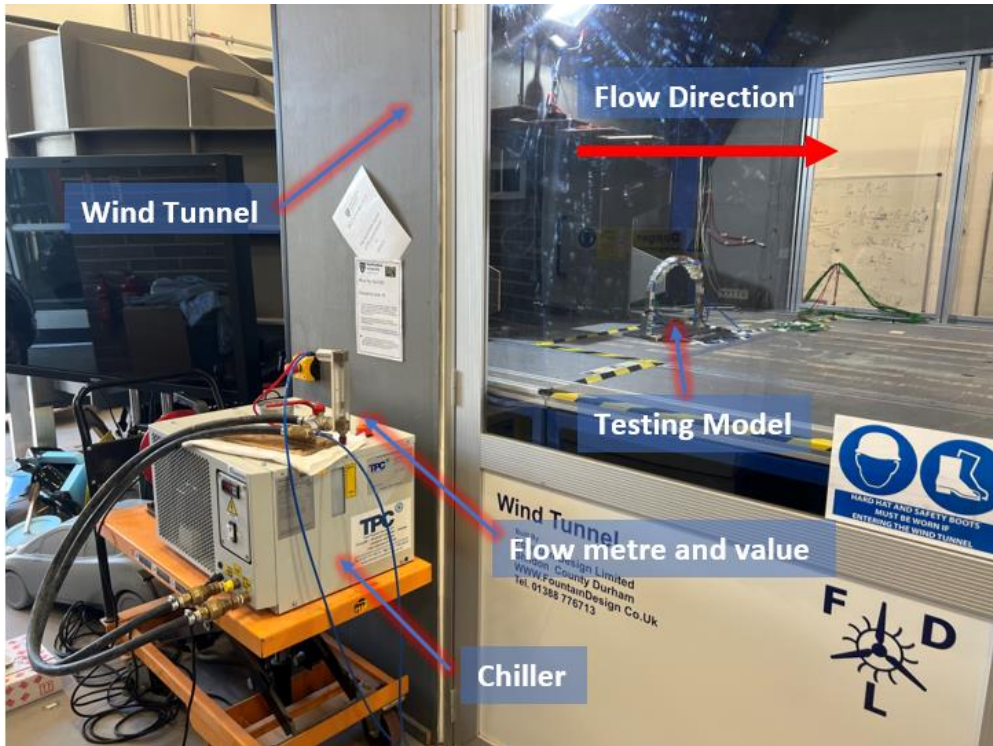
(a)



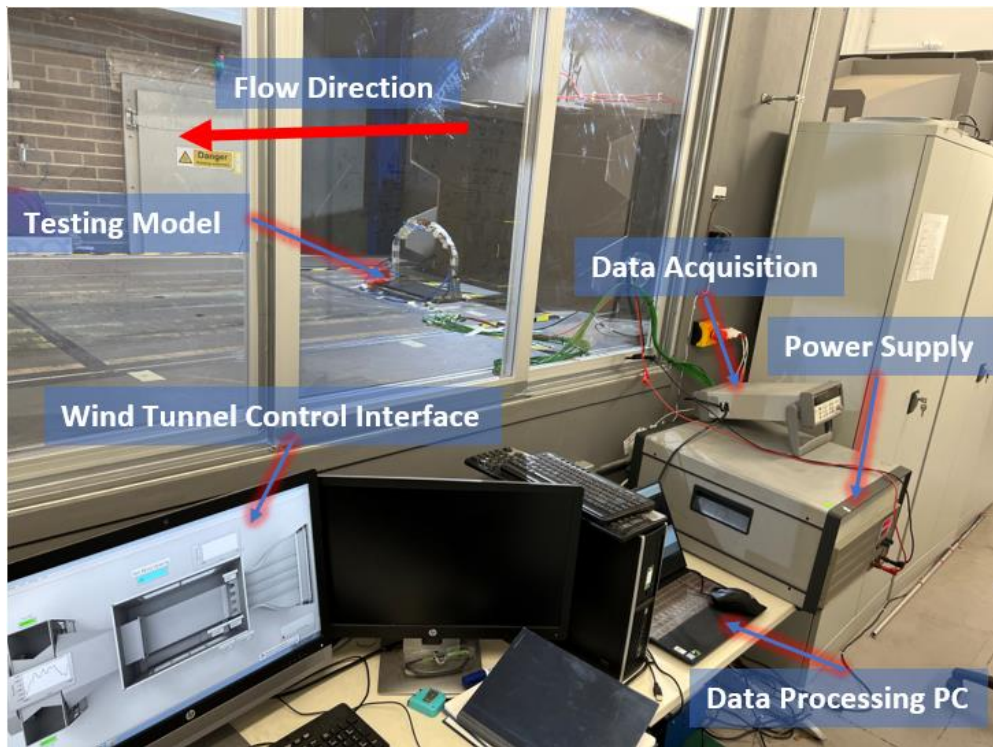
(b)

Figure 7-11: Model placed inside the wind tunnel: (a) front view and (b) side view

The wind speed in the wind tunnel increased to a maximum of 20 m/s during the test and the air turbulence intensity was fixed at approximately 0.5%.



(a)



(b)

**Figure 7-12: Test rig setup and configuration for the wind tunnel experiments:
(a) right side and (b) left side of wind tunnel**

7.3.3 Results analysis

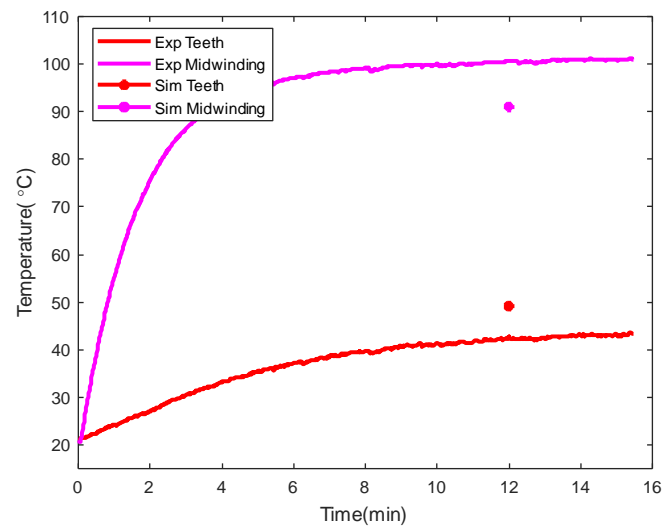


Figure 7-13: Comparison of experimental and numerical results at two measuring points for Model 1 at an airspeed of 10 m/s

For Models 1 and 2, the temperature was measured at two points – one on the surface of the middle winding and the other on the surface of the tooth. Figure 7-13 compares the experimental and simulation results for Model 1 at an airspeed of 10 m/s.

The results include a margin of error because the thickness of the slot liner in the simulation is only half of that in the test model. Furthermore, the windings are assumed to be fully impregnated when calculating the equivalent thermal conductivity of the simulated windings, whereas a large amount of air is still present in the windings in the test model, leading to a reduction in the thermal conductivity of the winding.

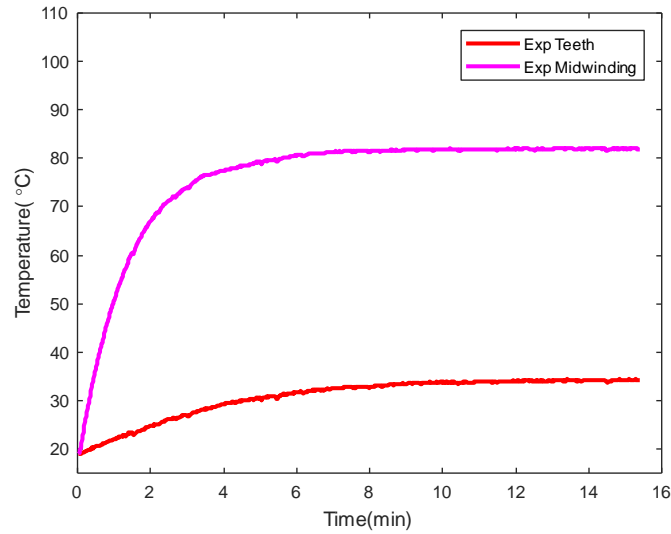


Figure 7-14: Experimental results for Model 1 at an airspeed of 15 m/s

Figure 7-14 shows the experimental results for Model 1 at an airspeed of 15 m/s. Comparing these results with those shown in Figure 7-13 reveals that the surface temperature of the middle winding has dropped by approximately 20% and the temperature on the teeth has dropped by 17%.

Figure 7-15 compares the experimental and simulation results for Model 2. Comparing these results with those of Model 1, the same error can be observed, but the relative error is smaller because Model 2 has a higher packing factor, which results in a higher thermal conductivity and a smaller volume of air in the winding. This is also responsible for the low temperature increase in Model 2 relative to Model 1.

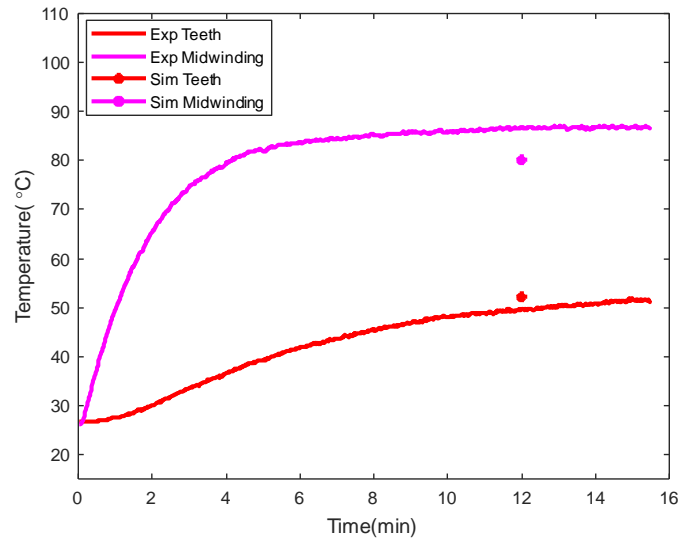


Figure 7-15: Comparison of experimental and numerical results at two measuring points for Model 2 at an airspeed of 10 m/s

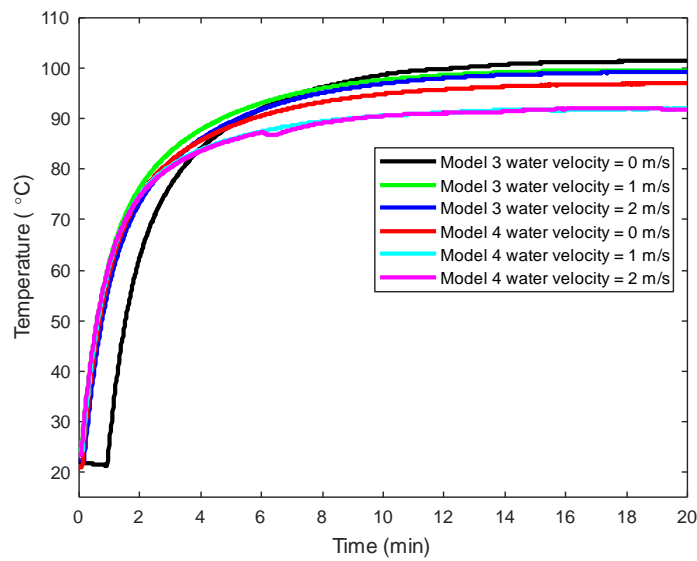


Figure 7-16: Comparison of hot spot temperature rise in Models 3 and 4 at an airspeed of 10 m/s

Figure 7-16 shows the hot spot temperatures of Models 3 and 4 at different water velocities. Both models exhibit some reduction in temperature with water cooling, but the temperature rise does not vary much with the increase in the water flow rate and there is some increase in the maximum temperature relative to the simulation results. This is because the tube is not in close contact with the winding, leading to a reduction in the cooling performance of the water cooling. The specific numerical increases in the hot spot temperatures of Models 3 and 4 are listed in Table 7-3.

Table 7-3: Experimental results of hot spot temperature rise

Air flow velocity	10 m/s		
Water flow velocity	0 m/s	1 m/s	2 m/s
Model 3	102 °C	99 °C	99 °C
Model 4	100 °C	95 °C	95 °C

7.3.4 Varnish sealed windings

Varnish was used to seal a part of the windings to bring the pipes into closer contact with the coils. Table 7-4 shows the results of the experiments after sealing a portion of the windings with varnish. Regardless of the water flow rate, the cooling performance improved by approximately 20%. Moreover, improvements of 12% and 15% were observed in Models 3 and 4, respectively, even in the absence of water cooling. The results are also more comparable to the simulation results.

Table 7-4: Experimental results of hot spot temperature rise after sealing the windings with varnish

Air flow velocity	10 m/s		
Water flow velocity	0 m/s	1 m/s	2 m/s
Model 3	90 °C	80 °C	80 °C
Model 4	84.4 °C	74 °C	73 °C

7.4 Conclusion

This chapter first described the process of preparing the experimental model and setting up the experiment. This was followed by presenting the experimental results and comparing them with the CFD simulation results.

The experimental tests in the wind tunnel were completed successfully. The results revealed that the proposed hybrid cooling design is effective and can significantly reduce the maximum temperature rise which is nearly 30 °C in the windings.

Chapter 8 Conclusion and Future Work

8.1 Conclusion

This study investigated the electromagnetic design, modelling, performance optimisation, fault tolerant design and thermal management of permanent magnet motors for electric tail rotor applications in helicopters.

Due to concern about environmental pollution, MEA is gaining increasing attention for the many advantages it brings in the replacement of conventional systems with electrical systems. Electrical machines, particularly those used for permanent magnet motors, play a very important role in drive and MEA systems and have a wide range of applications.

The electrification of helicopters is a topic of great interest due to their high manoeuvrability for vertical take-off, landing and hovering. A topology for a permanent magnet motor has been proposed for use as an electric tail rotor in helicopters. The performance of this motor was investigated by FE simulation. Through continuous optimisation, its performance has reached the requirements. Due to its specific application, high reliability is a necessary requirement and fault-tolerant design was therefore also proposed. The interspersed winding arrangement was selected because of its lower torque ripple and higher torque during faulted operation. Across a range of designs, the motor was able to deliver more than 70% of its output torque in the event of a short circuit.

Thermal management is also an important part of motor design. This study provides a detailed understanding of heat dissipation in the stator section through CFD simulations. The cooling performance of the motor stator winding has been further improved by better understanding and optimising some parameters, such as air turbulence intensity, air channel concept and width. In order to further reduce the winding temperature increase, a new hybrid cooling design has been proposed. Additionally, the results of the thermal simulation were verified in wind tunnel experiments. This experiment verifies the feasibility of this new hybrid cooling design.

8.2 Future work

- As evidenced in this study, significant losses are still caused to the rotor in an electric design, particularly on the permanent magnets. Although some of the

rotor losses have been reduced through careful selection of the combination of pole slots, the motor still generates considerable losses in the rotor. Therefore, rotor losses, and especially permanent magnet losses, need to be taken into account and attended to in future work.

- Only the stator section was taken into account during the thermal simulation and wind tunnel experimental verification. In future work, the rotor heat dissipation will also need to be considered.

Reference

- [1] Ritchie, H. (2020) *Climate change and flying: What share of Global CO2 Emissions Come From Aviation?*, *Our World in Data*. Available at: <https://ourworldindata.org/co2-emissions-from-aviation> (Accessed: May 7, 2021).
- [2] Roboam, X., Sareni, B. and De Andrade, A., 2012. More electricity in the air: Toward optimized electrical networks embedded in more-electrical aircraft. *IEEE industrial electronics magazine*, 6(4), pp.6-17.
- [3] Faleiro, L., 2005. Beyond the more electric aircraft. *Aerospace America*, 43(9), pp.35-40.
- [4] He, J., Zhang, D. and Torrey, D., 2018, July. Recent advances of power electronics applications in more electric aircrafts. In *2018 AIAA/IEEE Electric Aircraft Technologies Symposium (EATS)* (pp. 1-8). IEEE.
- [5] Sarlioglu, B. and Morris, C.T., 2015. More electric aircraft: Review, challenges, and opportunities for commercial transport aircraft. *IEEE transactions on Transportation Electrification*, 1(1), pp.54-64.
- [6] Buticchi, G., Costa, L. and Liserre, M., 2017. Improving system efficiency for the more electric aircraft: A look at dcVdc converters for the avionic onboard dc microgrid. *IEEE Industrial Electronics Magazine*, 11(3), pp.26-36.
- [7] Jones, R.I., 2002. The more electric aircraft—assessing the benefits. *Proceedings of the Institution of Mechanical Engineers, Part G: Journal of Aerospace Engineering*, 216(5), pp.259-269.
- [8] Donato, T., Ficarella, A. and Spedicato, L., 2018, June. Applying dynamic programming algorithms to the energy management of hybrid electric aircraft. In *Turbo Expo: Power for Land, Sea, and Air* (Vol. 51043, p. V003T06A015). American Society of Mechanical Engineers.
- [9] Gurevich, O., Lukovnikov, A., Gulienko, A., Zakharchenko, V., Kovalenko, I. and Suntsov, P., 2014, September. Analysis of possibilities to apply electric technologies for helicopter propulsion system. In *Proceedings of the 29th Congress of the International Council of the Aeronautical Sciences (ICAS 2014), St. Petersburg, Russia* (Vol. 4, pp. 2864-2869).
- [10] Donato, T., Carlà, A. and Avanzini, G., 2018. Fuel consumption of rotorcrafts and potentiality for hybrid electric power systems. *Energy Conversion and Management*, 164, pp.429-442.
- [11] Brelje, B.J. and Martins, J.R., 2019. Electric, hybrid, and turboelectric fixed-wing aircraft: A review of concepts, models, and design approaches. *Progress in Aerospace Sciences*, 104, pp.1-19.

- [12] Weimer, J.A., 1993, October. Electrical power technology for the more electric aircraft. In *[1993 Proceedings] AIAA/IEEE Digital Avionics Systems Conference* (pp. 445-450). IEEE.
- [13] Glass-Hooper, D.T., 1916. The electric control of large aeroplanes. *Flight*, 8(51), p.1118.
- [14] Jones, R.I., 1999, November. The More Electric Aircraft: the past and the future?. In *IEE Colloquium on Electrical Machines and Systems for the More Electric Aircraft (Ref. No. 1999/180)* (pp. 1-1). IET.
- [15] Rosero, J.A., Ortega, J.A., Aldabas, E. and Romeral, L.A.R.L., 2007. Moving towards a more electric aircraft. *IEEE Aerospace and Electronic Systems Magazine*, 22(3), pp.3-9.
- [16] Cao, W., Mecrow, B.C., Atkinson, G.J., Bennett, J.W. and Atkinson, D.J., 2011. Overview of electric motor technologies used for more electric aircraft (MEA). *IEEE transactions on industrial electronics*, 59(9), pp.3523-3531.
- [17] Wheeler, P.W., Clare, J.C., Trentin, A. and Bozhko, S., 2013. An overview of the more electrical aircraft. *Proceedings of the Institution of Mechanical Engineers, Part G: Journal of Aerospace Engineering*, 227(4), pp.578-585.
- [18] Thapa, N., Ram, S., Kumar, S. and Mehta, J., 2021. All electric aircraft: A reality on its way. *Materials Today: Proceedings*, 43, pp.175-182.
- [19] Wang, Y., Nuzzo, S., Zhang, H., Zhao, W., Gerada, C. and Galea, M., 2020. Challenges and opportunities for wound field synchronous generators in future more electric aircraft. *IEEE Transactions on Transportation Electrification*, 6(4), pp.1466-1477.
- [20] Provost, M.J., 2002, June. The more electric aero-engine: A general overview from an engine manufacturer. In *2002 International Conference on Power Electronics, Machines and Drives (Conf. Publ. No. 487)* (pp. 246-251). IET.
- [21] Rajashekara, K., 2014. Power electronics for more electric aircraft. *Power Electronics for Renewable Energy Systems, Transportation and Industrial Applications*, pp.365-386.
- [22] Quigley, R.E.J., 1993, March. More electric aircraft. In *Proceedings Eighth Annual Applied Power Electronics Conference and Exposition*, (pp. 906-911). IEEE.
- [23] Howse, M., 2003. All-electric aircraft. *Power Engineer*, 17(4), pp.35-37.
- [24] Chen, J., Wang, C. and Chen, J., 2018. Investigation on the selection of electric power system architecture for future more electric aircraft. *IEEE Transactions on Transportation Electrification*, 4(2), pp.563-576.
- [25] Emadi, K. and Ehsani, M.J.I.A., 2000. Aircraft power systems: technology, state of the art, and future trends. *IEEE Aerospace and Electronic Systems Magazine*, 15(1), pp.28-32.

- [26] Rahrovi, B. and Ehsani, M., 2019, February. A review of the more electric aircraft power electronics. In *2019 IEEE Texas Power and Energy Conference (TPEC)* (pp. 1-6). IEEE.
- [27] Asaei, B. and Rahrovi, B., 2010, September. Minimum-copper-loss control over full speed range of an IPMSM drive for hybrid electric vehicle application. In *2010 IEEE vehicle power and propulsion conference* (pp. 1-6). IEEE.
- [28] Pearson, W., 1998. The more electric/all electric aircraft-a military fast jet perspective.
- [29] Moir, I. and Seabridge, A., 2011. *Aircraft Systems: Mechanical, electrical, and avionics subsystems integration*. John Wiley & Sons.
- [30] Feiner, L.J., 1993, October. Power-by-wire aircraft secondary power systems. In *[1993 Proceedings] AIAA/IEEE Digital Avionics Systems Conference* (pp. 439-444). IEEE.
- [31] Sinnott, M., 2007. 787 no-bleed systems: saving fuel and enhancing operational efficiencies. *Aero Quarterly*, 18, pp.6-11.
- [32] Moir, I. and Seabridge, A., 2011. *Aircraft Systems: Mechanical, electrical, and avionics subsystems integration*. John Wiley & Sons.
- [33] *News & events single : Airbus, a leading aircraft manufacturer (2005) | Airbus News & Events*. Available at: <https://web.archive.org/web/20141004080800/http://www.airbus.com/newsevents/news-events-single/detail/a380-the-21st-century-flagship-successfully-completes-its-first-flight/> (Accessed: September 17, 2021).
- [34] Johnson, W., 2012. *Helicopter theory*. Courier Corporation.
- [35] Karimoddini, A., Lin, H., Chen, B.M. and Lee, T.H., 2014. Hierarchical hybrid modelling and control of an unmanned helicopter. *International Journal of Control*, 87(9), pp.1779-1793.
- [36] *Helicopter rotor* (2022) *Wikipedia*. Wikimedia Foundation. Available at: https://en.wikipedia.org/wiki/Helicopter_rotor (Accessed: October 3, 2021).
- [37] Alpman, E., Long, L.N. and Kothman, B.D., 2004. Understanding ducted rotor antitorque and directional control characteristics part II: unsteady simulations. *Journal of Aircraft*, 41(6), pp.1370-1378.
- [38] Johnson, W., 2013. *Rotorcraft aeromechanics* (Vol. 36). Cambridge University Press.
- [39] Kebriaei, M., Niasar, A.H. and Asaei, B., 2015, October. Hybrid electric vehicles: An overview. In *2015 International Conference on Connected Vehicles and Expo (ICCVE)* (pp. 299-305). IEEE.
- [40] Donato, T., De Pascalis, C.L., Strafella, L. and Ficarella, A., 2021. Off-line and on-line optimization of the energy management strategy in a Hybrid Electric Helicopter for urban air-mobility. *Aerospace Science and Technology*, 113, p.106677.

- [41] Bolvashenkov, I., Kammermann, J. and Herzog, H.G., 2017, December. Electrification of helicopter: actual feasibility and prospects. In *2017 IEEE Vehicle Power and Propulsion Conference (VPPC)* (pp. 1-6). IEEE.
- [42] Bolvashenkov, I., Kammermann, J., Herzog, H.G. and Zeng, W., 2019, May. Reliability Evaluation of non-Repairable Propulsion Systems of Hybrid-Electric Helicopter with Different Level of Hybridization. In *2019 Fourteenth International Conference on Ecological Vehicles and Renewable Energies (EVER)* (pp. 1-6). IEEE.
- [43] Mellor, P.H., Yon, J., Baker, J.L., North, D. and Booker, J.D., 2017, May. Electromagnetic and thermal coupling within a fault-tolerant aircraft propulsion motor. In *2017 IEEE International Electric Machines and Drives Conference (IEMDC)* (pp. 1-7). IEEE.
- [44] Bolvashenkov, I., Kammermann, J. and Herzog, H.G., 2017, April. Reliability assessment of a fault tolerant propulsion system for an electrical helicopter. In *2017 Twelfth International Conference on Ecological Vehicles and Renewable Energies (EVER)* (pp. 1-6). IEEE.
- [45] Booker, J.D., North, D., Yon, J.M. and Mellor, P.H., 2019. Generator configuration for helicopter quadruplex electric tail rotor. *The Journal of Engineering*, 2019(17), pp.4471-4474.
- [46] Abdelrahem, M., Hackl, C.M. and Kennel, R., 2017. Finite position set-phase locked loop for sensorless control of direct-driven permanent-magnet synchronous generators. *IEEE Transactions on Power Electronics*, 33(4), pp.3097-3105.
- [47] Zhang, Z., Huang, J., Jiang, Y., Geng, W. and Xu, Y., 2017. Overview and analysis of PM starter/generator for aircraft electrical power systems. *CES Transactions on Electrical Machines and Systems*, 1(2), pp.117-131.
- [48] Yon, J.M., Baker, J.L., Mellor, P.H., Williamson, S.J. and Wrobel, R., 2017, May. Test characterization of a high performance fault tolerant permanent magnet machine. In *2017 IEEE International Electric Machines and Drives Conference (IEMDC)* (pp. 1-8). IEEE.
- [49] Castellini, L., D'Andrea, M. and Villani, M., 2016, November. Electric powertrain for helicopter tail rotor. In *2016 6th International Electric Drives Production Conference (EDPC)* (pp. 268-273). IEEE.
- [50] Fabri, G., Parasiliti, F., Tursini, M., Villani, M. and Castellini, L., 2017, May. PM brushless motor for helicopters electric tail rotor drive system. In *2017 IEEE International Electric Machines and Drives Conference (IEMDC)* (pp. 1-7). IEEE.
- [51] Villani, M., Collazzo, F.P., Tursini, M., Fabri, G. and Castellini, L., 2016, September. PM brushless motor design for helicopter tail rotor. In *2016 XXII International Conference on Electrical Machines (ICEM)* (pp. 2669-2675). IEEE.
- [52] Villani, M., Parasiliti, F., Tursini, M., Fabri, G. and Castellini, L., 2016, June. PM brushless motors comparison for a Fenestron® type helicopter tail rotor. In *2016*

- International Symposium on Power Electronics, Electrical Drives, Automation and Motion (SPEEDAM)* (pp. 22-27). IEEE.
- [53] Villani, M., Tursini, M., Fabri, G. and Castellini, L., 2010, September. Fault-tolerant PM brushless DC drive for aerospace application. In *The XIX International Conference on Electrical Machines-ICEM 2010* (pp. 1-7). IEEE.
- [54] Jahns, T.M., 1980. Improved reliability in solid-state AC drives by means of multiple independent phase drive units. *IEEE Transactions on Industry Applications*, (3), pp.321-331.
- [55] Jack, A.G., Mecrow, B.C. and Haylock, J.A., 1996. A comparative study of permanent magnet and switched reluctance motors for high-performance fault-tolerant applications. *IEEE transactions on industry applications*, 32(4), pp.889-895.
- [56] Bianchi, N., Pre, M.D., Grezzani, G. and Bolognani, S., 2005, May. Design considerations on fractional-slot fault-tolerant synchronous motors. In *IEEE International Conference on Electric Machines and Drives, 2005*. (pp. 902-909). IEEE.
- [57] Nall, S. and Mellor, P.H., 2008. Compact direct-drive permanent magnet motor for a UAV rotorcraft with improved faulted behaviour through operation as four separate three-phase machines.
- [58] Villani, M., Tursini, M., Fabri, G. and Castellini, L., 2010, October. Multi-phase fault tolerant drives for aircraft applications. In *Electrical Systems for Aircraft, Railway and Ship Propulsion* (pp. 1-6). IEEE.
- [59] Villani, M., Tursini, M., Fabri, G. and Castellini, L., 2013. Electromechanical actuator for helicopter rotor damper application. *IEEE Transactions on Industry Applications*, 50(2), pp.1007-1014.
- [60] Farman, J., 2013. *Electric tail rotor drive for the more-electric helicopter: a feasibility study* (Doctoral dissertation, University of Bristol).
- [61] Krishnamurthy, M., Edrington, C.S. and Fahimi, B., 2005, June. Comparison of various converter topologies for bipolar switched reluctance motor drives. In *2005 IEEE 36th Power Electronics Specialists Conference* (pp. 1858-1864). IEEE.
- [62] Barcaro, M., Bianchi, N. and Magnussen, F., 2010. Analysis and tests of a dual three-phase 12-slot 10-pole permanent-magnet motor. *IEEE Transactions on Industry Applications*, 46(6), pp.2355-2362.
- [63] Gopalarathnam, T., Toliyat, H.A. and Moreira, J.C., 2000, October. Multi-phase fault-tolerant brushless DC motor drives. In *Conference Record of the 2000 IEEE Industry Applications Conference. Thirty-Fifth IAS Annual Meeting and World Conference on Industrial Applications of Electrical Energy (Cat. No. 00CH37129)* (Vol. 3, pp. 1683-1688). IEEE.
- [64] Baudart, F., Labrique, F., Matagne, E., Telteu, D. and Alexandre, P., 2009, March. Control under normal and fault tolerant operation of multiphase SMPM synchronous

- machines with mechanically and magnetically decoupled phases. In *2009 International Conference on Power Engineering, Energy and Electrical Drives* (pp. 461-466). IEEE.
- [65] Nakahama, T., Biswas, D., Kawano, K. and Ishibashi, F., 2006. Improved cooling performance of large motors using fans. *IEEE Transactions on Energy Conversion*, 21(2), pp.324-331.
- [66] Akawung, A.F. and Fujimoto, Y., 2019, June. Design and thermal analysis of cooling system for high-power density motor based on air-flow. In *2019 IEEE 28th International Symposium on Industrial Electronics (ISIE)* (pp. 273-278). IEEE.
- [67] Kondjoyan, A., Péneau, F. and Boisson, H.C., 2002. Effect of high free stream turbulence on heat transfer between plates and air flows: a review of existing experimental results. *International journal of thermal sciences*, 41(1), pp.1-16.
- [68] Dong, J., Huang, Y., Jin, L., Lin, H. and Yang, H., 2014. Thermal optimization of a high-speed permanent magnet motor. *IEEE Transactions on Magnetics*, 50(2), pp.749-752.
- [69] Li, J., Lu, Y., Cho, Y.H. and Qu, R., 2018, September. Design and Analysis of a Water-Cooled Axial Flux Permanent-Magnet Machine for Large Power Direct-Driven Applications. In *2018 XIII International Conference on Electrical Machines (ICEM)* (pp. 118-124). IEEE.
- [70] Semidey, S.A. and Mayor, J.R., 2014. Experimentation of an electric machine technology demonstrator incorporating direct winding heat exchangers. *IEEE Transactions on Industrial Electronics*, 61(10), pp.5771-5778.
- [71] Lindh, P., Petrov, I., Jaatinen-Värri, A., Grönman, A., Martinez-Iturralde, M., Satrustegui, M. and Pyrhönen, J., 2017. Direct liquid cooling method verified with an axial-flux permanent-magnet traction machine prototype. *IEEE Transactions on Industrial Electronics*, 64(8), pp.6086-6095.
- [72] Gai, Y., Kimiabeigi, M., Chong, Y.C., Widmer, J.D., Deng, X., Popescu, M., Goss, J., Staton, D.A. and Steven, A., 2018. Cooling of automotive traction motors: schemes, examples, and computation methods. *IEEE Transactions on Industrial Electronics*, 66(3), pp.1681-1692.
- [73] Simpson, N., Wrobel, R. and Mellor, P.H., 2013. Estimation of equivalent thermal parameters of impregnated electrical windings. *IEEE Transactions on Industry Applications*, 49(6), pp.2505-2515.
- [74] Rama Krishna, S., Rama Krishna, A. and Ramji, K., 2010. An experimental study on the reduction of motor-fan noise by modification of the blade and shroud configuration. *Proceedings of the Institution of Mechanical Engineers, Part C: Journal of Mechanical Engineering Science*, 224(2), pp.315-320.
- [75] Rao, G.S. and Rao, V.S., 2011. Design of cooling fan for noise reduction using CFD. *Int. J. Sci. Eng. Res*, 2, pp.1-5.

- [76] North, D., Yon, J., Baker, J., Booker, J. and Mellor, P., 2019. Design route towards a PM machine for rotorcraft environments. *The Journal of Engineering*, 2019(17), pp.3720-3724.
- [77] Wheeler, P. and Bozhko, S., 2014. The more electric aircraft: Technology and challenges. *IEEE Electrification Magazine*, 2(4), pp.6-12.
- [78] Song, Z., Liu, C. and Zhao, H., 2019, August. Comparative analysis of slotless and coreless permanent magnet synchronous machines for electric aircraft propulsion. In *2019 22nd International Conference on Electrical Machines and Systems (ICEMS)* (pp. 1-6). IEEE.
- [79] Lisnianski, A., Frenkel, I. and Karagrigoriou, A. eds., 2017. *Recent advances in multi-state systems reliability: Theory and applications*. Springer.
- [80] Xia, B., Shen, J.X., Luk, P.C.K. and Fei, W., 2014. Comparative study of air-cored axial-flux permanent-magnet machines with different stator winding configurations. *IEEE Transactions on Industrial Electronics*, 62(2), pp.846-856.
- [81] Baumgartner, T., Burkart, R. and Kolar, J.W., 2012, October. Analysis and design of an ultra-high-speed slotless self-bearing permanent-magnet motor. In *IECON 2012-38th Annual Conference on IEEE Industrial Electronics Society* (pp. 4477-4483). IEEE.
- [82] Lee, C.H., Chau, K.T. and Liu, C., 2013. Electromagnetic design and analysis of magnetless double-rotor dual-mode machines. *Progress In Electromagnetics Research*, 142, pp.333-351.
- [83] Mizuno, S., Noda, S., Matsushita, M., Koyama, T. and Shiraishi, S., 2013. Development of a totally enclosed fan-cooled traction motor. *IEEE Transactions on Industry Applications*, 49(4), pp.1508-1514.
- [84] Herbert, W.A., 2013. Totally enclosed fan-cooled squirrel-cage induction motor options. *IEEE Transactions on Industry Applications*, 50(2), pp.1590-1598.
- [85] Shams Ghahfarokhi, P., Kallaste, A., Podgornovs, A., Belahcen, A., Vaimann, T. and Asad, B., 2021. Determination of heat transfer coefficient of finned housing of a TEFC variable speed motor. *Electrical Engineering*, 103(2), pp.1009-1017.
- [86] Dong, C., Qian, Y., Zhang, Y. and Zhuge, W., 2020. A review of thermal designs for improving power density in electrical machines. *IEEE Transactions on Transportation Electrification*, 6(4), pp.1386-1400.
- [87] Rosu, M., Zhou, P., Lin, D., Ionel, D.M., Popescu, M., Blaabjerg, F., Rallabandi, V. and Staton, D., 2017. *Multiphysics simulation by design for electrical machines, power electronics and drives*. John Wiley & Sons.
- [88] Ulbrich, S., Kopte, J. and Proske, J., 2017. Cooling fin optimization on a TEFC electrical machine housing using a 2-D conjugate heat transfer model. *IEEE Transactions on Industrial Electronics*, 65(2), pp.1711-1718.

- [89] Valenzuela, M.A. and Tapia, J.A., 2008. Heat transfer and thermal design of finned frames for TEFC variable-speed motors. *IEEE Transactions on Industrial Electronics*, 55(10), pp.3500-3508.
- [90] Lahne, H.C., Gerling, D., Staton, D. and Chong, Y.C., 2016, April. Design of a 50000 rpm high-speed high-power six-phase PMSM for use in aircraft applications. In *2016 Eleventh International Conference on Ecological Vehicles and Renewable Energies (EVER)* (pp. 1-11). IEEE.
- [91] Yung, C., 2015. Cool facts about cooling electric motors: improvements in applications that fall outside the normal operating conditions. *IEEE Industry Applications Magazine*, 21(6), pp.47-56.
- [92] Yang, Y., Bilgin, B., Kasprzak, M., Nalakath, S., Sadek, H., Preindl, M., Cotton, J., Schofield, N. and Emadi, A., 2017. Thermal management of electric machines. *IET Electrical Systems in Transportation*, 7(2), pp.104-116.
- [93] Stone, G.C., Boulter, E.A., Culbert, I. and Dhirani, H., 2004. *Electrical insulation for rotating machines: design, evaluation, aging, testing, and repair* (Vol. 21). John Wiley & Sons.
- [94] Staton, D., 2014, June. Thermal analysis of traction motors. In *2014 IEEE Transportation Electrification Conference and Expo (ITEC)* (pp. 1-139). IEEE.
- [95] Li, H., 2010. Cooling of a permanent magnet electric motor with a centrifugal impeller. *International journal of heat and mass transfer*, 53(4), pp.797-810.
- [96] Ye, L., Li, D., Ma, Y. and Jiao, B., 2011. Design and performance of a water-cooled permanent magnet retarder for heavy vehicles. *IEEE Transactions on Energy Conversion*, 26(3), pp.953-958.
- [97] Kral, C., Haumer, A. and Bauml, T., 2008. Thermal model and behavior of a totally-enclosed-water-cooled squirrel-cage induction machine for traction applications. *IEEE Transactions on Industrial Electronics*, 55(10), pp.3555-3565.
- [98] Zhang, B., Qu, R., Xu, W., Wang, J. and Chen, Y., 2014, September. Thermal model of totally enclosed water-cooled permanent magnet synchronous machines for electric vehicle applications. In *2014 International Conference on Electrical Machines (ICEM)* (pp. 2205-2211). IEEE.
- [99] Li, S., Zhang, S., Habetler, T.G. and Harley, R.G., 2019. Modeling, design optimization, and applications of switched reluctance machines—a review. *IEEE Transactions on Industry Applications*, 55(3), pp.2660-2681.
- [100] Zabihi, N. and Gouws, R., 2016, June. A review on switched reluctance machines for electric vehicles. In *2016 IEEE 25th International Symposium on Industrial Electronics (ISIE)* (pp. 799-804). IEEE.
- [101] Mishra, A., Agarwal, P. and Srivastava, S.P., 2014. A comprehensive analysis and implementation of vector control of permanent magnet synchronous motor. *International Journal of Power and Energy Conversion*, 5(1), pp.1-23.

- [102] Pellegrino, G., Vagati, A., Guglielmi, P. and Boazzo, B., 2011. Performance comparison between surface-mounted and interior PM motor drives for electric vehicle application. *IEEE Transactions on Industrial Electronics*, 59(2), pp.803-811.
- [103] Dong, J., Huang, Y., Jin, L. and Lin, H., 2016. Comparative study of surface-mounted and interior permanent-magnet motors for high-speed applications. *IEEE Transactions on Applied Superconductivity*, 26(4), pp.1-4.
- [104] Gieras, J.F., 2008. *Advancements in electric machines*. Springer Science & Business Media.
- [105] Coey, J.M.D., 2011. Hard magnetic materials: A perspective. *IEEE Transactions on magnetics*, 47(12), pp.4671-4681.
- [106] Coey, J.D., 2001. Magnetic materials. *Journal of Alloys and Compounds*, 326(1-2), pp.2-6.
- [107] Spaldin, N.A., 2010. *Magnetic materials: fundamentals and applications*. Cambridge university press.
- [108] Gutfleisch, O., Willard, M.A., Brück, E., Chen, C.H., Sankar, S.G. and Liu, J.P., 2011. Magnetic materials and devices for the 21st century: stronger, lighter, and more energy efficient. *Advanced materials*, 23(7), pp.821-842.
- [109] Grössinger, R., 2008. Characterisation of hard magnetic materials. *Journal of Electrical Engineering*, 59(7), pp.15-20.
- [110] *Samarium–Cobalt Magnet (2022) Wikipedia*. Wikimedia Foundation. Available at: https://en.wikipedia.org/wiki/Samarium%E2%80%93cobalt_magnet (Accessed: February 3, 2022).
- [111] *Neodymium magnet (2022) Wikipedia*. Wikimedia Foundation. Available at: https://en.wikipedia.org/wiki/Neodymium_magnet (Accessed: February 3, 2022).
- [112] *Simcenter Magnet: Siemens software (no date) Siemens Digital Industries Software*. Available at: <https://www.plm.automation.siemens.com/global/en/products/simcenter/magnet.html> (Accessed: February 4, 2022).
- [113] Bhavikatti, S.S., 2005. *Finite element analysis*. New Age International.
- [114] *NOTAR (2022) Wikipedia*. Wikimedia Foundation. Available at: <https://en.wikipedia.org/wiki/NOTAR> (Accessed: June 5, 2021).
- [115] *Permeability (electromagnetism) (2022) Wikipedia*. Wikimedia Foundation. Available at: [https://en.wikipedia.org/wiki/Permeability_\(electromagnetism\)](https://en.wikipedia.org/wiki/Permeability_(electromagnetism)) (Accessed: November 23, 2021).
- [116] Hanselman, D.C., 2003. *Brushless permanent magnet motor design*. The Writers' Collective.

- [117] Taran, N., Rallabandi, V., Ionel, D.M., Heins, G. and Patterson, D., 2019, May. A comparative study of methods for calculating ac winding losses in permanent magnet machines. In *2019 IEEE International Electric Machines & Drives Conference (IEMDC)* (pp. 2265-2271). IEEE.
- [118] Mellor, P.H., Wrobel, R. and McNeill, N., 2006, October. Investigation of proximity losses in a high speed brushless permanent magnet motor. In *Conference Record of the 2006 IEEE Industry Applications Conference Forty-First IAS Annual Meeting* (Vol. 3, pp. 1514-1518). IEEE.
- [119] Madina, P., Poza, J., Ugalde, G. and Almandoz, G., 2011, August. Magnet eddy current loss calculation method for segmentation analysis on permanent magnet machines. In *Proceedings of the 2011 14th European Conference on Power Electronics and Applications* (pp. 1-9). IEEE.
- [120] Zhu, Z.Q., Ruangsinchaiwanich, S. and Howe, D., 2006. Synthesis of cogging-torque waveform from analysis of a single stator slot. *IEEE transactions on industry applications*, 42(3), pp.650-657.
- [121] Huang, W.Y., Bettayeb, A., Kaczmarek, R. and Vannier, J.C., 2010. Optimization of magnet segmentation for reduction of eddy-current losses in permanent magnet synchronous machine. *IEEE Transactions on energy conversion*, 25(2), pp.381-387.
- [122] Polinder, H. and Hoeijmakers, M.J., 1997. Eddy-current losses in the permanent magnets of a PM machine.
- [123] Atallah, K., Howe, D., Mellor, P.H. and Stone, D.A., 2000. Rotor loss in permanent-magnet brushless AC machines. *IEEE transactions on industry applications*, 36(6), pp.1612-1618.
- [124] Toda, H., Xia, Z., Wang, J., Atallah, K. and Howe, D., 2004. Rotor eddy-current loss in permanent magnet brushless machines. *IEEE transactions on magnetics*, 40(4), pp.2104-2106.
- [125] Wu, L., Qu, R. and Li, D., 2017, May. Analysis of eddy current losses in surface-mounted permanent magnet vernier machines. In *2017 IEEE International Electric Machines and Drives Conference (IEMDC)* (pp. 1-6). IEEE.
- [126] J. Pandya and A. Kapil, "Effect of magnet segmentation on cogging torque of radial flux permanent magnet brushless DC motor," *2016 IEEE 7th Power India International Conference (PIICON)*, 2016, pp. 1-3, doi: 10.1109/POWERI.2016.8077274.
- [127] Ede, J.D., Atallah, K., Jewell, G.W., Wang, J.B. and Howe, D., 2007. Effect of axial segmentation of permanent magnets on rotor loss in modular permanent-magnet brushless machines. *IEEE Transactions on industry applications*, 43(5), pp.1207-1213.
- [128] Madina, P., Poza, J., Ugalde, G. and Almandoz, G., 2011, August. Magnet eddy current loss calculation method for segmentation analysis on permanent magnet machines. In *Proceedings of the 2011 14th European Conference on Power Electronics and Applications* (pp. 1-9). IEEE.

- [129] Virilan, B., Munteanu, A., Livadaru, L., Simion, A. and Nacu, I., 2017, October. Pole magnets segmentation effect on permanent magnet synchronous generators. In *2017 International Conference on Electromechanical and Power Systems (SIEMEN)* (pp. 163-168). IEEE.
- [130] Schmidt, E., Kahenbacher, M. and Wolfschluckner, A., 2017, May. Eddy current losses in the permanent magnets of synchronous machines—Comparison of planar and cylindrical arrangements with various pole coverages. In *2017 IEEE International Electric Machines and Drives Conference (IEMDC)* (pp. 1-6). IEEE.
- [131] Yamazaki, K., Kanou, Y., Fukushima, Y., Ohki, S., Nezu, A., Ikemi, T. and Mizokami, R., 2010. Reduction of magnet eddy-current loss in interior permanent-magnet motors with concentrated windings. *IEEE Transactions on Industry Applications*, 46(6), pp.2434-2441.
- [132] Ma, J. and Zhu, Z.Q., 2017, May. Magnet eddy current loss reduction in a 3-slot 2-pole permanent magnet machine. In *2017 IEEE International Electric Machines and Drives Conference (IEMDC)* (pp. 1-8). IEEE.
- [133] Xue, S., Xu, H. and Fang, C., 2012, June. The effect of stator slot and air gap length on high speed brushless PM motor. In *Proceedings of the 7th International Power Electronics and Motion Control Conference* (Vol. 1, pp. 281-285). IEEE.
- [134] Merdzan, M., Paulides, J.J.H. and Lomonova, E.A., 2015, March. Comparative analysis of rotor losses in high-speed permanent magnet machines with different winding configurations considering the influence of the inverter PWM. In *2015 Tenth International Conference on Ecological Vehicles and Renewable Energies (EVER)* (pp. 1-8). IEEE.
- [135] Gerada, C. and Bradley, K.J., 2008. Integrated PM machine design for an aircraft EMA. *IEEE Transactions on Industrial Electronics*, 55(9), pp.3300-3306.
- [136] Parsa, L. and Toliyat, H.A., 2007. Fault-tolerant interior-permanent-magnet machines for hybrid electric vehicle applications. *IEEE transactions on vehicular technology*, 56(4), pp.1546-1552.
- [137] Mecrow, B.C., Jack, A.G., Atkinson, D.J., Green, S.R., Atkinson, G.J., King, A. and Green, B., 2004. Design and testing of a four-phase fault-tolerant permanent-magnet machine for an engine fuel pump. *IEEE Transactions on Energy Conversion*, 19(4), pp.671-678.
- [138] Noel, C., Takorabet, N. and Meibody-Tabar, F., 2004, October. Short-circuit current reduction technique for surface mounted PM machines high torque-low speed applications. In *Conference Record of the 2004 IEEE Industry Applications Conference, 2004. 39th IAS Annual Meeting.* (Vol. 3, pp. 1427-1433). IEEE.
- [139] Bianchi, N. and Bolognani, S., 2005, September. Fault-tolerant PM motors in automotive applications. In *2005 IEEE Vehicle Power and Propulsion Conference* (pp. 747-755). IEEE.

- [140] Mecrow, B.C., Jack, A.G., Haylock, J.A. and Coles, J., 1996. Fault-tolerant permanent magnet machine drives. *IEE Proceedings-Electric Power Applications*, 143(6), pp.437-442.
- [141] Abolhassani, M.T. and Toliyat, H.A., 2009, May. Fault tolerant permanent magnet motor drives for electric vehicles. In *2009 IEEE International Electric Machines and Drives Conference* (pp. 1146-1152). IEEE.
- [142] Mitcham, A.J., Antonopoulos, G. and Cullen, J.J.A., 2004. Favourable slot and pole number combinations for fault-tolerant PM machines. *IEE Proceedings-Electric Power Applications*, 151(5), pp.520-525.
- [143] Simpson, N., Wrobel, R. and Mellor, P.H., 2013. Estimation of equivalent thermal parameters of impregnated electrical windings. *IEEE Transactions on Industry Applications*, 49(6), pp.2505-2515.
- [144] Hashin, Z. and Shtrikman, S., 1962. A variational approach to the theory of the effective magnetic permeability of multiphase materials. *Journal of applied Physics*, 33(10), pp.3125-3131.
- [145] Shen, X., Mecrow, B., Deng, X., Donaghy-Spargo, C., Whalley, R. and Chakraborty, N., 2019. Direct Air Cooling of High-Power Permanent Magnet Machines. In *2019 IEEE Energy Conversion Congress and Exposition (ECCE)* (pp. 5637-5644). IEEE.
- [146] Li, Q., Shen, X., Mecrow, B. and Deng, X., 2021. Hybrid cooling design of permanent magnet synchronous machines.
- [147] Li, Q., Mecrow, B., Shen, X., Deng, X. and Ikhlaiq, M., 2022, June. Design and analysis of a cooling system for permanent magnet synchronous machines. In *11th International Conference on Power Electronics, Machines and Drives (PEMD 2022)* (Vol. 2022, pp. 141-145). IET.
- [148] Al-ani, M.M.J., Barrans, S.M. and Carter, J., 2017, May. Electromagnetic and mechanical analysis of high speed SPM rotor with copper shield. In *2017 IEEE International Electric Machines and Drives Conference (IEMDC)* (pp. 1-8). IEEE.
- [149] López, A.A., Smith, D.J. and Mecrow, B., 2022. Magnet loss reduction: A new technique beyond segmentation and shielding.